NORTHWESTERN UNIVERSITY

Control of Light-Induced Electronic Behavior at Interfaces of Hybrid Nanomaterials

A DISSERTATION

SUBMITTED TO THE GRADUATE SCHOOL

IN PARTIAL FULFILLMENT OF THE REQUIREMENTS

for the degree

DOCTOR OF PHILOSOPHY

Field of Chemistry

By

Suyog Padgaonkar

EVANSTON, ILLINOIS

September 2021

Abstract

Control of Light-Induced Electronic Behavior at Interfaces of Hybrid Nanomaterials

Suyog Padgaonkar

This dissertation explores ways to utilize physical parameters at the nanoscale interface to control the properties of mixed-dimensional heterojunctions (MDHJs). MDHJs combine the desirable properties of different classes of low-dimensional nanomaterials (materials that are quantum confined in at least one dimension). While MDHJs have achieved superlative performance for a variety of optoelectronic applications through this approach, they present even more opportunities to achieve emergent and exotic behavior. Because these low-dimensional materials have large surface-to-volume ratios, they are sensitive to small changes in their physical environment. This sensitivity can be leveraged to tune the properties of MDHJs by altering physical parameters at the mixed-dimensional interface. This dissertation focuses primarily on a few examples that develop a means to control over the rates and yields of charge and energy transfer between low-dimensional materials because this understanding is key to their future use in applications. The molecular orientation of organic molecules on the surface of a two-dimensional material can control the lifetime of charge separation at the mixed-dimensional interface. Different wavelengths of light can control the photoluminescence of quantum dots by leveraging the change in the rate of charge transfer to bound photoswitchable ligands. The light harvesting ability of chemically-reactive black phosphorus (BP) is enhanced by utilizing energy transfer from a close-packed film of quantum dots through a protective encapsulation layer to the BP. Beyond developing control over rates of charge carriers across the mixed-dimensional

interface, physical parameters in MDHJs can be altered to achieve even more exotic phenomena, such as exciton delocalization, spin selectivity, and quantum emission, in MDHJs. Finally, beyond the fundamental understanding of the properties of MDHJs, this dissertation looks beyond the lab and describes the development of a science outreach program to explain current research to senior citizens and other voting-age populations, which is critical because the broad understanding of basic scientific research is key to a more informed society.

Acknowledgements

A PhD is an extraordinarily humbling experience. There is no one telling you exactly what to do, and there is no book of instructions to follow. The pursuit of a PhD demonstrates, all too vividly, how little you know about the world, and it also reminds, all too often, how much you depend upon the generosity, kindness, and support of others. My growth during graduate school would not be possible without the help of so many others. I have been fortunate to have interacted with so many intelligent and helpful people throughout the past five years in graduate school. To those who may not be explicitly mentioned here, please know that I still appreciate your support.

I am indebted to my advisors, Prof. Emily Weiss and Prof. Mark Hersam, for their guidance over the last five years. From Emily, I have learned the value of time management and planning ahead; I don't know many people who are more efficient than Emily. From her countless revisions of my drafts, I developed a thick skin to her comments in the margins and vastly improved my technical writing skills. From Mark, I have learned the importance of seeing the forest beyond the trees; it is too easy to get lost in the minutiae during research or life in general. I have further appreciated his intellectual curiosity, which is evident from both his incisive questions and the range of research being done in his group. Both Emily and Mark made my graduate school experience easier through their timely email responses, and I do not take this for granted.

I am thankful to my committee, Prof. Rich Schaller, Prof. Lin Chen, and Prof. Lincoln Lauhon, for their time and for pushing me to changing my approach to research. Research cannot be done without funding, and I appreciate MRSEC, ISEN, and (the now defunct) ANSER/LEAP, along with their staff for the financial and logistical support. This work would not be possible without

the support of the many staff members in the Department of Chemistry, Department of Materials Science and Engineering, Office of Research Safety, and research cores, especially Dr. Paul Smeets, Dr. Xinqi Chen, and Dr. Gajendra Shekhawat. As an interdisciplinary research center, MRSEC also gave me the chance to work with many others throughout graduate school. The research projects described in this document are all collaborative efforts, and I am thankful for the intellectual and scientific contributions for these projects from my co-authors, as well as others with whom I had many insightful conversations.

Prior to entering graduate school, I was fortunate to have rewarding research experiences that excited me enough to pursue a PhD. My first research experience was in the lab of Prof. Yanbin Zhang, where I learned that I was not cut out for basic biomedical research but nonetheless learned so much more about the scientific method in action. Dr. Amy Scott gave me the chance to work in her lab, where I became interested in ultrafast spectroscopy and light-sensitive materials, and she, along with Dr. Mercedes Mazza, Dr. Shiori Yamazaki, Dr. Carmen Guzman, and Dr. Sam Peurifoy, equipped me with the fundamental skills to explore this exciting research area. With the support of Christopher LaPrade and ACS, I was able to spend a summer abroad in Singapore doing research with chemically functionalized biodegradable materials in the lab of Prof. Suresh Valiyaveettil, and this experience taught me how universal the language of science can be.

One thing that I find ironic is that the people who helped me most during the beginning of my PhD were not acknowledged in any of these papers, but I could not have done any of this work without their help early in my PhD. I was helped by many individuals in the Weiss and Hersam groups early on, primarily from Dr. Mohamad Kodaimati, Dr. Shichen Lian, Dr. Spencer Wells, Prof. Vinod Sangwan, Dr. Chen Wang, Dr. Chengmei Zhong, Dr. Cameron Rogers, Dr. Kaitlyn

Perez Redfern, Dr. James Schwabacher, and Dr. Ofer Kedem. Throughout my PhD, I have been fortunate to be able to rely on Jack Olding and Dr. Sam Amsterdam for their scientific input and knowledge of the field. In the last two years, my productivity saw a spike due to the arrival of several individuals on my research path: Shawn (Zhao) Irgen-Gioro, Dr. Rafael López-Arteaga, Paul Brown, and Chris Eckdahl – thank you all for your time and efforts towards making science both fun and fruitful. I also saw myself take the role of a mentor in the latter stage of my PhD, and I am thankful to Brendan Kerwin, Anushka Dasgupta, Christina Hemmingsen, and Riddhi Ananth for giving me the opportunity to share some of the things I have learned and allowing me to develop my mentoring skills. I particularly appreciate Paul Brown, who took a chance on me as a sophomore interested in research, and has been the ideal junior researcher, mentee, and friend – I know you will enjoy many successes in your own PhD journey.

I am grateful that I could form friendships with my colleagues because of how friendly the members of both of my research groups are. To the Rogers Park crew (Sonal Rangnekar, David Lam, Norman Luu, and Sam Amsterdam), thank you for being a rich source of humor and support, especially of late. To the 1013 family (Dr. Hadallia Bergeron, Dr. Megan Beck, and Dr. Will Gaviria) with whom I had the pleasure of sharing an office for two years, thank you for making the office feel like a home. To the Hersam group book club, thank you for enriching and enlightening discussions beyond nanomaterials research, and thanks to Eden Aklile for leading this effort. To everyone who participated in pickup basketball and volleyball over the years, thank you for the opportunity to burn off some steam and many competitive games.

Beyond the lab, I became interested in how science intersected with society and policy. I was fortunate to join the efforts of like-minded people, especially Dr. Michael Mullowney and Dr.

Louisa Savereide, at Northwestern early on in my PhD to form SPOT, and it has been a pleasure to watch SPOT grow even as we took a step back due to the efforts of Chamille Lescott, Jamie Neely, Kavi Chintam, Emma Zajdela, Emily Schafer, and others. I am especially grateful to the many people who volunteered to take part in *SwS* throughout my time leading that effort, and thank you to Emily for continuing and growing the program. I was inspired to start *SwS* by the hard work of Dr. Kathleen Stair, who has a tireless passion for outreach, and the many people I met at Science in Society during my involvement in Science Club. Prof. Yarrow Axford is a role model in her dedication to science communication and outreach, and I appreciate her constant encouragement of SPOT and *SwS*.

I am extremely thankful to the many old friends I relied upon and the many new friends I formed over the last five years for providing a distraction from the lab. I am also grateful to be able to commiserate experiences and form fun memories with my chemistry roommates: Nate, Dawning, Matt, Daylan, and Joaquin.

Most of all, I am thankful for my family. To my parents, thank you for your inexhaustible love and support. I could not have done anything without you. To my sister Kimaya, thank you for your wisdom and advice. I value your opinion more than anyone else's. To my grandparents Anna and Anu and my uncle Pramod, I will reconnect in my next journey. To my relatives in Chicagoland, thank you for always having your door open. I am glad I got the chance to create new memories after coming back here full circle. To my relatives elsewhere in the US and India, thank you for being a source of support throughout the turbulence of life. Finally, to my partner Luyi, I am ever grateful for your boundless patience and support. Thank you for all you do.

List of Abbreviations

0D	Zero-dimensional
1D	One-dimensional
2D	Two-dimensional
3D	Three-dimensional
AFM	Atomic force microscopy
ALD	Atomic layer deposition
AlO_x	Aluminum oxide, alumina
BP	Black phosphorus
$CDCl_3$	Deuterated chloroform
CF	Control furan
CdS	Cadmium sulfide
CdSe	Cadmium selenide
CuPc	Copper phthalocyanine
CR	Charge recombination
CT	Charge transfer
DFT	Density functional theory
eT	Electron transfer
EnT	Energy transfer
ES	Excited state
ESA	Excited state absorption

FFC	Furylfulgide carboxylate
FFM	Furylfulgide methyl ester
FRET	Forster resonance energy transfer
FDTD	Finite difference time domain
GSB	Ground state bleach
H_2Pc	Free-base phthalocyanine
HH	Parallel polarization
HOMO	Highest occupied molecular orbital
HV	Perpendicular polarization
IRF	Instrument response function
ISC	Intersystem crossing
LLI	Lifelong learning initiative
LUMO	Lowest unoccupied molecular orbital
MDHJ	Mixed-dimensional heterojunction
MoS_2	Molybdenum disulfide
NIR	Near-infrared
nm	nanometer
NMR	Nuclear magnetic resonance
ns	nanosecond
OA	Oleic acid
PbS	Lead sulfide
Pc	Phthalocyanine

PET	Photoinduced electron transfer
PL	Photoluminescence
ps	picosecond
PSS	Photostationary state
QD	Quantum dot
QY	Quantum yield
Si	Silicon
SiO_2	Silicon dioxide
STEM	Science, technology, engineering, math
SwS	Science with Seniors
TA	Transient absorption
TMDC	Transition metal dichalcogenide
TRPL	Time-resolved photoluminescence
UV	Ultraviolet
ZnPc	Zinc phthalocyanine
ZnS	Zinc sulfide
λ_{peak}	Peak wavelength
λ_{probe}	Probe wavelength
λ_{pump}	Pump (excitation) wavelength

Table of Contents

List of Figures

List of Tables

List of Schemes

Chapter 1: Introduction

Adapted from:

Padgaonkar, S.; Olding, J. N.; Lauhon, L. J.; Hersam, M. C.; Weiss, E. A., *Accounts of Chemical Research*, **2020**, *53* (4), 763-772.

1.1 Chapter Summary

The electronic dimensionality of a material is defined by the number of spatial degrees of confinement of its electronic wave function. Low-dimensional semiconductor nanomaterials with at least one degree of spatial confinement have optoelectronic properties that are tunable with size and environment (dielectric and chemical) and are of particular interest for optoelectronic applications such as communications, energy harvesting, and photocatalysis. By combining nanomaterials of differing dimensionalities, mixed-dimensional heterojunctions (MDHJs) exploit the desirable characteristics of their components. For example, the strong optical absorption of zero-dimensional (0D) materials combined with the high charge carrier mobilities of two-dimensional (2D) materials widens the spectral response and enhances the responsivity of mixed-dimensional photodetectors, which has implications for ultrathin, flexible optoelectronic devices. MDHJs are highly sensitive to: (i) interfacial chemistry because of large surface area-to-volume ratios; and (ii) electric fields, which are incompletely screened because of the ultrathin nature of MDHJs. This sensitivity presents opportunities for control of physical phenomena in MDHJs through chemical modification, optical excitation, externally applied electric fields and other environmental parameters. Since this fast-moving research area is beginning to pose and answer fundamental questions that underlie the fundamental optoelectronic behavior of MDHJs, it is an opportune time to assess progress and suggest future directions in this field.

In this chapter, we first outline the characteristic properties, advantages, and challenges for low-dimensional materials, many of which arise as a result of quantum confinement effects. The optoelectronic properties and performance of MDHJs are primarily determined by dynamics of excitons and charge carriers at their interfaces, where these particles tunnel, trap, scatter, and/or recombine on the time scales of tens of femtoseconds to hundreds of nanoseconds. We discuss

several photophysical phenomena that deviate from those observed in bulk heterojunctions, as well as factors that can be used to vary, probe, and ultimately control the behavior of excitons and charge carriers in MDHJ systems. We also discuss optoelectronic applications of MDHJs, namely photodetectors, photovoltaics, and photocatalysts, and identify current performance limits compared to state-of-the-art benchmarks. Finally, this chapter concludes by outlining the course of this dissertation.

1.2 Low-Dimensional Materials

Due to the quantum confinement effect, in which the electronic wavefunction is spatially restricted by a physical barrier, the properties of low-dimensional materials can be tuned as a function of size.[1] These properties are highly sensitive to their immediate environment as a result of the large surface-area-to-volume ratios of the nanostructures. Low-dimensional materials are

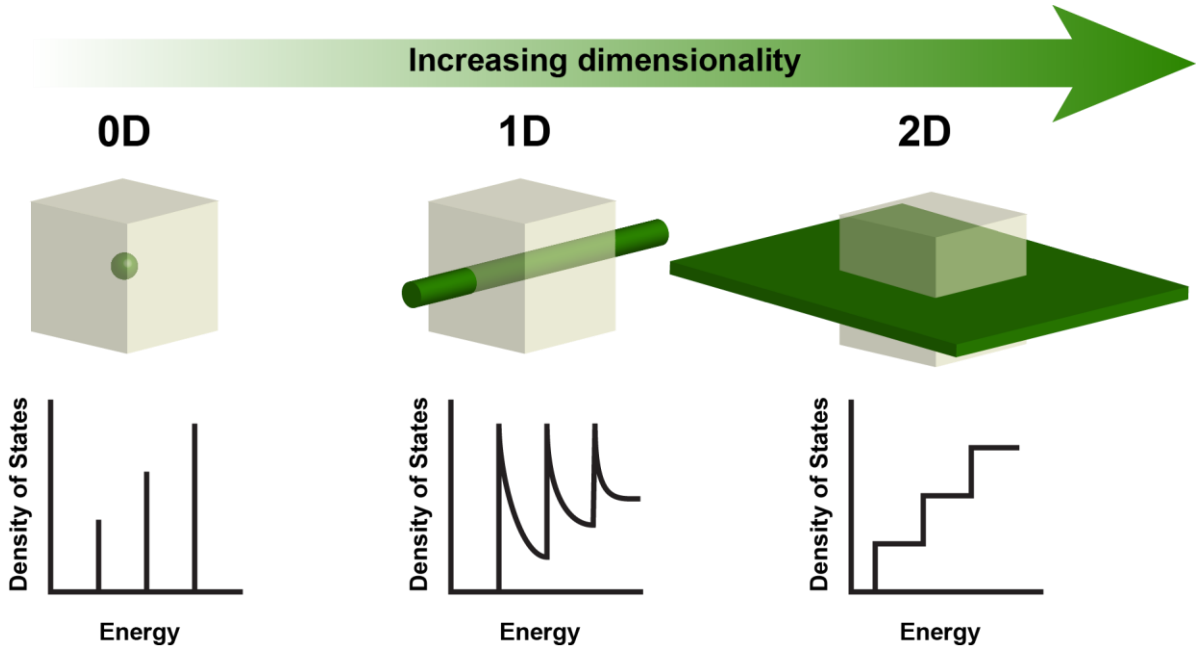

Figure 1.1. Schematic diagram depicting the dependence of quantum confinement and density of states on dimensionality.

categorized according to the *number* of dimensions along which charge carriers or excitons (*i.e.*, electrostatically bound electron-hole pairs) are free to move, as shown in **Figure 1.1**. The degrees of freedom for a charge carrier in a given material dictate its density of states and the degree to which its k-space is filled with electrons. For example, a zero-dimensional (0D) material has no degrees of freedom for a charge carrier and thus available states exist only at discrete orbital energies, while the two degrees of freedom for a carrier in a two-dimensional (2D) material allow for the existence of states in between discrete orbital energies.[2] Zero-dimensional (0D) materials include isolated colloidal quantum dots (QDs)[3] and organic molecules;[4] one-dimensional (1D) materials include nanotubes/rods/wires[5] and conjugated polymers;[6] and two-dimensional (2D) materials include nanosheets/platelets and layered materials that can be isolated in ultrathin form.[7,8] While exceptions exist, each class of low-dimensional material typically has characteristically advantageous optical and/or electronic properties. 0D materials have high photoluminescence quantum yields and large optical absorption coefficients, while 2D materials have high carrier mobilities. Conversely, films of 0D materials generally have low carrier mobilities due to abundant tunneling barriers and other defects,[3] and 2D materials have low photoluminescence quantum yields, particularly in their as-synthesized forms, due to high rates of defect-mediated non-radiative recombination.[7]

One way to bypass the intrinsic limitations of a given low-dimensional material is to form a mixed-dimensional heterojunction (MDHJ) between two low-dimensional materials with different dimensionalities.[9] Because the surfaces of most low-dimensional materials are passivated (dangling bond-free), van der Waals assembly that leads to strong electronic coupling is commonplace for MDHJs. A MDHJ consisting of 0D PbS QDs and 2D MoS_2 results in a high-

performance photodetector, due to the strong optical absorption of PbS QDs and the high carrier mobility of MoS_2.[10] Sensitization with PbS QDs increases the responsivity of 2D MoS_2-based photodetectors by five orders of magnitude, with further improvements enabled by the introduction of an intermediate layer to reduce interfacial traps[11] or the use of architectures that bypass the tradeoff between gain and speed.[12] MDHJs can be used for a variety of other optoelectronic applications, including sensing, energy harvesting, catalysis, and computing, but because of their electronically complex interfaces, it is not straightforward to predict the behavior of an exciton or charge carrier within these junctions.[13] In an effort to delineate the state-of-the-art and provide guidance for future research, this chapter provides a critical assessment of the recent literature concerning interfacial photophysics in MDHJs.

1.3 Interfacial Photophysics in MDHJs

In MDHJs (similar to other organic and semiconductor heterojunctions), photoexcitation leads to either charge or energy transfer (**Figure 1.2a**) if (i) one or both processes is energetically favorable, and (ii) the rate of one or both processes is competitive with exciton decay *via* other radiative and non-radiative processes (**Figure 1.2b**). Control of this competition is a basic but critical first step in engineering MDHJs for optoelectronic applications.

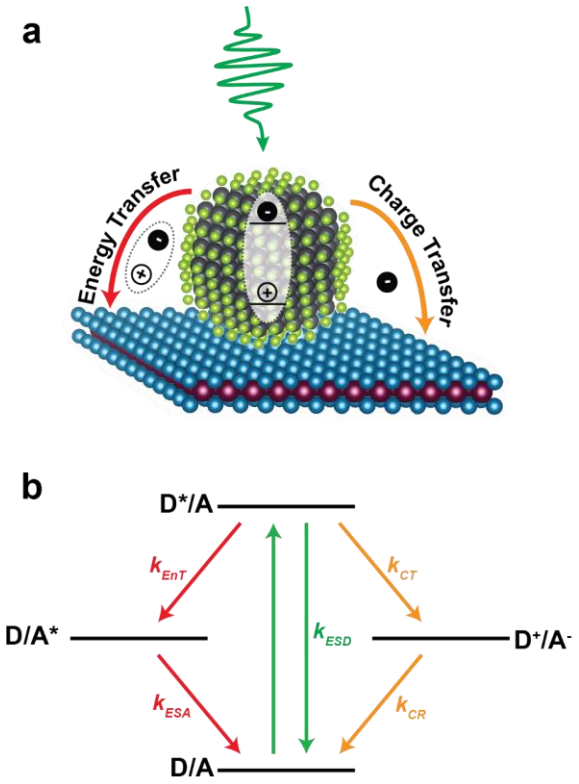

Figure 1.2. (a) Schematic showing mechanisms of energy and charge transfer from a 0D material to a 2D material upon photoexcitation. **(b)** Jablonski diagram illustrating photophysical pathways in the MDHJ with associated rates, *k*. ESD, donor excited state decay; EnT, energy transfer; CT, charge transfer; ESA, acceptor excited state decay; CR, charge recombination.

1.3.1 Charge Transfer in MDHJs

Engineering the alignment of energy levels at an interface, sometimes called "bandgap engineering", can be used to drive charge transfer (CT), also known as exciton dissociation, in MDHJs. In a type II heterojunction, photoinduced electron transfer (eT) is thermodynamically downhill from the electron donor to the electron acceptor material at the interface, and photoinduced hole transfer (hT) is favorable in the opposite direction. For instance, in a type II MDHJ consisting of an 1D organic polymer PTB7 (poly({4,8-bis[(2-ethylhexyl)oxy]benzo[1,2-

b:4,5-b′]dithiophene-2,6-diyl}{3-fluoro-2-[(2-ethylhexyl)carbonyl] thieno[3,4-b]thiophenediyl}) and monolayer 2D MoS_2, the photoluminescence (PL) intensity of both materials decreases relative to that of the isolated materials due to interfacial CT, **Figure 1.3a**.[14] The degree of PL quenching in both materials is tunable through the thickness of the PTB7 layer such that, at an optimal thickness of 16 nm, the PL of both materials is completely quenched. In this case, the interfacial CT was exploited in a large-area MDHJ photovoltaic cell with an open-circuit voltage of 0.21 V, whereas devices made from the corresponding isolated materials did not generate a photovoltage.

In cases of strong electronic coupling between the components of a MDHJ, such as a WS_2/tetracene junction, new PL peaks are observed in emission spectra as a result of spatially-indirect excitons that emerge at a lower energy than the emission of either component alone.[15] In a recent study of metallated phthalocyanine molecules on MoS_2, the mixing of the electronic orbitals of phthalocyanine with the density of states of MoS_2 similarly led to the formation of a new ground state absorption peak associated with a transition to interfacial excitonic states, **Figure 1.3b**.[16] This peak was observed for a series of different metal centers of the phthalocyanine molecule, and theoretical modeling showed that the energy of this peak corresponds to the mixing of a non-frontier orbital (HOMO-1) of the metallated phthalocyanine with the valence band of MoS_2. These interactions highlight the importance of orbital mixing in determining interfacial exciton energies in MDHJs.

Time-resolved spectroscopic measurements of MDHJ systems with type II band alignments have revealed a common theme, namely sub-picosecond photoinduced charge transfer[17–19] that is primarily due to the high density of states in the 2D material.[20,21] For the case of

phthalocyanine/MoS_2 MDHJs, selective excitation of each component elucidates the rates of photoinduced eT and hT and subsequent charge recombination. In **Figure 1.3c**, kinetic traces extracted from transient absorption (TA) measurements of a copper phthalocyanine (CuPc)/MoS_2 heterojunction after selective excitation of the MoS_2 show that the ground state bleach corresponding to the A exciton of MoS_2 recovers faster at early times but lives longer at later times than the A exciton of isolated MoS_2.[21] The ground state bleach indicates population of the lowest excited states, which reduces absorption due to state filling, and the delayed recovery of the MoS_2 ground state bleach (in the presence of CuPc) suggests charge separation. Based on the changes in the kinetics of the ground state bleach, the timescale of photoinduced hT from MoS_2 to CuPc was determined to be 880 fs, and the lifetime of the charge-separated state was as long as 70 ns. Raman spectroscopy further showed that copper CuPc molecules lie flat ("face-on") on MoS_2. Given the strong electronic coupling that results from the orbital overlap between face-on CuPc and MoS_2, sub-picosecond charge separation is reasonable in this case. On the other hand, the long charge separation lifetime in this MDHJ can be attributed to hole hopping away from the interface through the face-on CuPc stack. This conclusion was corroborated by the observation that unmetallated phthalocyanine (H_2Pc)/MoS_2 junctions, within which H_2Pc adopts a mixed (face-on and edge-on) orientation on MoS_2, have charge recombination times on the order of 4 ns rather than 70 ns. Long-lived charge separation has also been attributed to hole hopping away from the heterointerface in single-walled carbon nanotube/MoS_2 MDHJs.[22] These results highlight that the charge separation

lifetimes in these systems can be modulated with synthetic changes that influence the geometry of the interface.

Since 2D materials have thickness-dependent optoelectronic properties, synthetic tunability is not limited to the organic 0D component. For example, enhancement of the in-plane, ring-stretching Raman modes of CuPc, which arises due to interfacial orbital mixing, decreases with

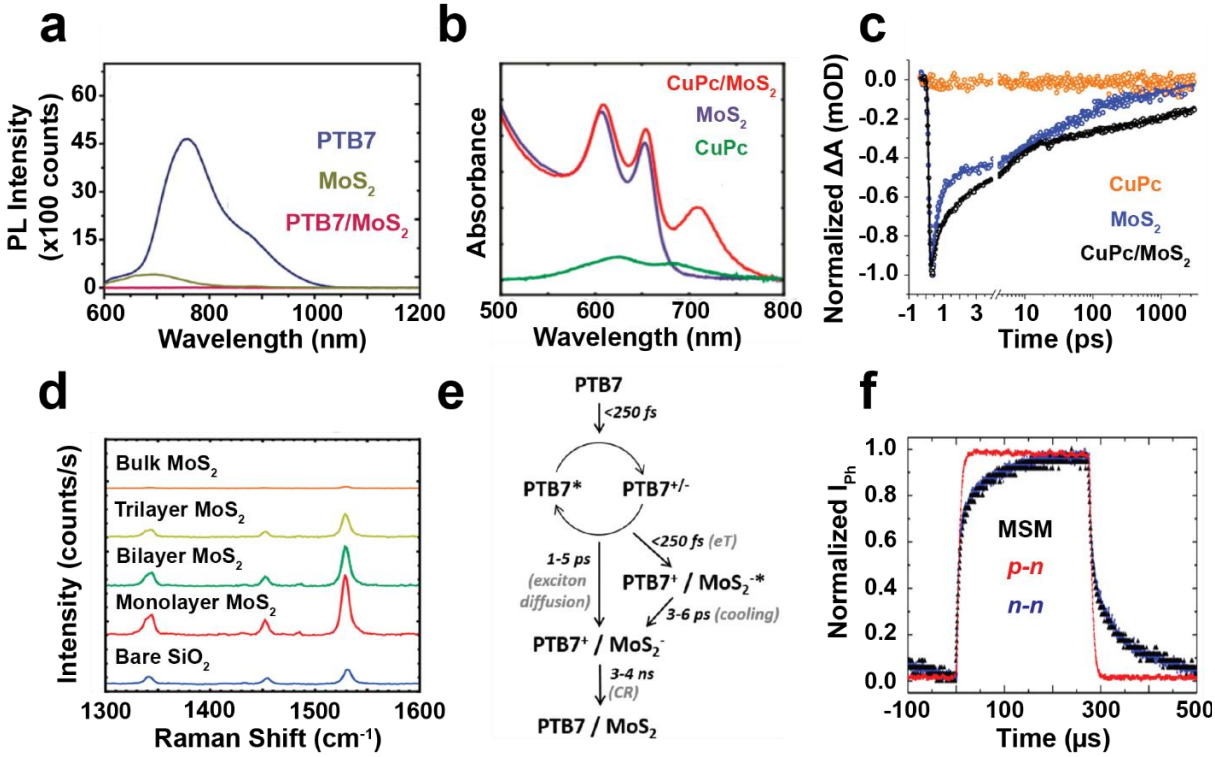

Figure 1.3. Charge separation in type II MDHJs. **(a)** Mutual PL quenching in a PTB7/MoS_2 MDHJ, indicating charge transfer. Adapted with permission from ref. 14. Copyright 2016 American Chemical Society. **(b)** New optical absorption peak in a CuPc/MoS_2 MDHJ. Adapted with permission from ref. 16. Copyright 2019 American Chemical Society. **(c)** Ultrafast and long-lived charge separation in a CuPc/MoS_2 MDHJ from transient absorption measurements. Adapted with permission from ref. 21. Copyright 2019 American Chemical Society. **(d)** Dependence of CuPc Raman signal enhancement on MoS_2 layer thickness. Adapted with permission from ref. 16. Copyright 2019 American Chemical Society. **(e)** Map of carriers from PTB7 in a heterojunction with MoS_2 after photoexcitation. Adapted with permission from ref. 20. Copyright 2018 American Chemical Society. **(f)** Time-resolved photocurrent measurements on a Si nanowire/MoS_2 heterojunction. Adapted with permission from ref. 25. Copyright 2018 American Chemical Society.

increasing thickness of the underlying MoS_2 layer because additional layers absorb more energy (and therefore scattering), **Figure 1.3d**.[16] Another effect of increasing thickness is the contribution of band-bending, which influences the CT dynamics at the interface. In particular, while exciton dissociation occurs between ZnPc and MoS_2 in both its bulk or monolayer forms, the competitive mechanism of back electron transfer leads to triplet formation in ZnPc only when combined with bulk MoS_2 that is thick enough for band-bending to take place.[23]

Although ultrafast CT (on the order of tens to hundreds of femtoseconds), which is desirable for applications that depend on extracting photoinduced charge carriers, will likely outcompete other processes, simultaneous loss mechanisms often plague MDHJs. The organic component is often the source of loss, particularly if deposited in thick (>10 nm) layers where a majority of the material is not interacting with the 2D material at the interface. For instance, in the PTB7/MoS_2 case, the propensity of PTB7 to form polarons (competitive with exciton formation) almost immediately upon photo-excitation reduces the total CT yield,[20] which in turn leads to suboptimal internal quantum efficiency and fill factor in PTB7-based solar cells, **Figure 1.3e**.[14] In pentacene/MoS_2 MDHJs, ultrafast intersystem crossing in pentacene occurs before most singlet excited states can reach the interface and limits the overall CT yield since the triplet state does not have enough energy to donate an electron to MoS_2.[17] Back electron transfer, in which an electron is transferred from the original electron acceptor back to the low-lying donor triplet state after undergoing a spin conversion, is another prominent loss mechanism in organic/2D MDHJs.[23,24]

Techniques such as time-resolved scanning photocurrent microscopy, which couple optical excitation and electronic measurements, provide insight into how interfacial exciton dissociation affects charge carrier behavior in the presence of external electric fields. For the case of a 1D

silicon nanowire (Si NW)/2D MoS_2 MDHJ, the transient photocurrent is larger and faster when the Si NW is p-type rather than n-type, **Figure 1.3f**.[25] This observation indicates that the larger magnitude of the internal electric field generated at the p-n junction increases the yield of exciton dissociation and the rate of carriers moving out of the depletion region, resulting in faster photoresponse and enhanced photocurrent. Due to reduced electrical screening, the lateral extent of the depletion region formed in 1D/2D MDHJs is larger than that at 2D/3D interfaces, resulting in rapid carrier separation that is advantageous for many photodetector applications.

Scanning photocurrent microscopy has also been used to distinguish between energy transfer and charge transfer processes in CdSe QD/MoS_2 MDHJs.[26] When CdSe QDs have a thick ZnS shell that allows energy transfer but inhibits CT, the photocurrent response increases with increasing light intensity. In contrast, when the CdSe QDs have no CT-inhibiting shell, the photocurrent response decreases with increasing light intensity. This result can be attributed to a photogating effect induced by CT since the remaining electrons in CdSe QDs (after the hole transfer process) form a negative top gate potential on MoS_2, while no such potential is generated during the energy transfer process since both carriers are effectively transferred.

Because of their ultrafast exciton dissociation and long-lived charge separated states, many examples of MDHJs have shown promise for optoelectronic applications, although a number of challenges remain unresolved.[27] For example, poor interfacial quality in MDHJs can contribute to competitive recombination pathways, which can potentially be addressed through the development of new processing methods.[28] While some theoretical work has been done to understand the nature of electronic transitions between molecular orbitals and quasi-continua, a more complex modeling framework than a typical energy level diagram is likely to be necessary to understand electronic

transitions at the hybrid interface.[16,29–31] The few studies that have explored CT dynamics as a function of dimensionality suggest that increasing the dimensionality of the charge acceptor enhances CT rates and yields.[32] Finally, many studies have focused on MoS_2 and other transition metal dichalcogenides (TMDCs) because of their chemical stability, but exploration of other 2D semiconductors (*e.g.*, black phosphorus, monochalcogenides, and metal halides) may open research avenues not accessible with TMDCs alone.[33–37]

1.3.2 Energy Transfer in MDHJs

Photosynthetic systems exploit energy transfer, where an exciton is transferred from a larger bandgap donor material to a smaller bandgap acceptor material, to funnel excitations to desired locations. Energy transfer has been thoroughly studied in molecular systems, where it can generally be well described within the dipole approximation of classical Förster Theory. In MDHJs, energy transfer deviates from behavior typically observed in molecular systems as a result of less confined carriers, the ultrathin nature of the components, and integration into solid state devices. The rate of Förster energy transfer, when modeled as an interaction of two point dipoles, has a distance-dependence of $1/R^6$. In contrast, for Förster energy transfer from a 0D donor to a 2D acceptor, which is more accurately modeled as a sheet of dipoles, the distance dependence is $1/R^4$, which expands the range of distances over which efficient energy transfer is possible.[38] Similarly, by changing the shape of a 0D nanocrystal donor to a quasi-2D nanoplatelet, the distance dependence becomes $1/R^2$, **Figure 1.4a**.[39] Dipole-dipole coupling between components that are greater than 10 nm apart enables the insertion of interlayers and broadens the design space and processing conditions for heterostructures. For example, thin encapsulation layers such as alumina

may be deposited to protect ambient-reactive 2D substrates from atmosphere or solvents used during the deposition of photosensitizing QDs.

Looking ahead to the design of dynamic systems that are more complex than the static cases that have been studied thus far, interlayers that are responsive to external stimuli such as fields, photons, or environment could be used to modulate the electronic coupling between components. One possibility is tethering QDs to 2D substrates with pH-responsive (*e.g.*, DNA) or light-responsive linkers to dynamically modulate the interparticle distance. Heterojunctions comprising low-dimensional materials are particularly well-suited for such stimuli-responsive systems because external stimuli are incompletely screened by the atomically-thin materials, making multiple components and their interfaces accessible. Such concepts will be explored further below.

The rate of Förster energy transfer from a quantum dot to a 2D acceptor has been shown to be dependent on the number of layers of the 2D material, **Figure 1.4b**.[40,41] As the thickness of the 2D acceptor increases, it makes up a larger portion of the immediate dielectric environment of the donor relative to that of the supporting substrate, which impacts the energy transfer rate by two mechanisms. First, the additional layers increasingly screen the donor dipole's field in the uppermost acceptor layer, therefore decreasing the energy transfer rate. Second, there is increased, albeit weaker, absorption in the additional layers, effectively increasing the energy transfer rate. The change in energy transfer rate to the 2D acceptor with layer thickness is thus dependent on the dielectric function of the acceptor, which determines the relative magnitudes of the competing contributions from screening and increased absorption.[40] For example, the energy transfer rate from a CdSe/ZnS QD to MoS_2 decreases with increasing thickness of MoS_2 due to the larger contribution from enhanced screening. On the other hand, in graphene, the increased absorption

with increasing layer thickness dominates so that the energy transfer rate increases. As a result, layer thickness can be added to the list of parameters that allow engineering of the energy transfer rate within a MDHJ.

Finally, external electric fields can be used to modulate the carrier concentration, and thus the optical properties, of 2D materials. By tuning the carrier concentration, and therefore excitonic absorption, of MoS_2 in a top-gate architecture, the energy transfer rates from CdSe QDs to MoS_2

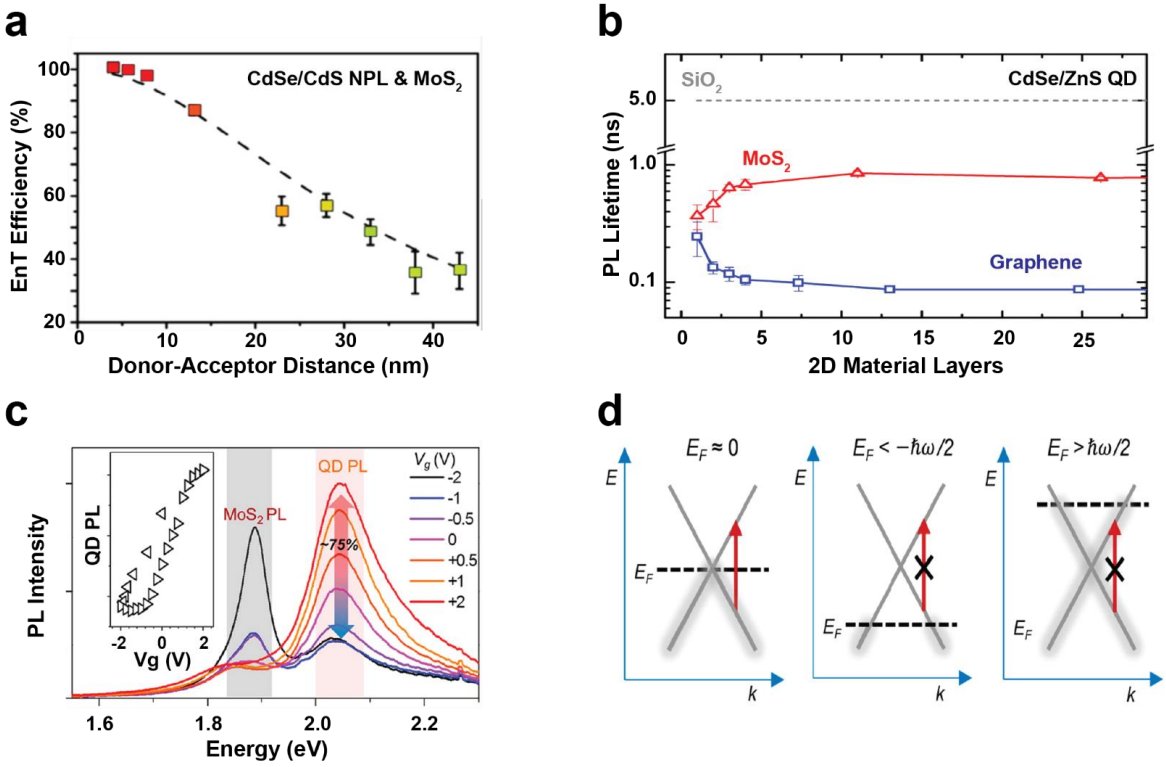

Figure 1.4. Energy transfer in MDHJs. **(a)** $1/R^2$ distance dependence of EnT from CdSe nanoplatelets to MoS_2 through varying thicknesses of Al_2O_3. Adapted with permission from ref. 39. Copyright 2018 American Chemical Society. **(b)** Difference of layer-dependence between graphene and MoS_2 as EnT acceptors of excitons from QDs. Adapted with permission from ref. 40. Copyright 2016 American Chemical Society. **(c)** Electrical control of EnT in a CdSe/ZnS QD/MoS_2 MDHJ by applying a gate bias. Adapted with permission from ref. 42. Copyright 2015 American Chemical Society. **(d)** Schematic depicting the mechanism of electrical modulation of energy transfer to graphene. Adapted with permission from ref. 43. Copyright 2014 American Chemical Society.

are tunable by up to 500%, **Figure 1.4c**.[42] Similarly, the Fermi level of graphene can be tuned to block optical transitions of certain energies and thereby control energy transfer from a nearby PbS/CdS QD donor, albeit not as effectively as MoS_2, which has a sharp excitonic absorption, **Figure 1.4d**.[43] While the energy transfer rate has been statically engineered in systems by controlling parameters such as the dipole orientation[44] or spectral overlap, the dynamic tunability of low-dimensional materials with electric fields has the potential to enable reconfiguration of energy pathways after fabrication or assembly, thus creating opportunities for electrically controlled nanoscale switches.

1.4 Optoelectronic Applications of MDHJs

The large absorption cross-sections, tunable optoelectronic properties, and ease of integration into device structures make low-dimensional materials a compelling target for optoelectronic applications. In particular, MDHJs have been employed as photodetectors, photovoltaics, and photocatalysts. In photodetection applications, devices based on low-dimensional materials must surpass existing thin film technologies (e.g. Si, InGaAs, HgCdTe) in cost or performance.[45] While the growth and processing of low-dimensional materials has not yet matured, the high costs and integration problems of existing InGaAs and HgCdTe technologies present an opportunity to outcompete on cost in the infrared detection space. On the performance side, devices exploiting the high mobility of graphene transport channels have demonstrated modulation bandwidths exceeding 60 GHz, beating state-of-the-art Ge detectors.[46] 2D transport channels have also been integrated with 0D photosensitizers to increase sensitivity. For example, PbS QDs have been deposited on graphene[47] and MoS_2[10] photodetectors to combine the large absorption cross-section of the QDs, particularly in the near-infrared spectral region, with the relatively high mobilities of

the 2D material, **Figure 1.5a**. In a related example, a 0D/3D photodetector composed of PbS QDs and bulk silicon demonstrated a responsivity competitive with state-of-the-art epitaxial semiconductor systems that require high-temperature growth.[48] The combination of high responsivity and microsecond time response required well-passivated (dangling bond-free) interfaces of both the silicon and colloidal QD surfaces. For 0D/2D MDHJs, high responsivities are commonly reported,[47,10] but response times are limited by long-lived trapped carriers, particularly at interfaces. Continued growth in the understanding of the surface chemistry of 2D

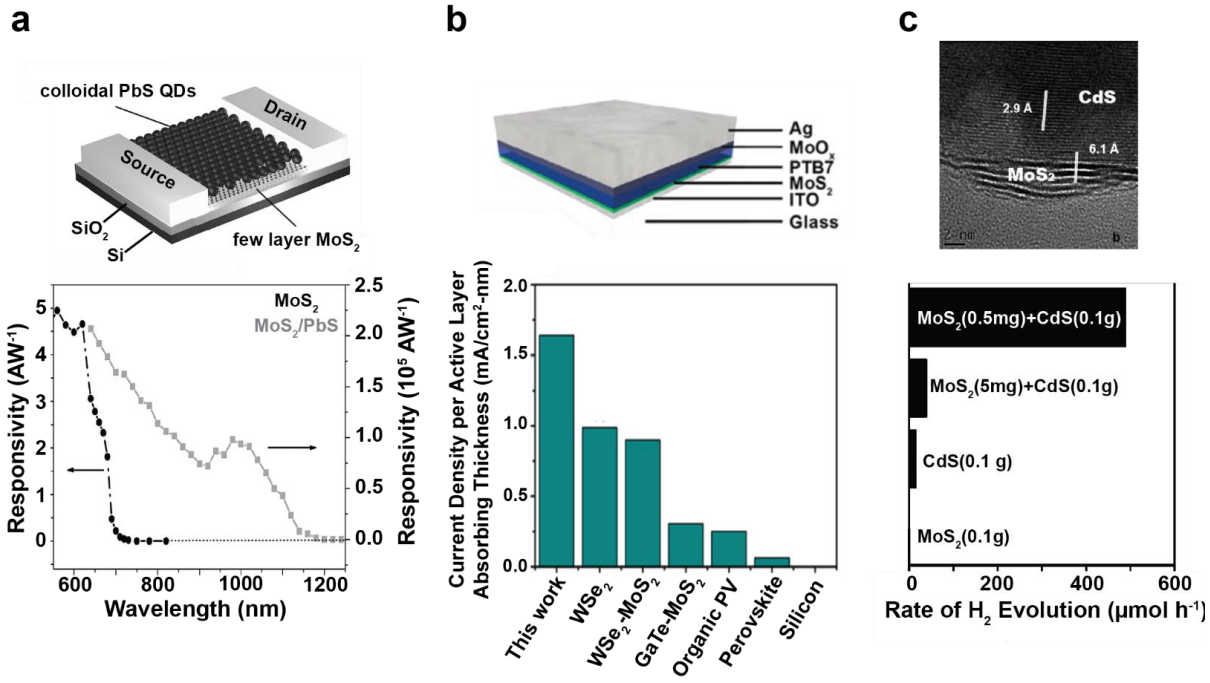

Figure 1.5. Optoelectronic applications of MDHJs. **(a)** Enhanced photoresponsivity and extended spectral range (into the near-infrared) of an MoS_2-based photodetector upon sensitization with PbS QDs. Adapted with permission. Ref. 10, 2015, Wiley-VCH. **(b)** High current density per thickness in a PTB7/MoS_2-based solar cell compared to other conventional photovoltaic materials. Adapted with permission from ref. 14. Copyright 2016 American Chemical Society. **(c)** Increased rate of photocatalytic H_2 evolution in a hybrid CdS/MoS_2 system. Adapted with permission from ref. 51. Copyright 2008 American Chemical Society.

materials, which is critically important due to their large surface areas, will be required for improving the speed of photodetectors based on 2D transport channels.

While silicon photovoltaics have a dominant position in large-scale power conversion applications, alternative material technologies may be viable in light conversion applications where flexibility and weight are important considerations.[49] The ultrathin nature of MDHJs makes them well suited for such applications and warrants further development in this area. An early example is the demonstration of large-area MDHJ solar cells based on the organic polymer PTB7 and 2D MoS_2; these cells have the highest current density, when normalized by thickness, of all known photovoltaic technologies, **Figure 1.5b**.[14] Despite the impressive photocurrent response, the photovoltage performance was suboptimal due to interfacial traps. With such a wide design space for combinations of 0D, 1D, and 2D materials, fundamental studies elucidating design rules or targets to focus further technological development are necessary. One promising avenue is the self-assembly of organic materials on the atomically flat basal planes of 2D substrates, where increased order could improve charge transport in the organic layer and reduce interfacial traps, enhancing collection efficiencies and charge carrier separation, respectively.[50]

Finally, colloidal dispersions of MDHJs synthesize some of the benefits of molecular photocatalysts (e.g. energy level tunability) with the surfaces that are typically presented by solid-state photocatalysts, offering the potential to go beyond existing systems in both performance and reactivity. Preliminary demonstrations in this area have used colloidal nanocrystals such as CdS QDs or CdSe nanoplatelets to photosensitize MoS_2[51] or Pt[52] catalysts, **Figure 1.5c**. Looking forward, one potential benefit of MDHJs is that colloidal dispersions of inorganic low-dimensional materials provide surfaces that could be used to template surface reactions for a desired

selectivity.[53] Additionally, molecular tethers could hierarchically assemble dissimilar nanoparticles with precisely controlled energy levels and surface chemistry to funnel energy to a subset of nanoparticles that act as reaction centers.[54] In this scheme, the absorption cross-section of the reaction center is effectively enhanced by nearby photosensitizing particles, and several redox equivalents can be rapidly shuttled to the same active site, increasing the efficiency of multi-electron/hole reactions. Molecular ligands that tune the energy levels of a colloidal nanocrystals through electrostatic effects or orbital mixing could also be used to customize systems for a targeted reaction.[55]

1.5 Dissertation Outline

This dissertation focuses on gathering insights on how to tune and control the light-induced electronic behavior at the interfaces of MDHJs. The fundamental understanding of how different classes of nanomaterials can complement each other will drive rational design for their use in various optoelectronic applications, such as but not limited to those described above. There are myriad factors that can be used to control the behavior at the interface. Chapter 2 describes a static way of controlling the physics through altering the interfacial morphology. The way that phthalocyanine molecules lie on the surface of a 2D material directly informs the interfacial charge separation lifetimes. Chapter 3 describes a more dynamic means of control through the use of a remote light field. Photoswitchable molecules bound to the surface of the QD can accept electrons from the QD at different rates, which controls the QD PL. Chapter 4 opens the door for sensitizing chemically reactive 2D materials by exploiting the long-range EnT from QDs. The close-packed nature of the QD donor film and the bulk nature of the black phosphorus (BP) acceptors enable EnT to sensitize BP through a protective alumina encapsulation layer. Chapter 6 explores further

possibilities building on these concepts (interfacial morphology, external stimuli, and chemically reactive 2D materials) and also posits other opportunities in exciton delocalization, spin selectivity, and quantum emission to obtain even more exotic and emergent behavior from MDHJ interfaces.

While all of this fundamental research is intriguing for the possibilities of furthering knowledge in this area, there are also opportunities to explain this research to lay audiences. Most STEM outreach focuses on children, and Chapter 5 describes the development of a program to engage voting age audiences, namely senior citizens, to inform them about current science happening at NU. After all, science does not end when one submits a paper; scientists have a duty to share their findings with their broader communities.

Chapter 2: Molecular-Orientation-Dependent Interfacial Charge Transfer in Phthalocyanine/MoS_2 Mixed Dimensional Heterojunctions

Adapted from:

Padgaonkar, S.; Amsterdam, S. H.; Bergeron, H.; Su, K.; Marks, T. J.; Hersam, M. C.; Weiss, E. A., *Journal of Physical Chemistry: C*, **2019**, *123* (21), 13337-13343.

2.1 Chapter Summary

Mixed-dimensional heterojunctions (MDHJs) combine the characteristics of component materials such as the discrete orbital energies of zero-dimensional (0D) molecules and the extended band structure of two-dimensional (2D) semiconductors. Here, time-resolved spectroscopy reveals sub-picosecond photoinduced hole transfer and sub-320-fs photoinduced electron transfer processes at the interfaces of type-II copper and free-base phthalocyanine/monolayer MoS_2 MDHJs. In CuPc/MoS_2 heterojunctions, charge separation lasts as long as 70 ns, which is a factor of 17 longer than in H_2Pc/MoS_2 heterojunctions and a factor of 40 longer than in previously reported transition metal dichalcogenide-based heterojunctions. Preservation of the charge separated state is attributed to the face-on orientation of CuPc on the MoS_2 surface, which templates stacking of CuPc molecules and facilitates hole migration away from the interface, whereas H_2Pc molecules adopt a mixed edge-on and face-on orientation. This work highlights the role of molecular structure in determining the interfacial geometry and, ultimately, charge transfer dynamics in 0D/2D heterojunctions.

2.2 Introduction

The high charge carrier mobilities, strong optical absorption, and mechanical resilience of two-dimensional (2D) semiconductors make these materials prime candidates for next-generation flexible optoelectronic applications.[56,57] For example, monolayer MoS_2, a transition metal dichalcogenide (TMDC), has garnered interest as an electron accepting charge transport layer for photovoltaics[58–61] and photodetectors[62,63] because of its visible-wavelength absorption, direct bandgap, and *n*-type doping. To enhance the coupling of 2D materials with light for use in optoelectronic or photovoltaic applications, 2D materials are often interfaced with chromophoric

zero-dimensional (0D) materials such as organic molecules,[58] polymers,[59] and colloidal quantum dots[64,65] in mixed-dimensional heterojunctions (MDHJs).[66] In organic/2D heterojunctions,[60,61,67–70] picosecond or sub-picosecond-timescale photoinduced charge transfer leading to charge-separated states with nanosecond lifetimes (up to a factor of ten longer lifetimes than 2D/2D junctions) has been observed,[71,72] but the relationships between molecular structure and orientation on the 2D material surface and the resulting photophysical processes have not yet been explored systematically.

Here, we study rates and yields of charge separation and charge recombination in MDHJs of copper phthalocyanine (CuPc) or free-base phthalocyanine (H_2Pc) and monolayer MoS_2. In previous studies, phthalocyanines have been shown to passivate defects,[73] modulate doping,[74] and improve rise times in MoS_2-based phototransistors.[63,75] More relevant to this work, varying the metal center modifies excitonic properties,[76] including diffusion length and mobility, in organic heterojunctions[77] and the electronic coupling with MoS_2.[70] With a combination of transient absorption and polarized Raman spectroscopies, we focus here on the role of the metal center in determining molecular orientation within the heterojunction, and thereby the formation and decay rates of the charge-separated state. We observe that CuPc molecules lie primarily π-face-on on the MoS_2 basal plane, whereas H_2Pc molecules adopt a mixed edge-on and π-face-on orientation. While the sub-picosecond charge separation time constants are similar in the two heterojunctions, charge-separated states within CuPc/MoS_2 live up to a factor of 17 longer than in H_2Pc/MoS_2, and a factor of 40 longer than in any previously reported TMDC-based heterojunction. We propose this lifetime is attributable to high hole mobility away from the interfacial region through the stacks of CuPc, templated by their face-on orientation on MoS_2.[71,72]

2.3 Results and Discussion

2.3.1 Steady State Characterization of Pc/MoS_2 Heterostructures

MoS_2 was grown by chemical vapor deposition with >99% coverage on sapphire substrates; 89% is monolayer and 11% is multilayer crystals.[78] To form heterojunctions, we thermally evaporated a CuPc film with a thickness of 5 nm on top of the MoS_2. This thickness is the thinnest layer that yields reliable signals from CuPc in the time-resolved optical experiments. Based on reported energy levels, CuPc and MoS_2 form a type-II heterojunction, where both electron transfer (eT) from photoexcited CuPc to the MoS_2 conduction band (CB) and hole transfer (hT) from photoexcited MoS_2 to the CuPc highest occupied molecular orbital (HOMO) are energetically allowed (**Figure 2.1**).[79,80]

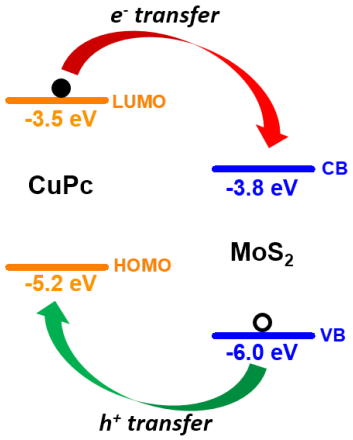

Figure 2.1. Type II heterojunction formed from CuPc/MoS_2 and the favorable charge transfer pathways. Since H_2Pc has similar HOMO and LUMO levels to CuPc, the energy level alignment in that junction is similar.

Figure 2.2a is a Jablonski diagram depicting these charge transfer processes in addition to other competitive decay pathways. **Figure 2.2b** shows the measured ground-state absorption spectra of the "control" samples (monolayer MoS_2 and vapor-deposited 5-nm-thick CuPc, both on sapphire). The CuPc spectrum has Q-band absorption peaks at 623 nm and 705 nm, ascribed to two π-π* transitions,[81] and the MoS_2 spectrum has peaks corresponding to the so-called "A" (662 nm) and "B" (611 nm) excitons. The measured absorbance of the heterojunction is greater in some spectral regions than the sum of the individual component absorbances (green dashed line). The adsorption of CuPc on MoS_2 enhances the vibronic transitions within the Q-band of CuPc by ~40%. **Figure 2.2b** also shows the excitation wavelengths used in the transient absorption (TA) study of these samples: MoS_2 is selectively excited within the heterojunction using a 510-nm pump, and CuPc is selectively excited within the heterojunction using a 705-nm pump.

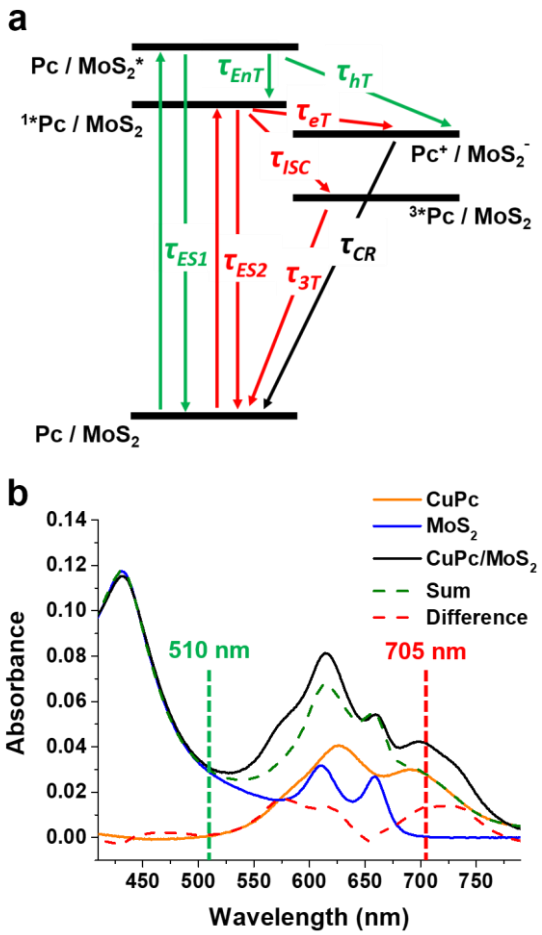

Figure 2.2. (a) Jablonski diagram illustrating the photophysical pathways in the MDHJ, with associated time constants, τ. ES1 is MoS_2 excited state decay, ISC is intersystem crossing, eT is electron transfer, hT is hole transfer, EnT is energy transfer, ES2 is ^{1*}Pc decay, 3T is ^{3*}Pc decay, and CR is charge recombination. **(b)** Individual ground-state absorption spectra of CuPc (orange), MoS_2 (blue), and the MDHJ thin film (black), the sum of the orange CuPc and blue MoS_2 traces (dashed green), and the difference between the MDHJ spectrum and the sum of individual component spectra (dashed red). All films are deposited on single-crystal sapphire. The pump wavelengths used in TA experiments are indicated by the dashed lines.

2.3.2 Ultrafast Hole Transfer from MoS_2 to Pc

For TA measurements across different samples, we chose a pump wavelength that would generate an exciton density of 3 x 10^{18} cm^{-3} when exciting MoS_2 and 7 x 10^{18} cm^{-3} when exciting Pc to maximize signal while minimizing biexcitonic effects. **Figure 2.3a** shows the TA spectra (time delay = 375 fs) of MoS_2 pumped at 510 nm (blue) and CuPc pumped at 705 nm (orange) for the control samples. The spectra are dominated by the ground state bleaches (GSBs) of the respective materials, corresponding to the A (662 nm) and B (614 nm) excitons of MoS_2, and to the Q-band transitions of CuPc (630 nm, 720 nm). The TA spectrum of CuPc also contains a broad excited state absorption (ESA) between 450 nm and ~600 nm that changes the shape of the GSB features relative to those of the ground state absorption spectrum (**Figure 2.2b**). While these ESA and the GSB features at 630 nm are nearly identical for the lowest-energy singlet and triplet excited states (^{1*}CuPc and ^{3*}CuPc, respectively), the two states can be distinguished by the 720-nm GSB, which decays upon intersystem crossing (**Figure 2.4**).[82–86] Monitoring the dynamics at 730 nm (where pump scatter effects are minimal) in the CuPc-only TA spectrum after pumping at 705 nm yields an intersystem crossing time constant of 620 ± 70 fs, consistent with the literature (**Figure 2.5**).[85,86]

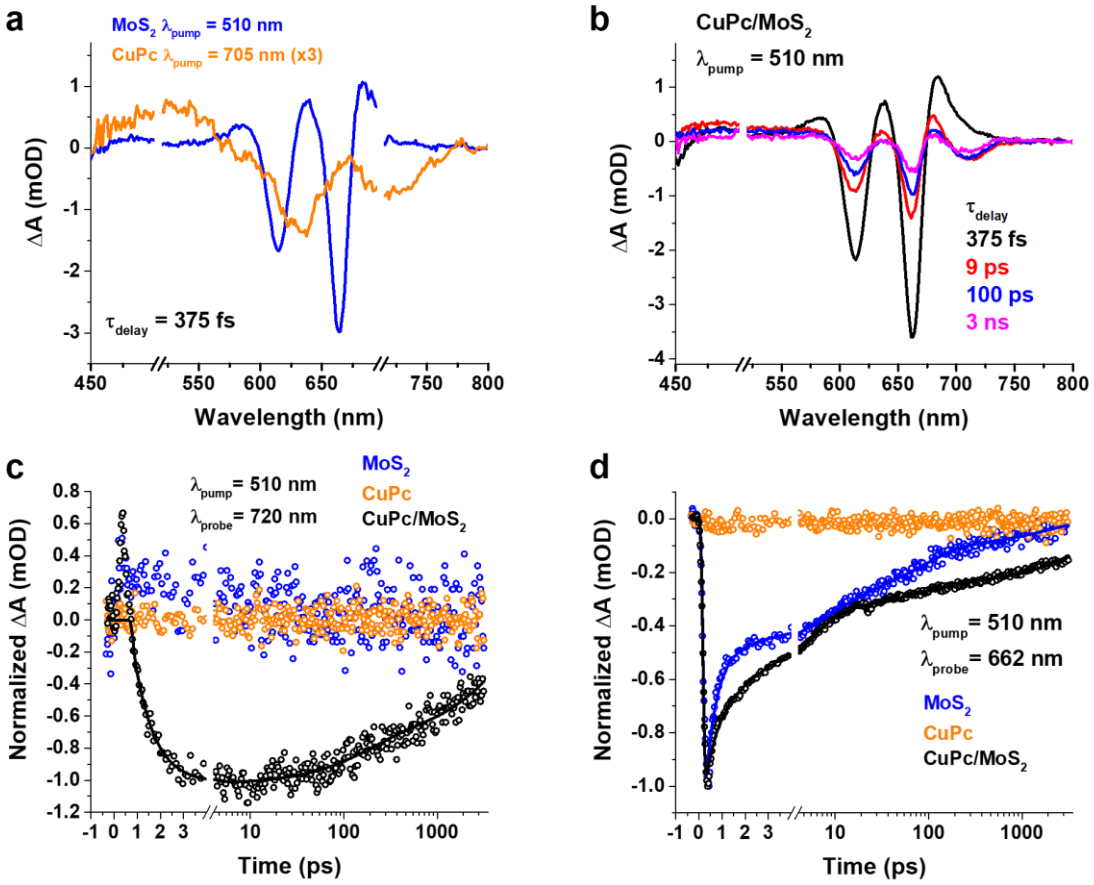

Figure 2.3. (a) TA spectra of MoS_2 (blue) pumped at 510 nm and CuPc (orange, magnified by 3x for clarity) pumped at 705 nm at a time delay of 375 fs. The regions between 500-520 nm, as well as 695-715 nm are inaccessible due to pump scatter. **(b)** TA spectra of the CuPc/MoS_2 heterojunction pumped at 510 nm to form CuPc/MoS_2^* at varying time delays between 375 fs and 3 ns. Normalized kinetic traces extracted at **(c)** 720 nm (Q-band of CuPc) and **(d)** 662 nm (A exciton of MoS_2) from the TA spectra of CuPc (orange), MoS_2 (blue), and CuPc/MoS_2 heterojunction (black) films pumped at 510 nm. We fit the traces in (c) and (d) to obtain a time constant for charge separation by hole transfer (CuPc/$^{1*}MoS_2$ → $CuPc^{+\bullet}/MoS_2^-$) of 880 ± 110 fs. Kinetic traces were fit with multiexponential functions convoluted with the instrument response function (IRF). TA spectra were acquired at a pump fluence (3.2 μJ/cm^2 at 510 nm and 7 μJ/cm^2 at 705 nm) to ensure a low initial excitation density (7 × 10^{18} cm^{-3} and 3 × 10^{18} cm^{-3}) in the samples.

Figure 2.3b shows the TA spectrum of the heterojunction after pumping at 510 nm, where >99% of absorbed photons excite the MoS_2. As expected, this spectrum is dominated by the MoS_2 GSBs and ESAs at a time delay of 375 fs (black). By 9 ps, however, the CuPc GSB centered at ~720 nm is clearly present (red), even though CuPc alone has no optical response at this pump

wavelength (**Figure 2.3c**, orange). The black trace in **Figure 2.3c** shows the growth of the CuPc GSP feature; a fit to this trace reveals that the CuPc ground state is depleted in 880 ± 110 fs upon excitation of the MoS_2, and remains depleted out to 3 ns (**Figure 2.3b**). Furthermore, the 720-nm GSB in this spectrum is not accompanied by an ESA in the 480-nm region at any delay time. These two observations indicate that the transient species of CuPc produced in 880 ± 110 fs is $CuPc^{+\bullet}$ (**Figure 2.6**), not ^{1*}CuPc, which has the ESA and a sub-ps decay of the GSB at 720 nm, or ^{3*}CuPc, which has the ESA and no GSB at 720 nm. The charge separation that forms $CuPc^{+\bullet}$ could be accomplished either by direct hT from photoexcited MoS_2 or by Förster energy transfer from photoexcited MoS_2 followed by eT from CuPc to MoS_2. Förster energy transfer is possible given that the MoS_2 emission overlaps with the CuPc absorption (**Figure 2.7**), and as we show below, the eT from CuPc to MoS_2 is faster than the instrument response function (IRF), so a detectable population of the ^{1*}CuPc intermediate is not expected to accumulate during this process. We therefore cannot distinguish between these two pathways to $CuPc^{+\bullet}/MoS_2^{-}$, but we would expect both to be operative given the range of donor-acceptor distances in this MDHJ (from directly adjacent to ~5 nm).

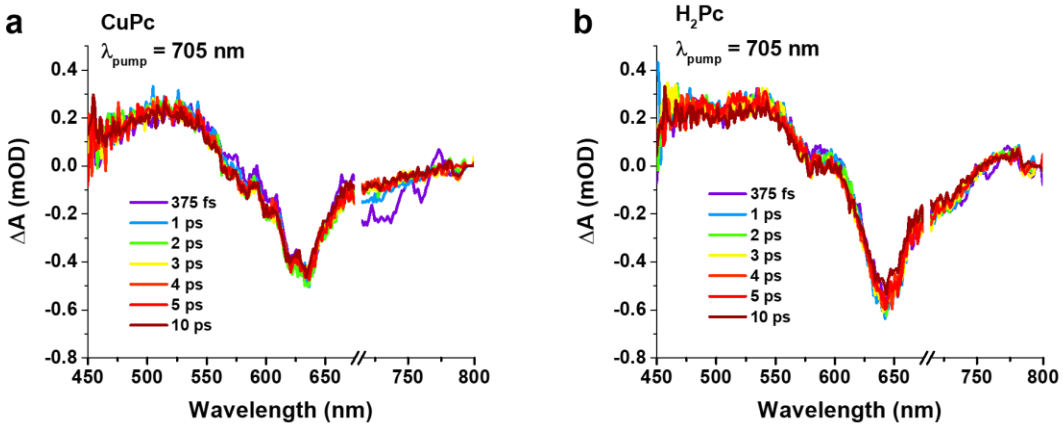

Figure 2.4. TA spectra of **(a)** CuPc and **(b)** H_2Pc with varying time delays between 0 and 10 ps after excitation at 705 nm. The GSB centered at 720 nm decays much faster in CuPc than H_2Pc. Wavelengths between 695 nm and 715 nm are inaccessible due to pump scatter.

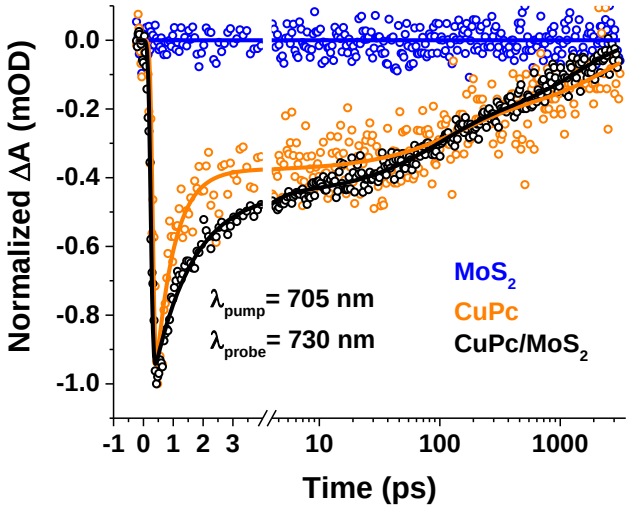

Figure 2.5. Kinetic traces extracted at 730 nm (Q-band of CuPc) from the TA spectra of CuPc (orange), MoS_2 (blue), and CuPc/MoS_2 heterojunction (black) after pumping at 705 nm.

Our proposal that charge separation is occurring from MoS_2^* to form $CuPc^{+\bullet}/MoS_2^-$ is further supported by the observation that, in the MDHJ, 15% of the MoS_2 transient species responsible for the GSB remains after 3 ns, whereas only 1% of these species remains after 3 ns in the MoS_2-only sample (**Figure 2.2d**, compare blue to black, and **Table 2.1**). This result indicates that at least

a portion of the GSB in the MDHJ is due to MoS_2^-.[60,61] **Figure 2.2d** shows that the decay of the MoS_2 GSB on the 0 – 10 ps timescale is also slower in the presence of CuPc, which is likely attributable to the adsorbed CuPc on MoS_2 suppressing 480-fs carrier trapping by passivating surface defects.[73,87] We therefore conclude that $CuPc^{+\bullet}/MoS_2^-$ evolves from $^{1*}MoS_2$ within the MDHJ with a time constant of 880 ± 110 fs, either by direct hT or a combination of energy transfer and eT, **Table 2.1**.

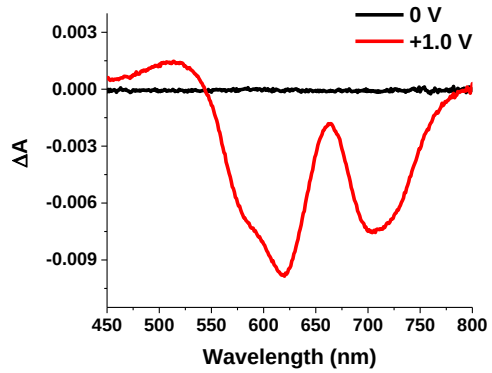

Figure 2.6. Spectroelectrochemistry of a 40-nm film of CuPc on ITO/glass at a potential of 0 V (black) and +1.0 V (red) versus an Ag wire in a 1M KCl aqueous solution.

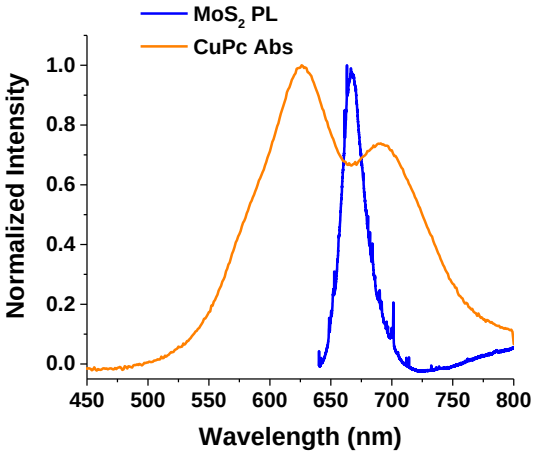

Figure 2.7. Normalized spectra of MoS_2 PL emission (blue) and CuPc absorption (orange).

Table 2.1. Time Constants (τ_1) and Amplitudes (A_1) Extracted from Fits to the Kinetic Traces of the Decay of the MoS_2 A Exciton GSB (λ_{probe}= 662 nm).[a]

Sample	λ_{pump}, nm	τ_1 (A_1)	τ_2 (A_2)	τ_3 (A_3)	τ_4 (A_4)	τ_5 (A_5)	τ_6 (A_6)
		Carrier trapping[b]	hT[c]/BET[d]	Exciton scattering	Rad. recomb. /e^- trapping	Rad. recomb. from trapped carriers	CR[e]
MoS_2 (used for CuPc)	510	480 ± 30 fs (54 ± 2%)		8.1 ± 1.3 ps (19 ± 1%)	84 ± 11 ps (19 ± 1%)	2.1 ± 0.3 ns (9 ± 1%)	
CuPc/MoS_2	510	480 fs (27 ± 1%)	4.1 ± 0.1 ps[c] (41 ± 1%)		98 ± 11 ps (9 ± 1%)		5.9 ± 0.4 ns (23 ± 1%)
CuPc/MoS_2	705		2.7 ± 0.1 ps[d] (53 ± 1%)		390 ± 70 ps (10 ± 1%)		5.9 ns[f] (22 ± 4%)
MoS_2 (used for H_2Pc)	510	380 ± 20 fs (54 ± 1%)		6.7 ± 0.5 ps (23 ± 1%)	85 ± 5 ps (23 ± 1%)	2.2 ± 0.2 ns (12 ± 1%)	
H_2Pc/MoS_2	510	380 fs (29 ± 1%)	4.7 ± 0.1 ps[c] (52 ± 1%)		50 ± 4 ps (15 ± 1%)	2.6 ± 0.4 ns (4 ± 1%)	
H_2Pc/MoS_2	705		6.3 ± 0.2 ps[d] (53 ± 1%)		55 ± 2 ps (38 ± 1%)		4.0 ± 0.5 ns (9 ± 1%)

[a]$\Sigma A_n = 1$. [b]The exciton decay dynamics for MoS_2 have been extensively studied.[60,88,89] [c]This component is likely due to hole transfer from MoS_2 to CuPc but is possibly convoluted with energy transfer (EnT). [d]This component is possibly due to back electron transfer (BET) or convoluted with phonon scattering[67]. [e]"CR" = charge recombination. **[f]An additional component of >10 ns (15%) was needed to complete this fit for fs-TA. With ns-TA, we find that this signal decays with two time constants: 4.3 ± 0.9 ns (65%) and 70 ± 25 ns (35%).**

2.3.3 Ultrafast Electron Transfer from Pc to MoS_2

Figure 2.8a shows the TA spectra of the CuPc/MoS_2 heterojunction films after excitation at 705 nm, where >99% of absorbed photons excite the CuPc. At a pump-probe delay of 375 fs, the spectrum contains the GSB (at 720 nm) and the ESA (at ~480 nm) characteristic of ^{1*}CuPc, as expected since CuPc is being directly photoexcited. The non-trivial result is that the spectrum at

this delay is dominated by MoS_2 GSB and ESA features. Since isolated MoS_2 does not have any transient features when excited directly at 705 nm, this result indicates that these features are due to instrument response function (IRF)-limited eT from ^{1*}CuPc to the MoS_2 CB (hole and energy transfer are energetically uphill). This result is consistent with previous measurements of IRF-limited eT from ZnPc to MoS_2,[67,90] and from PTB7 to MoS_2.[61] At a delay time of 3 ns after pumping at 705 nm (**Figure 2.8a**, pink), the ESA at 480 nm has disappeared, but the GSBs of CuPc at 720 nm and MoS_2 at 614 nm and 662 nm remain, again indicating the presence of the eT product: $CuPc^{+\bullet}/MoS_2^{-}$.

The final piece of evidence that $CuPc^{+\bullet}/MoS_2^{-}$ evolves from ^{1*}CuPc in the MDHJ is that the average lifetime of the A-exciton GSB of MoS_2 in the MDHJ, formed after pumping CuPc at 705 nm, is a factor of 55 longer than that of isolated MoS_2 and even a factor of nine longer than the MDHJ pumped at 510 nm (**Tables 2.1 and 2.2**). These results are reasonable given that all of the A-exciton GSB is attributable to the longer-lived MoS_2^{-} species when pumping at 705 nm, but some fraction of it is attributable to $^{1*}MoS_2$ when pumping at 510 nm.

We therefore conclude that $CuPc^{+\bullet}/MoS_2^{-}$ forms from ^{1*}CuPc within the present MDHJ by eT with a time constant of <320 fs (the IRF of our system), **Table 2.3.** Notably, the 620-fs dynamic signature of ISC (^{1*}CuPc → ^{3*}CuPc) is missing in the kinetic trace extracted from the GSB of CuPc in the CuPc/MoS_2 MDHJ TA spectrum after pumping the CuPc at 705 nm (**Table 2.2**), so it appears that photoinduced eT from CuPc to MoS_2 out-competes sub-picosecond ISC.

Table 2.2. Time Constants (τ_1) and Amplitudes (A_1) Extracted from Fits to the Kinetic Traces of the Decay of the Pc GSB (λ_{probe}= 720 or 730 nm).[a]

Sample	λ_{pump}, nm	τ_1 (A_1)	τ_2 (A_2)	τ_3 (A_3)	τ_4 (A_4)	τ_5 (A_5)	τ_6 (A_6)
		ISC[b]	hT[c]	BET[d]			CR[e]
CuPc	705	620 ± 70 fs (65 ± 4%)			130 ± 50 ps (14 ± 2%)	2.6 ± 0.7 ns (21 ± 2%)	
CuPc/MoS_2	705			1.3 ± 0.1 ps (56 ± 1%)	87 ± 10 ps (20 ± 1%)	1.4 ± 0.1 ns (25 ± 1%)	
CuPc/MoS_2	510		880 ± 110 fs[c]		170 ± 50 ps (28 ± 4%)		4.9 ± 0.8 ns (72 ± 4%)
H_2Pc	705	2.1 ± 0.9 ps (23 ± 5%)			43 ± 9 ps (55 ± 5%)	450 ± 160 ps (22 ± 6%)	
H_2Pc/MoS_2	705			9.9 ± 0.7 ps (40 ± 2%)	84 ± 7 ps (33 ± 2%)	6.6 ± 0.7 ns (27 ± 1%)	
H_2Pc/MoS_2	510		780 ± 100 fs[c]		83 ± 14 ps (24 ± 1%)		8.5 ± 1.0 ns (76 ± 1%)

[a]ΣA_n = 1, 720 nm was used for CuPc samples and 730 nm was used for H_2Pc samples. [b]"ISC" = intersystem crossing. [c]This component is likely due to hole transfer (hT) but likely convoluted with energy transfer (EnT). [d]"BET" = back electron transfer. [e]"CR" = charge recombination.

2.3.4 Lifetime of Charge-Separated States

We next determine the lifetimes of the charge-separated state $CuPc^{+\bullet}/MoS_2^-$ from the decays of the CuPc and MoS_2 GSBs. After inducing charge separation by pumping MoS_2 at 510 nm, $CuPc^{+\bullet}$ (monitored at 720 nm) decays primarily with a time constant of 4.9 ± 0.8 ns, **Figure 2.3c**, and MoS_2^- decays primarily with a time constant of 5.6 ± 0.3 ns (monitored at 662 nm), **Figure 2.3d**. A population of $CuPc^{+\bullet}/MoS_2^-$ therefore lives for ~5 ns. In both kinetic traces, an additional charge recombination process is observed that is longer than the present 3-ns time window, but a limited signal-to-noise ratio limits accurate characterization at this longer timescale. However,

when the MDHJ at 705 nm is pumped, a higher density of $CuPc^{+\bullet}/MoS_2^-$ states is created, and the charge recombination process on both the ps - ns and ns - μs timescales can be monitored, **Figures 2.8b** and **2.8c**, respectively. Fits to these kinetic traces for the MDHJ yield time constants of 4.3 ± 0.9 ns, in agreement with the charge recombination time obtained by pumping at 510 nm, and 70 ± 25 ns (**Tables 2.1, 2.2, and 2.3**). The 70-ns lifetime, which accounts for 35% of the population of $CuPc^{+\bullet}/MoS_2^-$ states, is at least a factor of ten greater than the reported lifetime of any charge-separated state in a TMDC-based heterojunction.[60,61,67–69,71,72]

Comparison of the structure and photophysics of the $CuPc/MoS_2$ heterojunction to that of an H_2Pc/MoS_2 heterojunction highlights the influence of interfacial geometry on charge transfer in this system. The steady state absorption features of H_2Pc and its heterojunction with MoS_2 are similar to those of CuPc, including the enhanced absorption of the Q-band in the MDHJ. **Figure 2.9a** (black) shows that, as in the $CuPc/MoS_2$ heterojunction, the GSB of H_2Pc emerges in less than 1 ps (specifically, 780 ± 100 fs) when MoS_2 is selectively excited. The lifetime of the MoS_2 GSB within this MDHJ is shorter than that of MoS_2 alone, **Figure 2.9b**, so it cannot be pure MoS_2^* and must instead be a mixture of MoS_2^* and MoS_2^-, where the lifetime of the charge-separated state $H_2Pc^{+\bullet}/MoS_2^-$ is, on average, shorter than that of MoS_2 alone. We therefore conclude that $H_2Pc^{+\bullet}/MoS_2^-$ forms upon excitation of MoS_2.

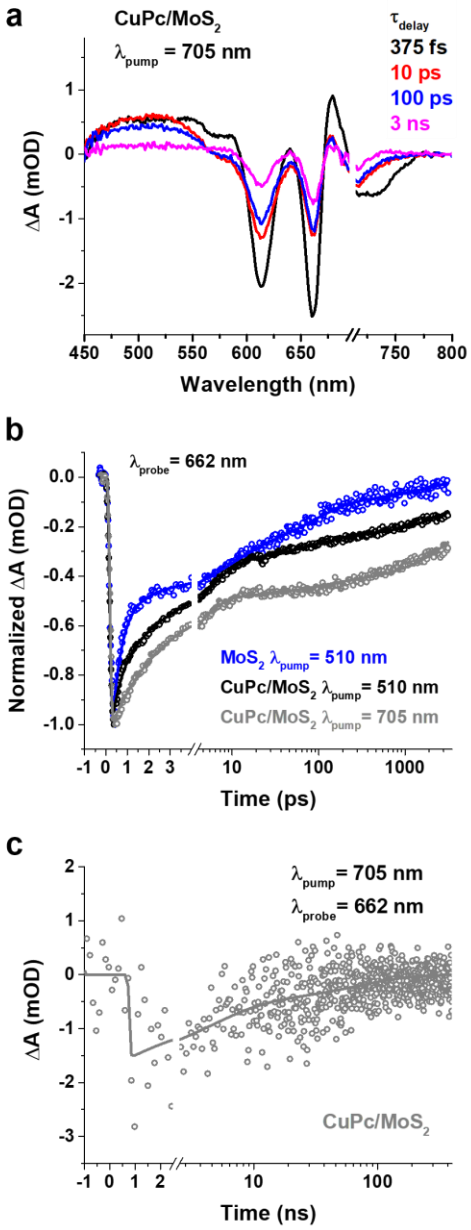

Figure 2.8. (a) TA spectra of CuPc/MoS_2 heterojunction pumped at 705 nm to form ^{1*}Pc/MoS_2). at varying time delays between 375 fs and 3 ns. **(b)** Normalized kinetic traces extracted at 662 nm (A exciton of MoS_2) from the TA spectra of MoS_2 (blue) pumped at 510 nm, the CuPc/MoS_2 heterojunction (black) pumped at 510 nm, and the CuPc/MoS_2 heterojunction (gray) pumped at 705 nm. Fits to the kinetic traces of the heterojunctions yield one of the time constants for charge recombination of the $CuPc^{+\bullet}/MoS_2^{-}$ state, 4.3 ± 0.9 ns. **(c)** Kinetic traces from ns-TA spectrum of CuPc/MoS_2 heterojunction pumped at 705 nm. A fit of this trace yields a second time constant for charge recombination of the $CuPc^{+\bullet}/MoS_2^{-}$ state, 70 ns.

Figure 2.9c shows that when H_2Pc is excited at 705 nm, MoS_2 GSBs dominate the TA spectra at the first measureable time points, which, as in the case of the CuPc/MoS_2 heterojunction, indicates that photoinduced eT from H_2Pc to MoS_2 occurs occurring faster than we can measure. As is the case with 510-nm excitation, the $H_2Pc^{+\bullet}/MoS_2^-$ state formed by eT is almost entirely absent by 3 ns (**Figure 2.9c**, red trace). A fit to the kinetic trace extracted at 662 nm after pumping at 705 nm (**Figure 2.10**) indicates that the $H_2Pc^{+\bullet}/MoS_2^-$ charge-separated state lives for 4.0 ± 0.5 ns (**Tables 2.1 and 2.2**), and, importantly, has no 70-ns lifetime, as observed for $CuPc^{+\bullet}/MoS_2^-$, **Table 2.3**.

Table 2.3. Time constants (τ) of electron transfer (eT), hole transfer (hT), and charge recombination (CR) in CuPc/MoS_2 and H_2Pc/MoS_2 MDHJs.

Time Constant, τ (=1/*k*)	CuPc	H_2Pc
τ_{hT} ($Pc/^{1*}MoS_2 \rightarrow Pc^{+\bullet}/MoS_2^-$) [a]	880 ± 110 fs	780 ± 100 fs
τ_{eT} ($^{1*}Pc/MoS_2 \rightarrow Pc^{+\bullet}/MoS_2^-$)	<320 fs [b]	<320 fs [b]
τ_{CR} ($Pc^{+\bullet}/MoS_2^- \rightarrow Pc/MoS_2$)	4.3 ± 0.9 ns (65%), 70 ± 25 ns (35%)	4.0 ± 0.5 ns

[a] This net hole transfer may be the sum of two processes: energy transfer ($Pc/^{1*}MoS_2 \rightarrow {}^{1*}Pc/MoS_2$) followed by electron transfer ($^{1*}Pc/MoS_2 \rightarrow Pc^{+\bullet}/MoS_2$); the time constant is therefore possibly a convolution of those two time constants

[b] The instrument response function (IRF) is 320 ± 20 fs, as measured by a Gaussian fit to the optical Kerr effect response of sapphire in the glass cuvette.

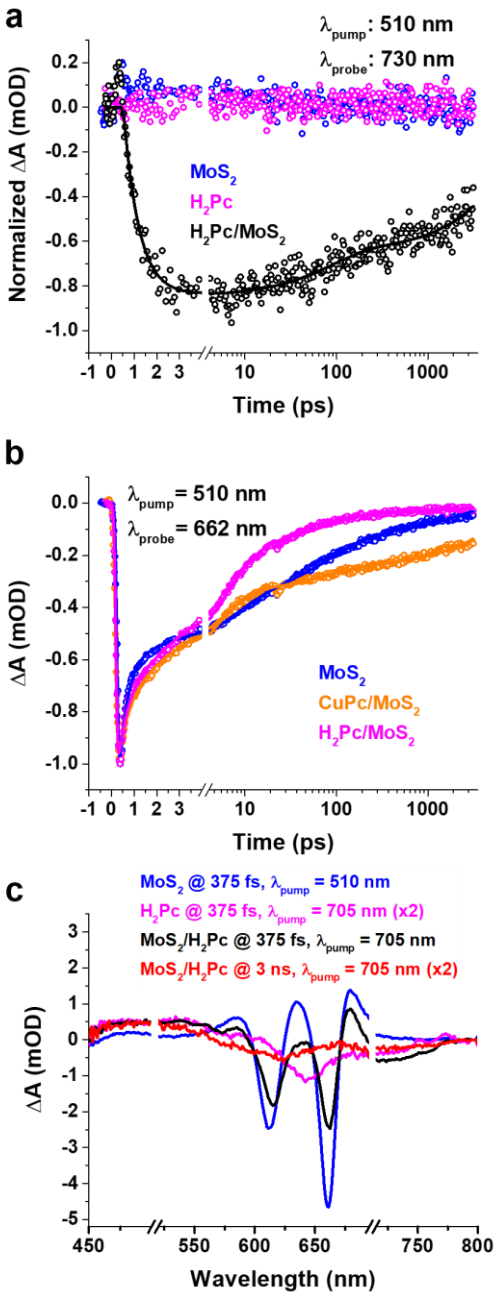

Figure 2.9. (a) Normalized kinetic traces extracted at 730 nm (Q-band of H_2Pc) from the TA spectra of H_2Pc (pink), MoS_2 (blue), and H_2Pc/MoS_2 heterojunction (black) films pumped at 510 nm. A fit of the black trace yields a time constant for charge separation by hole transfer ($H_2Pc/^{1*}MoS_2 \rightarrow H_2Pc^{+\bullet}/MoS_2^{-}$) of 780 ± 100 fs. **(b)** Normalized kinetic traces extracted at 662 nm from the TA spectra of MoS_2 (blue), $CuPc/MoS_2$ (orange), and H_2Pc/MoS_2 (pink) pumped at 510 nm. A fit of the kinetic trace of the heterojunction (pink) yields a time constant for charge recombination of the $H_2Pc^{+\bullet}/MoS_2^{-}$ state of 4.0 ± 0.5 ns. **(c)** TA spectra of MoS_2 at 375 fs (blue) pumped at 510 nm, H_2Pc at 375 fs (pink, magnified by 2× for clarity) pumped at 705 nm, and H_2Pc/MoS_2 heterojunction at 375 fs (black) and 3 ns (red, magnified by 2× for clarity) pumped at 705 nm.

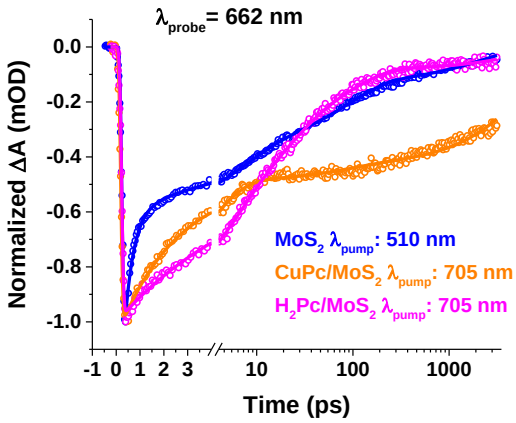

Figure 2.10. Normalized kinetic traces extracted at 662 nm (A exciton of MoS_2) from the TA spectra of MoS_2 (blue), CuPc/MoS_2 (orange), and H_2Pc/MoS_2 (pink) at different excitation wavelengths.

2.3.5 Dependence of Charge Separation on Molecular Orientation

Figures 2.11a and **2.11b** show the polarized Raman spectra of CuPc and H_2Pc, respectively, when deposited on sapphire and MoS_2. For polarized Raman experiments, the sample is excited

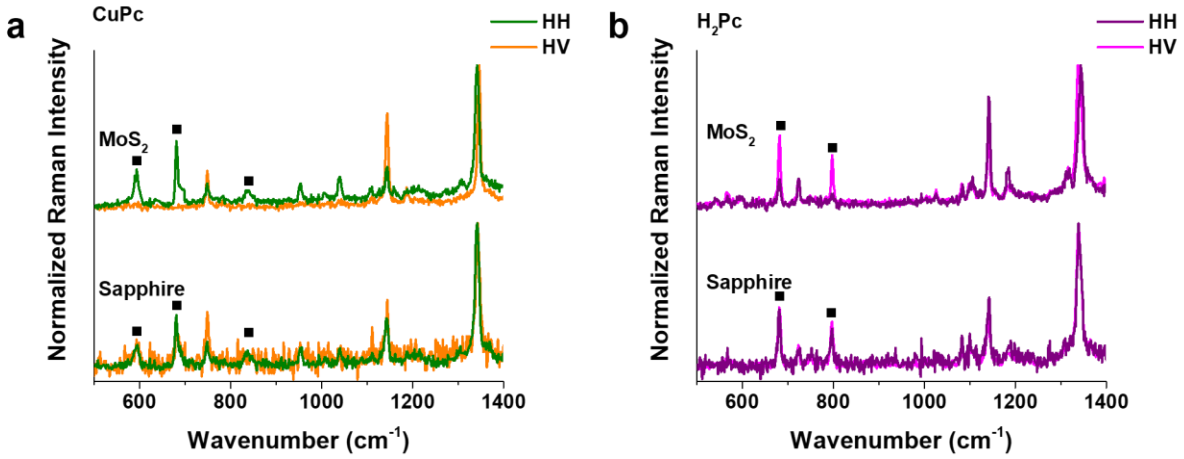

Figure 2.11. Normalized Raman spectra of **(a)** CuPc and **(b)** H_2Pc on single-crystal sapphire and MoS_2 with detection of horizontal (HH, green for CuPc and purple for H_2Pc) and vertical (HV, orange for CuPc and pink for H_2Pc) polarization. A_{1g} modes are denoted by black squares. Raman spectra were acquired for 60 s in a confocal microscope with 532 nm excitation and 1800 gr/mm. The spectra are normalized to the intensity of the 1340 cm^{-1} peak.

with 532 nm plane-polarized light, where the parallel (HH) and perpendicular (HV) light are selectively collected using a polarized filter. While Raman peaks associated with the A_{1g} modes (580, 670, 825 cm^{-1}) of CuPc are observed with both HV and HH modes for CuPc/sapphire, these features are only present with HH and not HV for CuPc/MoS_2. These data indicate that the CuPc is lying primarily "π-face-on" on MoS_2, but adopts mixed face-on and edge-on orientations on sapphire, in agreement with prior results.[91] Peaks at 680 cm^{-1} and 800 cm^{-1}, which are the A_{1g} modes of H_2Pc, are present in the spectrum acquired in HV mode both on sapphire and MoS_2, indicating a mixed orientation on both substrates.[92] While we are unable to obtain CuPc photoluminescence (PL) since the PL quantum yield is low due to ISC, the broad (full-width half-maximum of 140 nm) H_2Pc PL peak centered at 850 nm on both sapphire and MoS_2 (**Figure 2.12**) further confirms that H_2Pc does not lie π-face-on on MoS_2 since purely π-face-on orientation is evidenced by a sharp peak (full-width half maximum = 25 nm) centered at 700 nm.[93]

From these results, we suggest that the Cu(II) metal center can play two roles in this MDHJ. First, it promotes π-face-on orientation of the CuPc on MoS_2, potentially via axial coordination of

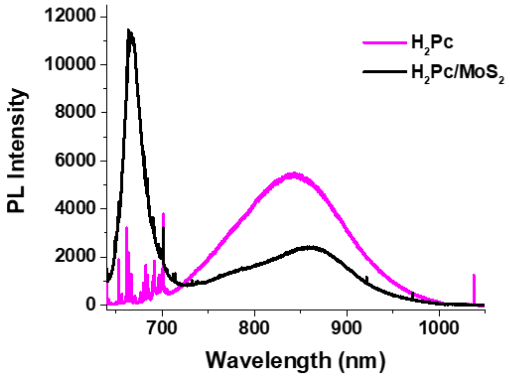

Figure 2.12. PL spectra of H_2Pc on sapphire (pink) and MoS_2 (black). PL spectra were acquired for 10 s in a confocal microscope with 633 nm excitation and 600 gr/mm.

the Cu metal center to an MoS_2 basal sulfur atom. Second, this π-face-on molecular orientation of the CuPc layer templates the face-to-face growth of additional CuPc molecular layers on the MoS_2.[94] Such stacks should enable rapid hole migration away from the hetero-interface, thereby decreasing the effective electron-hole Coulomb interaction and enabling an exceptionally long lifetime (70 ns) of the charge-separated state.[95] This out-of-plane hole mobility is further enhanced by the Cu metal centers in CuPc (as opposed to no metal center in H_2Pc), which serve as hole hopping sites.[77]

2.4 Experimental Details

2.4.1 Synthesis and Characterization of MoS_2

Continuous monolayer MoS_2 was grown directly on sapphire with chemical vapor deposition (CVD) as described elsewhere (**Figure 2.13a**).[78] Using a previously reported procedure, we binarized optical microscopy images to quantify the amount of monolayer and bilayer coverage in the area used for transient absorption spectroscopy (**Figure 2.13b** and **Table 2.4**).[59]

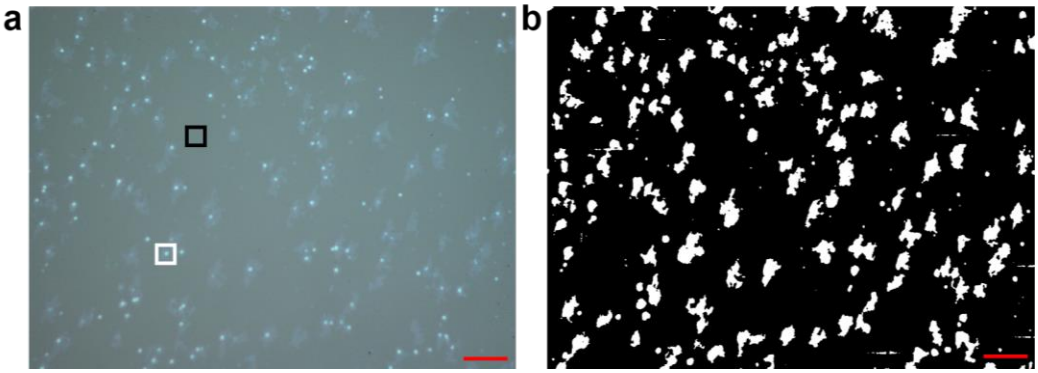

Figure 2.13. (a) Representative optical micrograph of CVD-grown MoS_2 on sapphire with black and white squares highlighting areas of monolayer growth and bilayer growth, respectively. **(b)** Binarized image of the same micrograph to quantify the ratio of monolayer and bilayer growth. A collection of similar images was used to determine the overall percentage of monolayer MoS_2. The red scale bar is 20 μm.

Table 2.4. Summary of Percentages of Black/white Channels from the Binarized image.

	Percentage	Error
Monolayer (black)	89.6%	1%
Bilayer (white)	10.4%	1%

2.4.2 Preparation of the Heterojunction

CuPc and H_2Pc (Sigma-Aldrich) were purified by temperature gradient sublimation and deposited by thermal evaporation similarly to literature procedures.[70] Briefly, in a thermal evaporator in a nitrogen glovebox, Pc powder was placed in an alumina boat and pumped below 10^{-5} torr for 30 minutes. We increased the current through the boat until the deposition rate was steady between 0.1 and 0.2 Å/s, as measured by a quartz crystal microbalance. We then opened the shutter and deposited 5 nm of Pc on both pristine sapphire and MoS_2 substrates. Samples were characterized by ground state absorption and Raman spectroscopy before TA measurements.

2.4.3 Ultrafast Transient Absorption Spectroscopy

Femtosecond-TA experiments were performed in a commercial system (Ultrafast Systems LLC, Helios) with a Ti:sapphire amplifier (Spectra-Physics, Solstice). The fundamental 800 nm, 2.5 mJ, 100 fs pulse is split to form the pump and probe beams. The pump beam is routed through an optical parametric amplifier (Light Conversion, TOPAS-C) to produce pump pulses at wavelengths of 510 nm and 705 nm. The probe beam is directed through a 3-mm thick sapphire window to monitor the visible spectral region. The pump and probe were then focused onto the sample, which was contained in a 2-mm glass cuvette (Starna Cells). Films were placed in cuvettes and sealed with grease, PTFE tape, and Parafilm in a nitrogen glovebox to avoid photooxidation

during the course of experiments. The instrument response function (IRF) of the TA setup was determined to be 320 fs by measuring the width of a Gaussian fit to the optical Kerr effect response of sapphire in the glass cuvette. For each sample, we measured and averaged 3 different locations to obtain representative TA data.

For measurements longer than the 3 ns temporal window, we used an Ultrafast Systems LLC, EOS spectrometer, which we have described elsewhere.[96] To obtain an adequate signal-to-noise ratio, we used a pump excitation power ten times greater than was used for femtosecond-TA measurements.

2.4.4 Pump Power-Dependent Measurements

Figure 2.14 shows pump power-dependent TA measurements for both isolated components in the heterojunction: 5-nm CuPc and monolayer MoS_2. We calculated the exciton density per volume using equation 2.1 to ensure that we are

$$N = \frac{\left(1-10^{2-Abs}\right)*I_{\phi}}{t} \qquad (2.1)$$

generating similar numbers of excitons in different samples, particularly in light of the change in absorption of Pc between sapphire and MoS_2 substrates. In equation 2.1, N is the exciton density per unit volume, Abs is the absorbance at the pump wavelength, I_{ϕ} is the photon flux, and t is the film thickness. For TA measurements across different samples, we chose a pump wavelength that would generate an exciton density of 3 x 10^{18} cm^{-3} when exciting MoS_2 and 7 x 10^{18} cm^{-3} when exciting Pc to maximize signal while minimizing biexcitonic effects.

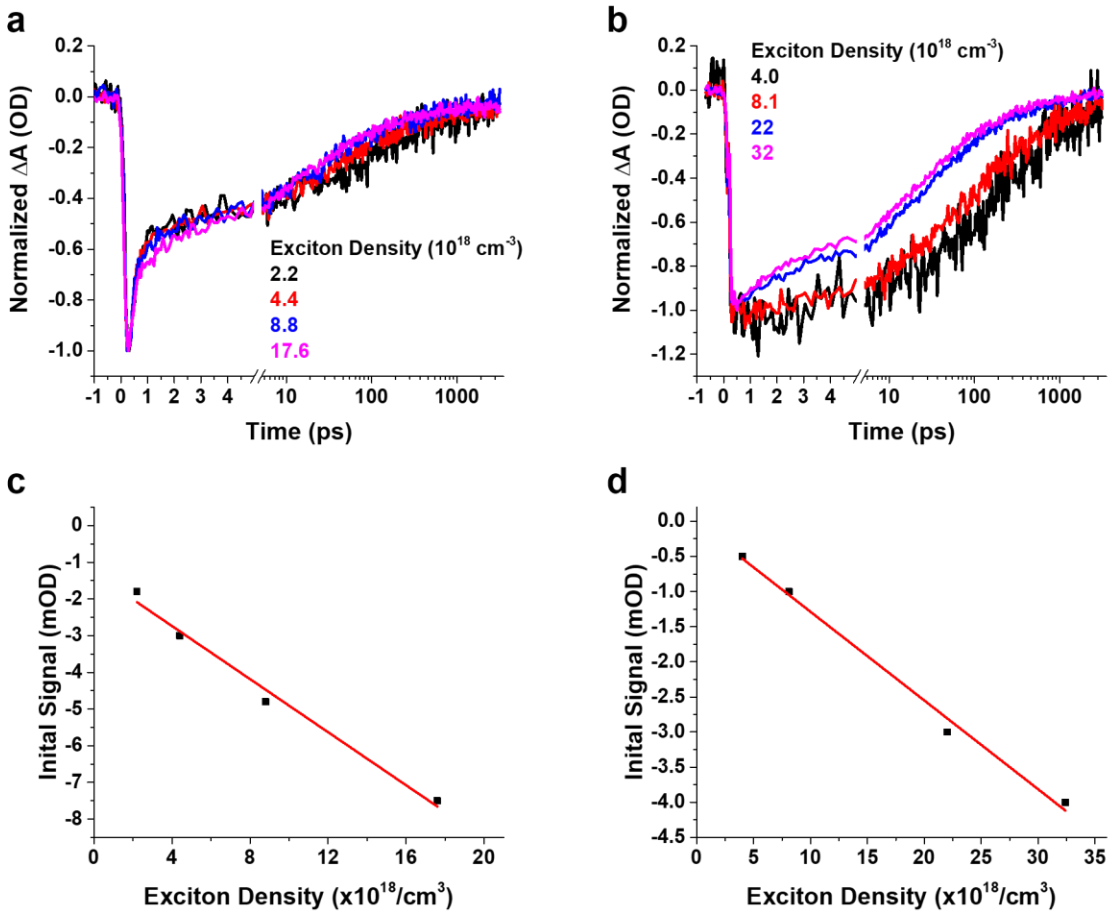

Figure 2.14. Pump power-dependent measurements on **(a)** MoS_2 with 510 nm excitation and **(b)** CuPc with 705 nm excitation. Initial signal plotted as a function of exciton density for **(c)** MoS_2 and **(d)** CuPc. The solid red lines in (c) and (d) are linear fits with an R^2 of 0.98 and 0.97, respectively.

2.4.5 Spectroelectrochemistry of CuPc$^{+\bullet}$

To ensure we had enough signal for spectroelectrochemistry, we evaporated 40-nm thick CuPc films on indium tin oxide (ITO) on glass. We applied a constant potential of +1.0V versus a silver (Ag) wire while measuring the spectrum of the CuPc radical cation (**Figure 2.6**). The reference electrode was platinum (Pt), and the electrolyte was 1M potassium chloride (KCl) in H_2O, which are parameters used for Pc films in prior studies.[97] The main features in the differential spectrum

are the negative bleaches of the Q-band absorption features and a positive feature in the 450 – 550 nm region.

2.5 Chapter Conclusion

The photoinduced charge separation processes in type-II (Cu, H_2)Pc/monolayer MoS_2 mixed-dimensional heterojunctions are sub-picosecond, likely reflecting a high density of states at the accepting MoS_2. While the rates of charge separation are indistinguishable for CuPc/MoS_2 and H_2Pc/MoS_2 MDHJs, 35% of the population of charge-separated states in CuPc/MoS_2 have a lifetime of 70 ns, a factor of 17 longer than that of H_2Pc/MoS_2 and a factor of 40 longer than that of previously reported 2D-2D heterojunctions.[71,72] Preservation of excess electrons in MoS_2 and excess holes in the CuPc/MoS_2 system appears to be enabled by the π-face-on orientation of CuPc on MoS_2, as measured by polarized Raman spectra, which templates stacking of CuPc molecules in the thin film and, in turn, facilitates the transport of holes through the stacks and away from the interface. Although previous studies have analyzed ultrafast charge transfer in organic/2D heterojunctions, our approach allows us to selectively excite and probe both the organic and 2D components and study the role of the metal center of Pc molecules on ultrafast photoinduced processes and in molecular orientation.[60,61,67–69,90] Overall, our results demonstrate that the rational design of these types of heterojunctions, similar to all-organic heterojunctions,[98–103] involves consideration of the morphology, electronic structure, and orientation of molecules on the surface of 2D materials, since such parameters can clearly dictate the lifetimes of the charge-separated states.

Chapter 3: Light-Triggered Switching of Quantum Dot Photoluminescence through Excited-State Electron Transfer to Surface-Bound Photochromic Molecules

Adapted from:

Padgaonkar, S.*; Eckdahl, C. T.*; Sowa, J. K.; López-Arteaga, R.; Westmoreland, D. E.; Woods, E. F.; Irgen-Gioro, S.; Nagasing, B.; Seideman, T.; Hersam, M. C.; Kalow, J. A.; Weiss, E. A., *Nano Letters*, **2021**, *21* (1), 854-860.

(* indicates equal contribution)

3.1 Chapter Summary

This chapter describes reversible "on-off" switching of the photoluminescence (PL) intensity of CdSe quantum dots (QDs), mediated by photochromic furylfulgide carboxylate (FFC) molecules chemisorbed to the surfaces of the QDs. Repeated cycles of UV and visible illumination switch the FFC between "closed" and "open" isomers. Reversible switching of the QDs' PL intensity by >80% is enabled by different rates and yields of PL-quenching photoinduced electron transfer (PET) from the QDs to the respective isomers. This difference is consistent with cyclic voltammetry measurements and density functional calculations of the isomers' frontier orbital energies. This work demonstrates fatigue-resistant modulation of the PL of a QD-molecule complex through remote control of PET. Such control potentially enables applications, such as all-optical memory, sensing, and imaging, that benefit from a fast, tunable, and reversible response to light stimuli.

3.2 Introduction

Precise and dynamic control of the function of materials in applications like catalysis, memory, and electronics is achievable by making the materials responsive to environmental stimuli in prescribed ways.[104,105] Light is a particularly powerful remote trigger for responsive materials because it may be delivered by a remote source with precise control of time, location, energy, phase and intensity.[106] Nanomaterials are promising candidates for photo-control schemes because they often have intense and well-defined optical spectra, in addition to high surface-area-to-volume ratios that facilitate strong interactions with photoresponsive molecules. In particular, the photo-responsivity of nanomaterials can be enhanced through surface functionalization with photochromic molecules (or photoswitches), which reversibly isomerize upon excitation with

different wavelengths of light.[106–108] This strategy has enabled control over photocatalytic activity in gold nanoparticles,[109] resistivity in two-dimensional semiconducting field-effect transistors,[110] magnetism in organometallic thin films,[111] and porosity of metal-organic frameworks.[112]

Composites of colloidal semiconductor quantum dots (QDs) and molecular photoswitches have previously been used to control photocurrent in QD-film-based two-terminal devices[113] and photoluminescence (PL) intensity of QDs.[114–124] QDs are known for their high PL quantum yields, but the ability to control their PL with a remote field makes them even better candidates for sensing, imaging, and optical memory applications. In all of the aforementioned studies in which the PL of the QDs was switched "on" and "off" by photoisomerization, the operative PL quenching pathway was Förster resonant energy transfer (FRET) to the photochromic molecule. While this mechanism has been useful for imaging applications, FRET is inherently destructive to the magnitude of the PL response because the absorbance energies of the acceptor (photoswitch) overlap with the emission energies of the donor (QD).[114–122] With this overlap, energy transferred from the QD to the photoswitch also incidentally leads to its isomerization, thus changing the PL intensity during readout.

A non-destructive mechanism for remote-control of the intensity of QDs' PL is photoinduced electron transfer (PET) between the QD and an adsorbed photoswitch molecule. In such a system, the photoisomerization of the photoswitch shifts its frontier orbital energies above and below the band-edges of the QD and thereby switches PET between thermodynamically uphill and downhill regimes (**Figure 3.1**). For use of QD-photoswitch systems in fast-response applications in

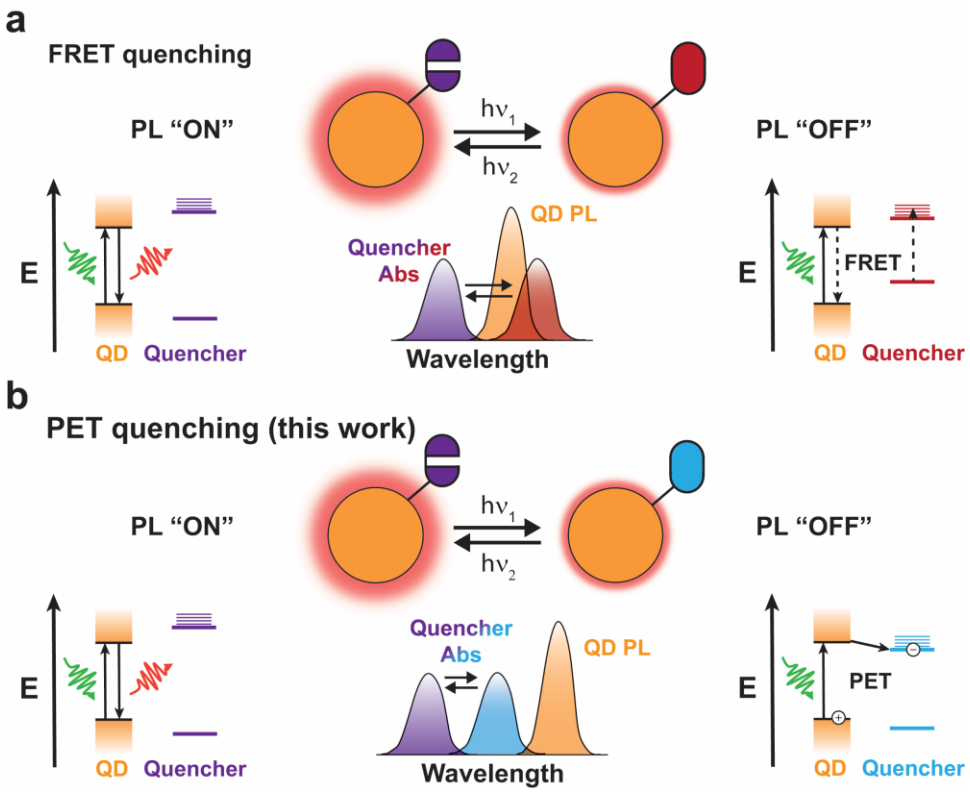

Figure 3.1. Difference between the FRET mechanism used in prior works and the PET mechanism used here to reversibly quench the QD's PL with bound photochromes. **(a)** FRET quenching requires spectral overlap of the emission of the QD with the absorbance of one of the isomers. This process excites the photochrome upon readout, leading to isomerization that degrades the response of the system. **(b)** The PET quenching mechanism requires proper energetic alignment of frontier orbitals but not spectral overlap, so it is non-destructive.

electronics and optical memory,[125–128] the photoswitching mechanism should also rely on electrocyclization-type isomerization, which occurs on ultrafast (picosecond) timescales.[129–136]

Here, we report reversible light-triggered PET modulation of the PL intensity of colloidal CdSe QDs using chemisorbed photoswitch molecules. We achieve reversible, >80% quenching of the PL of the solution-phase ensemble by activating (and then deactivating) the PET pathway to a surface-bound photoswitch, furylfulgide carboxylate (**FFC**). The "closed" conjugated form of FFC (**C-FFC**) has a lower reduction potential than the "open" form, such that isomerization to **C-FFC** using UV-light turns "off" the PL of the QDs. Reformation of the open state of FFC with green

light turns "on" the PL of the QDs. We chose fulgides as the photoswitches because they reversibly photo-isomerize on the picosecond timescale with minimal fatigue.[129–136] In addition, we incorporated a carboxylate group on the fulgide skeleton of the **FFC** to enhance the probability of PET since it chemisorbs to the surface of the QD.[137–140] The diameter of the CdSe QDs was tuned to 4.0 nm to eliminate the possibility of energy transfer to the FFC and to enable selective photoexcitation of the QD without photoexciting the FFC.

3.3 Results and Discussion

3.3.1 Synthesis and Characterization of FFC

We synthesized **FFC** by first using a previously reported phosphine-mediated cascade reaction to access tetra-substituted furan **1** in a single step from commercially available *tert*-butyl acrylate.[141] **FFC** was then prepared through consecutive Stobbe condensations starting from diethyl succinate, followed by saponification with sodium hydroxide and dehydration with acetyl chloride, **Figure 3.2a**.[142] This synthesis produces **FFC** as the *Z* open isomer.

Figure 3.2b shows the three isomers of **FFC**, and **Figure 3.2c** shows their absorbance spectra. Upon UV illumination (λ_{peak} = 365 nm), ***Z*-FFC** (open) undergoes *cis-trans* isomerization to ***E*-FFC** (open), followed by electrocyclization to closed isomer **C-FFC**. Ultrafast transient absorption (TA) measurements show that the ring-closing occurs on a timescale faster than 400 fs and the ring-opening occurs on a timescale of 1-2 ps, similar to prior studies on similar structures.[129–135] The quantum yield of electrocyclization with respect to absorbed photons is 20 ± 3%. Green-light illumination (λ_{peak} = 532 nm) induces a retro-electrocyclization, with a quantum yield of 14.4 ± 0.8%, to regenerate the open form, in which the photostationary state (PSS), or equilibrated state of isomers, consists of 75 ± 5% open *E* and 25 ± 5% open *Z* (no closed isomer). These quantum

yields are similar to those reported for structurally similar furyl fulgides.[143] The PSS of **FFC** in toluene under 365-nm illumination, which are the solvent and wavelength we use in all experiments with QDs below, comprises 52% C, 26% *E* (open), and 22% *Z* (open) isomer (all ± 5%). Below, for simplicity, we will refer to the state of **FFC** after UV illumination as "closed", even though ~50% is still in the open form. Similarly, we will refer to the mixture of the *E* and *Z* isomers obtained after green illumination as "open", because the two open isomers have nearly identical electronic and optical properties.

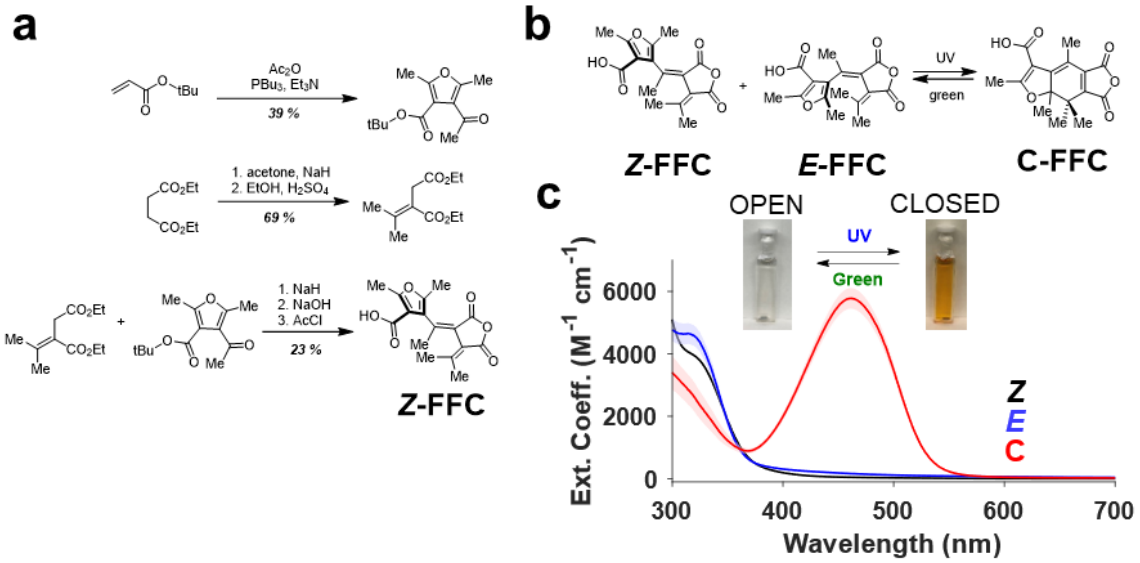

Figure 3.2. (a) Synthetic scheme to obtain ***Z*-FFC**. **(b)** Molecular structure and photographs of solutions of open (*Z*, *E*) and closed (C) isomers of **FFC**. **(c)** Absorbance spectra of all isomers of **FFC** in toluene.

3.3.2 Quantification of Bound FFC Ligands to QD Surface

We synthesized CdSe QDs using a previously reported hot-injection procedure.[144] The QDs have a first excitonic absorbance peak at 585 nm, which corresponds to a diameter of 4.0 nm, and estimated conduction and valence band-edge energies as shown in **Figure 3.3a**.[145–147] To substitute ***Z*-FFC** for the native oleate (OA) ligands on the QDs, we added ***Z*-FFC** to the QDs in toluene at

room temperature and stirred the mixture overnight for 16 hours. We confirmed that the ***Z*-FFC** is bound to the QD surface by monitoring the displacement of the OA ligands from the QD surface with ^{1}H NMR (**Figure 3.3**). Based on NMR spectra with the internal HMCTS standard, there are 83 native oleate (OA) ligands per QD at a surface coverage of 1.7 ligand/nm^2 for this 4.0-nm size of QDs. The broadened OA peak at 5.7 ppm in d_8-toluene can be used as a proxy to determine the amount of ligands that are bound to the QD surface. Upon the addition of ligands with the carboxylate group that bind to the QD surface, we observe the appearance of a sharper peak at 5.45 ppm that corresponds to free OA ligand. In both the control carboxylate furan (CF) and **FFC** cases, we observe an increase in the amount of OA displaced as a function of equivalents of molecule

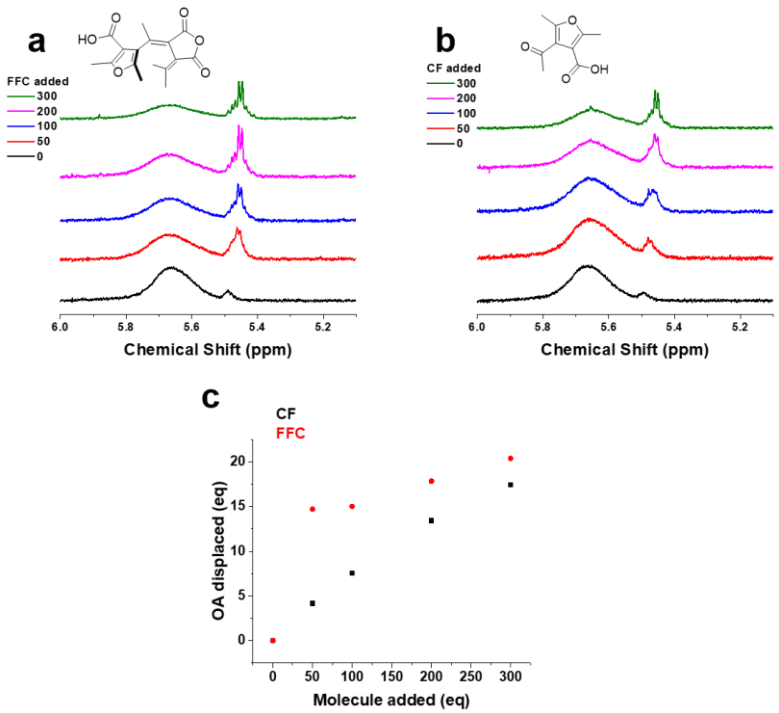

Figure 3.3. ^{1}H NMR spectra of the OA region of QDs with **(a) FFC** and **(b)** CF added. **(c)** Amount of OA displaced as a function of equivalents of molecule added. The amount was determined by taking the relative ratios of the integrated areas under Lorentizan fits to the free and bound OA population.

added, **Figure 3.3c**. We note that the **FFC** seems to saturate more quickly, likely because it displaces more OA ligands because of its bulkier size than CF.

This chemisorption is further supported by changes in the NMR signals corresponding to the ***Z*-FFC** methyl group at 2.57 ppm in $CDCl_3$, which shift and broaden when an increasing fraction of the total added ***Z*-FFC** adsorbs to the surface of the QD (**Figure 3.4**). This behavior, typical of carboxylates on CdSe QDs, suggests that the ***Z*-FFC** is in a regime of intermediate exchange between bound and free states on a time scale commensurate with the NMR measurement, but the broadening prevents accurate integration of the signals or partitioning between "bound" and "free" populations.[137–140] As a result, we estimate the number of bound **FFC** ligands from the number of displaced OA ligands, which we measure to be 17 upon addition of 200 eq. of **FFC**, **Figure 3.3**.

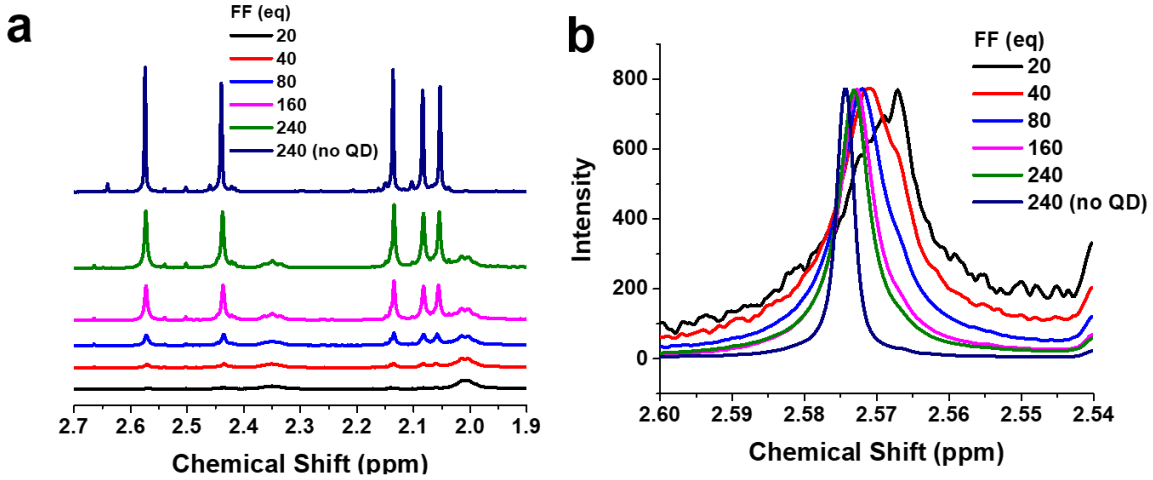

Figure 3.4. (a) ^{1}H NMR spectra of the methyl region of **FFC** with different amounts of **FFC** added to QD mixture with peaks normalized to the HMCTS internal standard at 0.18 ppm (not shown). **(b)** Spectral broadening of **FFC** when in the presence of QD with peaks normalized to each other. These NMRs are in $CDCl_3$.

3.3.3 Switchable PET from QD to FFC Isomers

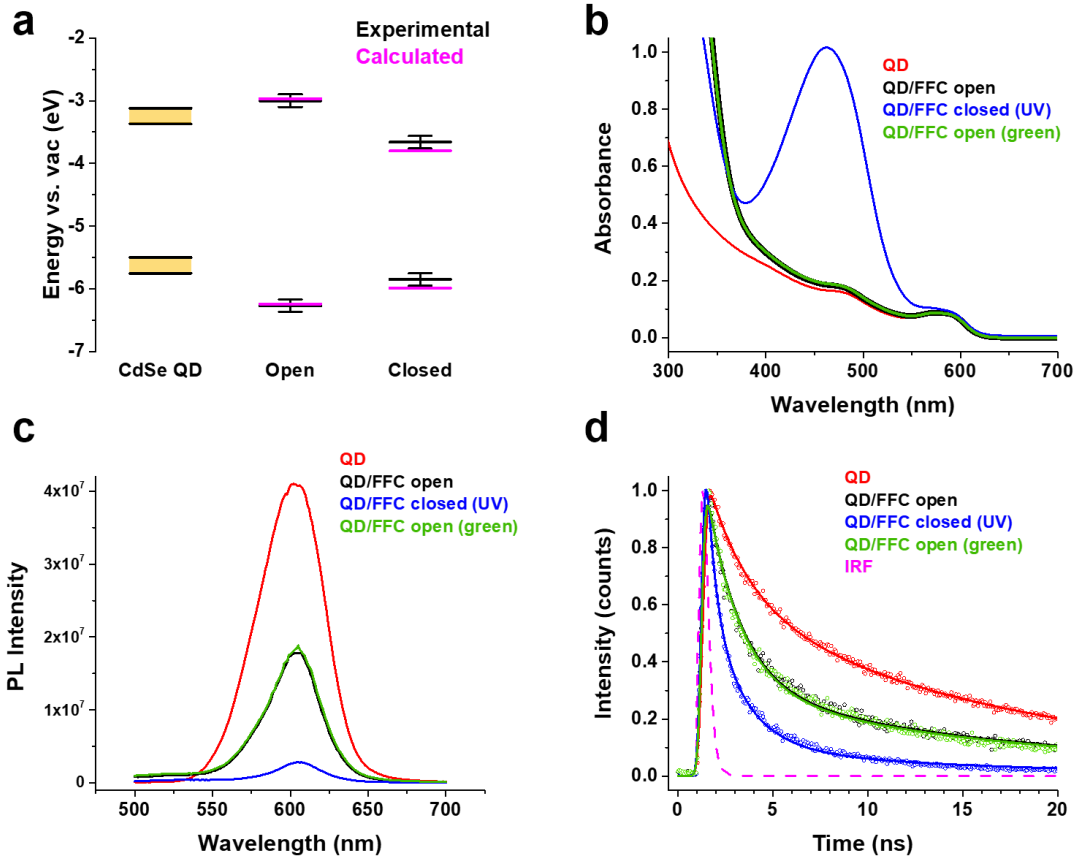

Figure 3.5. (a) Experimental (black) and calculated (pink) energy levels of open and closed isomers of **FFC** and CdSe QDs. The energies of the HOMOs of the **FFC** are obtained from cyclic voltammograms and DFT calculations, and the energies of the LUMOs are estimated by adding the measured optical bandgaps to the HOMO energies. Energy levels of the QD are estimated from literature calibration curves, and the width of the bands are obtained from the FWHM of the first absorption peak. **(b)** Absorbance and **(c)** PL spectra of 2 µM CdSe QDs alone (red) and with 600 eq. of **FFC** (black) in air-free toluene following irradiation with UV (365 nm, blue trace) and then green (532 nm, green trace) light. **(d)** The first 20 ns of exciton decay traces monitored by time-resolved PL of the same QD (red) and QD/**FFC** (black) mixtures following irradiation with UV (365 nm, blue trace) and then green (532 nm, green trace) light. Black and green traces overlay in **(b), (c),** and **(d)**. Multiexponential fits (solid lines) are convolved with the instrument response function (IRF, dashed pink) of 0.40 ns. Steady state PL spectra were acquired with an excitation wavelength of 450 nm. Time-resolved PL traces were acquired with a 450 nm pulsed diode and a 475 nm long-pass filter.

Figure 3.5a shows the frontier orbital energies of the open and closed isomers of **FFC**. We estimated the HOMO energy of unbound **FFC** from measurements of its oxidation potential using cyclic voltammetry in acetonitrile, and approximated its LUMO energy by adding the optical bandgap to the HOMO energy. To assess the effect of QD binding on **FFC** orbital energies, we also calculated HOMO energies within $Cd_{56}Se_{50}(OAc)_{11}$(**FFC**$^-$) clusters in toluene (NWChem, B3LYP/6-311G**) and added the measured optical gap to determine the LUMO energy, as above.[148,149] According to both the experimentally and computationally derived **FFC** orbital energies, PL-quenching PET from the QD to **FFC** is ~0.66 eV more favorable for the closed isomer than for the open isomers. The increased driving force should correspond to an increased rate and yield of PET upon UV illumination, which is then reversible upon illumination with green light.[150]

Figures 3.5b and **3.5c** show the changes in the absorbance and PL spectra of a solution of 2 μM QDs with 600 eq. of added open **FFC** (black), and of the QD-open **FFC** mixture upon irradiation with a UV lamp (λ_{peak} = 365 nm) for 50 minutes (blue), followed by illumination with green LEDs (λ_{peak} = 532 nm) for 6 minutes (green). **Figure 3.5b** confirms that the expected changes in absorbance of **FFC** upon isomerization still occur in the presence of QDs. **Figure 3.5c** shows that the PL of the QDs is quenched by 68% upon addition of the open **FFC**, and that the quenching magnitude increases to 96% after UV illumination and conversion to the closed state. Upon green irradiation to revert the molecule back to the open state, the PL is completely reversed to the intensity obtained upon adding open **FFC** initially. These spectra remain unchanged after the same time, energy, and intensity of illumination if no **FFC** is added, as expected since air and water were excluded from these samples (**Figure 3.6**).[151,152] The decrease in PL from the QDs upon addition and photoswitching of **FFC** cannot be due to FRET to **FFC**, because the emission

band of the QDs, centered at 603 nm, has no spectral overlap with the absorbance of any **FFC** isomer (**Figure 3.2c**). We can therefore conclude that the origin of the additional nonradiative decay pathway introduced by **FFC** is PET from the QD to the **FFC**.

Fits of kinetic traces acquired by time-resolved PL (TRPL) measurements (**Figure 3.5d**) show

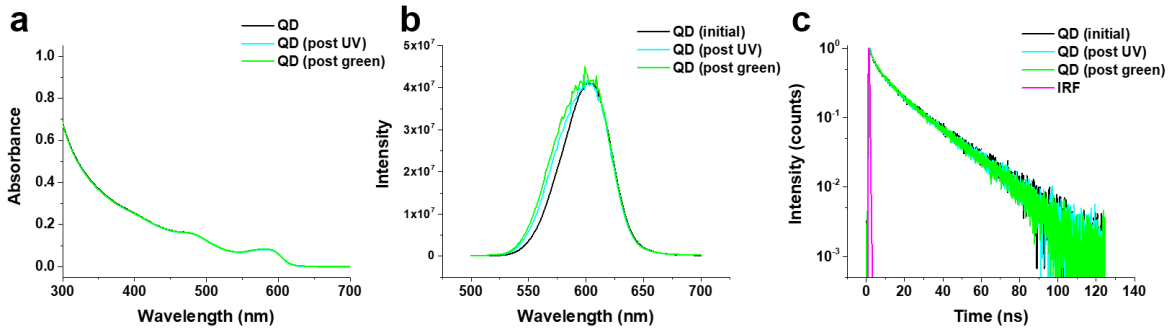

Figure 3.6. Change in QD **(a)** absorbance, **(b)** PL, and **(c)** TRPL after 50 minutes of UV illumination and 6 minutes of green illumination. These data correspond to the data shown in Figure 3.2.

that the addition of open FFC introduces a new non-radiative pathway, which we assign to PET, with a time constant of 1.78 ± 0.01 ns with a normalized amplitude of 71%, which is consistent with the observed steady-state PL quenching of 68% (see **Table 3.1** for the fitting parameters). The TRPL kinetics obtained from samples of the QD-**FFC** after UV irradiation have this same decay time constant (1.78 ns) with an amplitude of 43%, plus additional decay process with a time constant of 0.45 ± 0.01 ns and an amplitude of 50%. The sum (93%) of the amplitudes of these two PET processes matches the total percentage of the steady-state PL intensity that is quenched following UV irradiation of the QD-FFC sample (96%). Furthermore, the normalized amplitudes of these two processes (43% and 50%), consistent with the ~1:1 ratio of closed and open isomer in the PSS of this sample. Ultrafast transient absorption measurements detailed in **Figure 3.7** and **Table 3.2** demonstrate that **FFC** does not introduce any new non-radiative pathways, including

PET, on a timescale faster than those measured in the TRPL measurements shown in **Figure 3.5d**. We do not see accumulation of radical anion species of **FFC** in steady-state absorption measurements, which implies high-yield non-radiative charge recombination of the photoinduced radical pair: QD^{+}-$\mathbf{FFC}^{-}$ → QD-**FFC**.

Table 3.1. Time Constants (τ_n) and Amplitudes (A_n) Extracted from Fits to the Kinetic Traces of the Exciton Decay of QD and QD/FFC Mixtures, **Figure 3.5d**.[a,b]

Sample	τ_1 (A_1)	τ_2 (A_2)	τ_3 (A_3)	τ_4 (A_4)	τ_5 (A_5)
	eT to **C-FFC**	eT to ***E*-FFC**/***Z*-FFC**	Trapping	Charge recombination	Charge recombination
QD	-	-	2.05 ± 0.02 ns (40 ± 0%)[c]	12.21 ± 0.11 ns (47 ± 0%)[c]	42.41 ± 0.59 ns (13 ± 0%)[c]
QD (post UV)	-	-	2.05 ± 0.02 ns (40 ± 0%)[c]	12.21 ± 0.11 ns (49 ± 0%)[c]	42.41 ± 0.59 ns (12 ± 0%)[c]
QD (post green)	-	-	2.05 ± 0.02 ns (36 ± 0%)[c]	12.21 ± 0.11 ns (51 ± 0%)[c]	42.41 ± 0.59 ns (12 ± 0%)[c]
QD/**FFC** (open)	-	1.78 ± 0.01 ns (71 ± 0%)[d]	-	12.21 ns (22 ± 0%)[e]	42.41 ns (7 ± 0%)[e]
QD/**FFC** (closed, post UV)	0.45 ± 0.01 ns (50 ± 1%)	1.78 ± 0.01 ns (43 ± 1%)[d]	-	12.21 ns (7 ± 0%)[e]	42.41 ns (<1 ± 0%)[e]
QD/**FFC** (open, post green)	-	1.78 ± 0.01 ns (71 ± 0%)[d]	-	12.21 ns (21 ± 0%)[e]	42.41 ns (8 ± 0%)[e]

[a]$\Sigma A_n = 1$. [b]An error of 0% indicates the error is less than 0.5%. [c]The TRPL traces of QDs without FFC were fitted globally to find the radiative processes intrinsic to the QD. [d]This component was globally fit across the QD/FFC traces. [e]This component was fixed from the intrinsic processes of the QD.

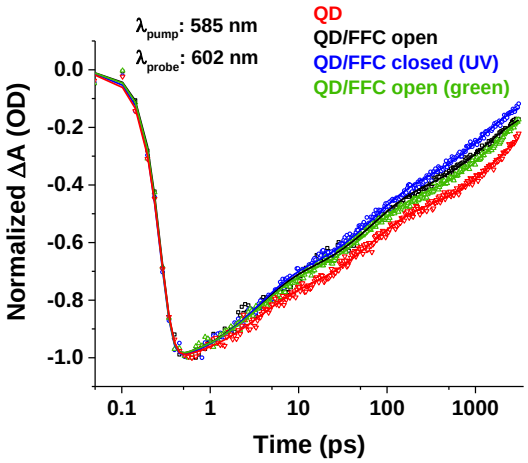

Figure 3.7. Kinetic traces at a probe wavelength of 602 nm (the band edge of QDs) extracted from TA measurements with 585 nm pump.

Table 3.2. Time Constants (τ_n) and Amplitudes (A_n) Extracted from Fits to the Kinetic Traces in **Figure 3.7**.[a,b]

Sample	τ_1 (A_1)	τ_2 (A_2)	τ_3 (A_3)	τ_4 (A_4)
	Trapping[c]	Trapping[c]	Radiative trapping[d]/electron transfer[e]	Radiative recombination
QD	3.2 ± 0.2 ps (21 ± 0%)	62.9 ± 2.4 ps (28 ± 0%)	2100 ± 200 ps (36 ± 2%)	>3 ns (15 ± 2%)
QD/**FFC** (open)	3.2 ps (26 ± 0%)[f]	62.9 ps (28 ± 0%)[f]	1400 ± 100 ps (31 ± 1%)	12.21 ns (22 ± 0%)[e]
QD/**FFC** (closed)	3.2 ps (28 ± 0%)[f]	62.9 ps (29 ± 0%)[f]	1200 ± 100 ps (33 ± 1%)[g]	12.21 ns (7 ± 0%)[e]
QD/**FFC** (open)	3.2 ps (25 ± 0%)[f]	62.9 ps (28 ± 0%)[f]	1800 ± 100 ps (35 ± 1%)	12.21 ns (21 ± 0%)[e]

[a]$\Sigma A_n = 1$. [b]An error of 0% indicates the error is less than 0.5%. [c]These processes are likely due to surface traps for electrons and holes in CdSe QDs and regularly appear at these timescales in the literature. [d]This component is radiative trapping for the QD only trace. [e]This component corresponds to electron transfer for the QD/FFC traces. [f]This component was fixed from the intrinsic processes of the QD. [g]This component is likely a combination of the 450 ps and 1.8 ns electron transfer components from TRPL measurements but splitting this across two time constants led to a high codependency for the fit.

3.3.4 Fully Reversible PL Quenching in QD/FFC Moeity

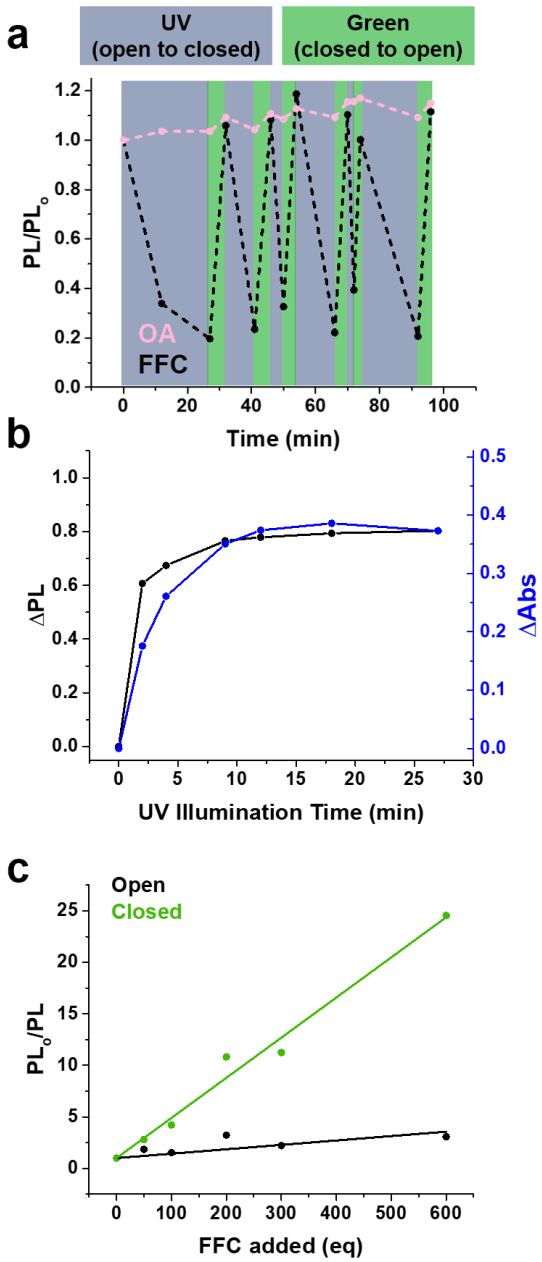

Figure 3.8. (a) Change of QD PL intensity with repeated illumination cycles with 300 eq. of **FFC** and OA. **(b)** Dependence of the change in normalized PL intensity and absorbance (at 463 nm) on UV illumination time in a QD mixture with 300 eq. of FFC. **(c)** PL/PL_o plotted against the amount of **FFC** added, illustrating the enhancement of PL quenching when comparing open and closed **FFC.** Linear fits are guides to the eye. PL spectra were acquired with an excitation wavelength of 450 nm.

For any application that would benefit from light-based control of PL, it is important to demonstrate that the modulation we observe here is reversible and fatigue-resistant. **Figure 3.8a** shows that the photoswitchable PET to **FFC** isomers enables >80%, fully reversible quenching of QDs' PL over repeated UV/green irradiation cycles when the QDs are treated with 300 eq. of **FFC**. We note that this reversibility is dependent on the exclusion of air and water. This on:off ratio is greater than that observed in prior work using FRET as the PL quenching mechanism.[114–122] We know that the **FFC** molecule is not degrading over the course of this experiment because the absorbance of its respective isomers are fully recovered at each cycle (**Figure 3.9**).

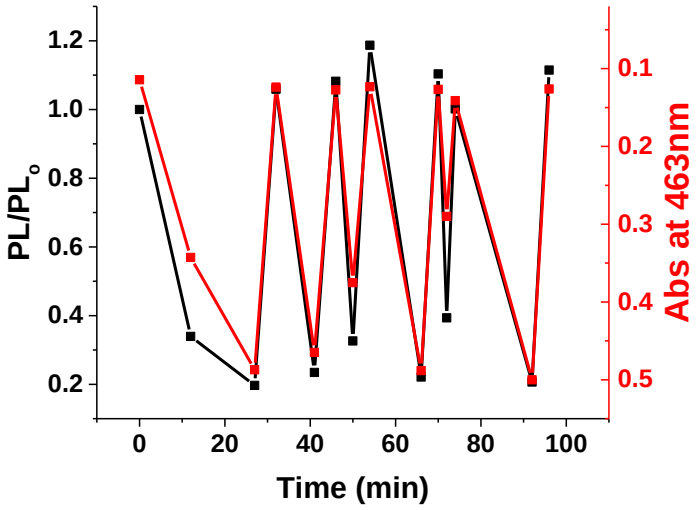

Figure 3.9. The change in QD PL quenching corresponds to the change in absorbance at 463 nm. No degradation is seen in the **FFC**. The illumination cycles are the same as in **Figure 3.8a**.

When adding the same number of oleate ligands to the QDs, we do not observe more than a ±10% change in the PL intensity. This change can be attributed to previously characterized photo-brightening and photo-darkening processes of CdSe QDs.[151] After treating the QDs with similar concentrations of a carboxylate-functionalized *non*-photochromic furan, we again did not observe changes in the QD PL of more than ±10% during UV/green illumination cycles, Figure 3.10. This

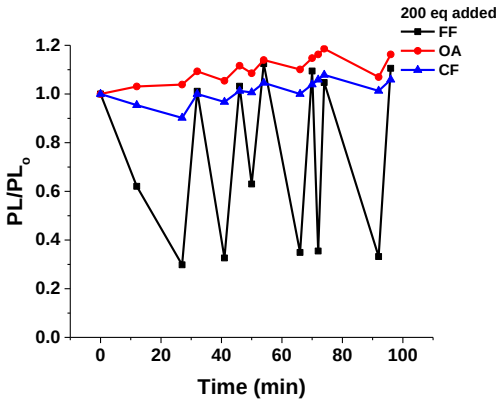

Figure 3.10. Change in PL over repeated switching cycles (with the same illumination times as seen in **Figure 3.8a**) with 200 eq of **FFC** (black), OA (red), and CF (blue) added.

non-photochromic furan binds to the QDs at similar levels as the **FFC** (**Figure 3.3**). We can therefore confirm that ligand exchange-induced surface defects are not the primary source of the reversible response we see in the QD-**FFC** case.[151] We also treated the QDs with a photochromic furylfulgide (**FFM**) with frontier orbital energies nearly degenerate with those of **FFC**, but functionalized with a methyl ester rather than carboxylate group. As expected, we did observe some reversible switching of the QDs' PL in the QD-**FFM** mixture (because QDs can still exchange electrons with molecules in diffusion-mediated electron transfer), but not nearly to the extent seen in the QD-**FFC** mixtures (**Figure 3.11**). These control experiments demonstrate that the observed PL modulation can only be achieved effectively with molecules that *both* bind and switch.

Tuning of the illumination time and/or number of equivalents of **FFC** enables additional control over the PL response. **Figure 3.8b** shows that the magnitude of the PL response is correlated with the amount of **C-FFC** in the sample, and both depend on UV illumination time (since UV light closes the **FFC**). This behavior is similarly seen in the reverse direction when the sample is illuminated with green light, which decreases the amount of **C-FFC** and thus increases

the magnitude of the PL (**Figure 3.12**). **Figure 3.8c** also demonstrates that addition of more FFC to the sample increases the degree of PL quenching for a given UV illumination time of 27 minutes.

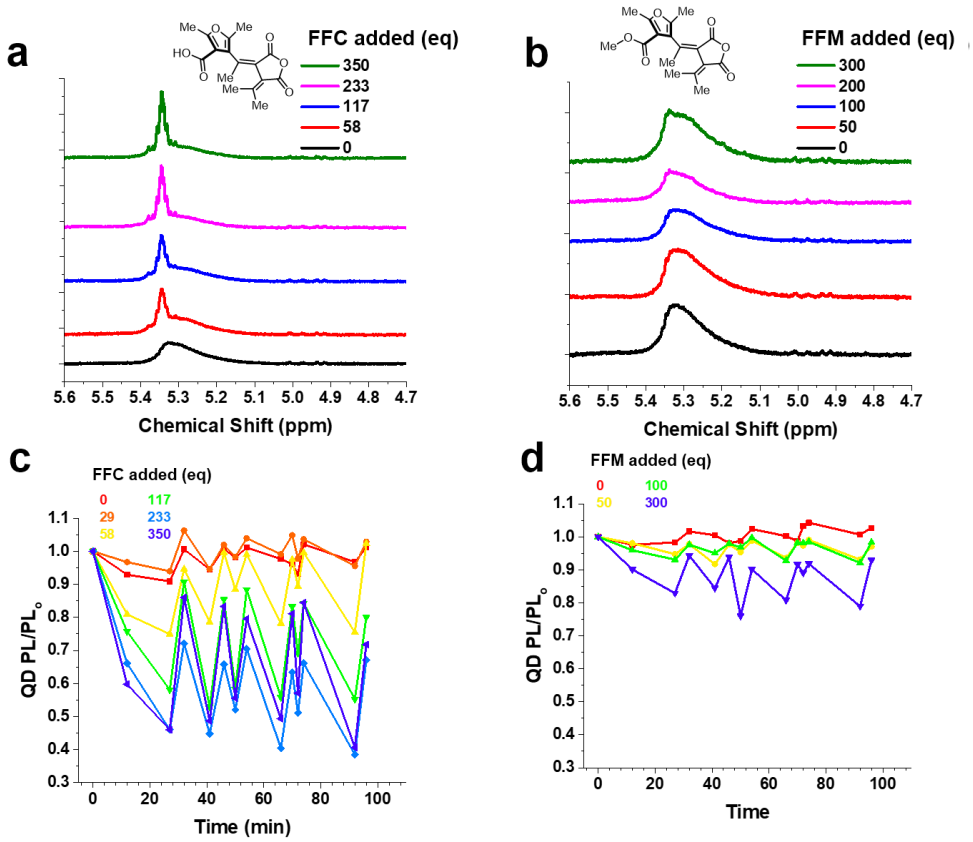

Figure 3.11. ^{1}H NMR spectra of the oleate (OA) region in the presence of a series of equivalents of **(a) FFC** and **(b) FFM**. QD PL intensity change as a function of irradiation cycles in the presence of a series of equivalents of **(c) FFC** and **(d) FFM.**

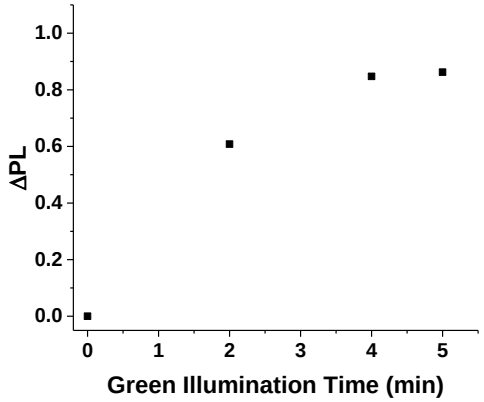

Figure 3.12. Dependence of the change in normalized PL intensity of the QD-FFC system (QDs with 300 eq. of FFC) on the time of illumination with green (532-nm) light.

3.4 Experimental Methods

3.4.1 Synthesis of Molecules

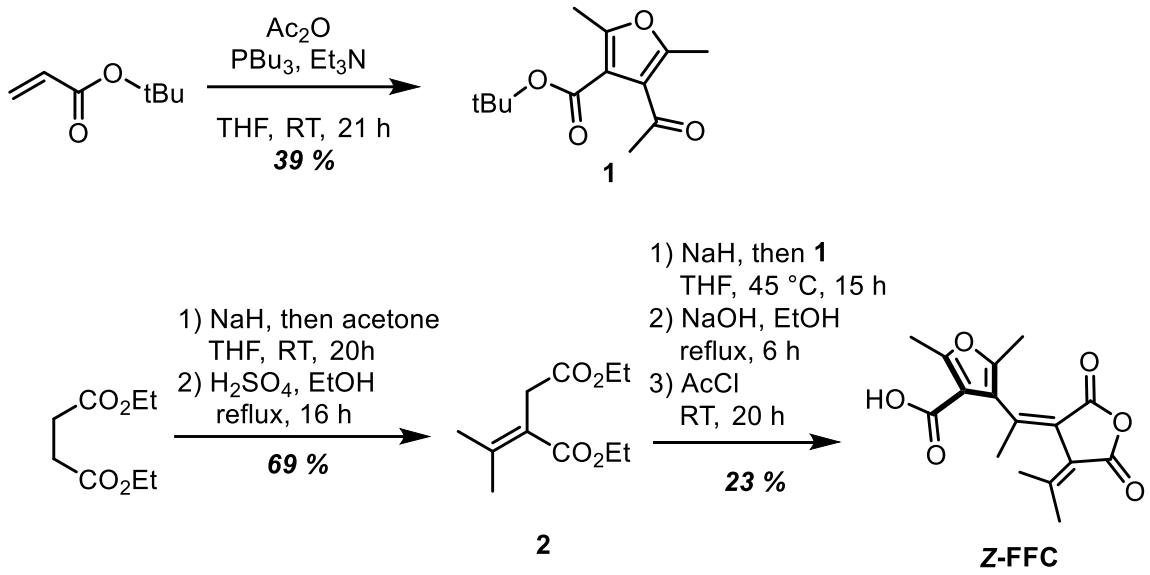

Scheme 3.1. Synthesis of furylfulgide carboxylate (**FFC**).

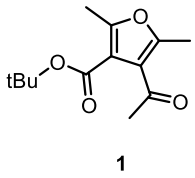

tert-butyl 4-acetyl-2,5-dimethylfuran-3-carboxylate (1). Based on a literature procedure,[141] *tert*-butyl acrylate (5.13 g, 5.86 mL, 40.0 mmol) and acetic anhydride (14.7 g, 13.6 mL, 144 mmol) were added to 150 mL of THF in a 500 mL round-bottom flask equipped with a magnetic stir bar. Tributylphosphine (9.71 g, 12.0- mL, 48.0 mmL) was added to the solution with stirring, followed by the addition of triethylamine (21.9 g, 30.1 mL, 216 mmol). The reaction was stirred at room temperature for 21 hours. The initially clear reaction nearly immediately takes on a yellow color upon addition of the triethylamine. Upon consumption of the starting acrylate (monitored using TLC with a 9:1 ethyl acetate/hexane mobile phase and $KMnO_4$ staining), the solution was diluted with 300 mL of water, then extracted with 3x100 mL of dichloromethane. The combined organic

layers were washed with 2x100 mL of brine then dried over Na_2SO_4. Removal of the solvent *in vacuo* provided a yellow oil which was subjected to column chromatography (Silica gel, 8-15% step gradient of ethyl acetate/hexanes) to yield the title compound as a colorless oil (927 mg, 39%). Spectral data were consistent with the literature report.[141]

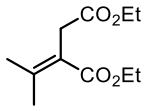

2

diethyl 2-(propan-2-ylidene)succinate (2). Based on a literature procedure,[142] NaH (60 wt% dispersion in mineral oil, 2.37 g of oil/NaH dispersion, 59.2 mmol of NaH) was added to a 250 mL round-bottom flask equipped with a magnetic stir bar. 100 mL of THF were added, and the white slurry was cooled to 0 °C in an ice bath with stirring. Diethyl succinate (6.88 g, 6.57 mL, 39.5 mmol) was added and the reaction was stirred for 5 minutes. Then, 1 drop of ethanol was added, followed by the dropwise addition of acetone (2.87 g, 3.66 mL, 49.4 mmol) over 15 minutes. The reaction was stirred and allowed to warm slowly to room temperature as the ice bath melted. After 16 hours, the reaction had taken on a light vanilla color and the diethyl succinate had been consumed (monitored with TLC with 95:5 ethyl acetate/hexanes mobile phase and I_2 staining). The reaction was cooled to 0 °C in an ice bath then quenched with 50 mL of 4 M HCl. The mixture was extracted with 200 mL, then 2x50 mL ethyl acetate. The combined organic layers were washed with 100 mL 1 M HCl then dried over Na_2SO_4. Removal of the solvent *in vacuo* provided a dark yellow oil. This crude oil was dissolved in 40 mL of ethanol in a 100 mL round bottom flask equipped with a magnetic stir bar. The resultant yellow solution was cooled to 0 °C in an ice bath with stirring. 1.5 mL of sulfuric acid were added, causing immediate clouding. The

reaction was stirred at 0 °C for 1 hour. Then a reflux adapter was fitted on the flask, and the reaction was heated to reflux and stirred for 16 hours. The resultant yellow solution was cooled to 0 °C in an ice bath then quenched with 150 mL of saturated $NaHCO_3$ (aq.). The mixture was extracted with 2x100 mL of ethyl acetate. The combined organic layers were washed with 100 mL of brine then dried over Na_2SO_4. Removal of the solvent *in vacuo* provided a brown oil. Kugelohr vacuum distillation at 130 °C afforded a colorless oil composed of 90% pure product. Further purification by column chromatography (silica gel, 1:4 ethyl acetate/hexanes) provided >95% pure product (5.84 g, 69%). Spectral data were consistent with the literature report.[142]

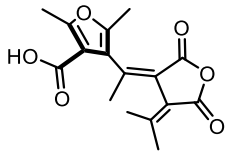

***Z*-FFC**

(*Z*)-4-(1-(2,5-dioxo-4-(propan-2-ylidene)dihydrofuran-3(2H)-ylidene)ethyl)-2,5-dimethylfuran-3-carboxylic acid (*Z*-FFC). NaH (60 wt% dispersion in mineral oil, 538 mg of oil/NaH dispersion, 8.73 mmol NaH) and 25 mL of THF were added to a 100 mL round bottom flask equipped with a magnetic stir bar. The shite slurry was cooled to 0 °C in an ice bath with stirring. **2** (1.63 mL, 1.60 g, 7.47 mmol) was added followed by one drop of ethanol. The slurry took on a slight yellow color. The reaction was stirred at 0 °C for 20 minutes. Then, **1** (2.17 mL, 2.08 g, 8.73 mmol) was added dropwise over 5 minutes. The reaction was heated to 45 °C. After several hours, the reaction took on a rich orange color and darkened to brown by 15 hrs. The reaction can be tracked using TLC with a 1:1 ethyl acetate/hexanes mobile phase, where the initial high R_f (>0.6) spot of **2** dissapears with the appearance of a lower $R_f = 0.3$ spot. After 15 hours, **2** was completely consumed and the reaction was cooled to 0 °C in an ice bath and quenched with

100 mL of ice-cold water. The mixture was stirred at 0 °C for 20 minutes then acidified to pH = 2 with 1 M HCl, causing a yellow precipitate to form. The mixture was extracted with 200, then 2x75 mL ethyl acetate. The combined yellow organic layers were washed with 2x100 mL brine then dried over Na_2SO_4. Removal of the solvent *in vacuo* provided a dark orange oil. The crude oil was dissolved in 100 mL of a 5 wt% solution of NaOH in ethanol (5 g of NaOH) in a 500 mL round-bottom flask equipped with a magnetic stir bar. The reaction was heated to reflux with stirring. The initial crimson color quickly darkens to dark brown with heating. Production of the triacid intermediate was monitored with LCMS (m/z = 322). After 6 hours, the reaction had fully converted to the triacid intermediate and was cooled to room temperature. The reaction was diluted with 200 mL of water then the resultant mixture washed with 2x100 mL diethyl ether and 100 mL hexanes. The dark red aqueous layer was acidified with concentrated HCl to produce a light yellow precipitate. The mixture was extracted with 2x150 mL ethyl acetate then the combined ethyl acetate layers washed with 2x100 mL brine and dried over Na_2SO_4. The triacid intermediate is somewhat insoluble in ethyl acetate, so after removal of the Na_2SO_4 with a filter, the filter and Na_2SO_4 were rinsed with 50 mL of acetonitrile to recover residual triacid. The ethyl acetate and acetonitrile were removed *in vacuo*. The crude triacid intermediate was dissolve in 50 mL of acetyl chloride in a 100 mL round-bottom flask equipped with a stir bar (we found dehydration with acetyl chloride to be preferable to acetic anhydride, which acylates the furyl carboxylate group in addition to performing the desired dehydration). The flask was wrapped in aluminum foil to exclude light. The reaction was stirred at room temperature for 20 hours. Consumption of the triacid intermediate and production of the anhydride product were monitored with LCMS. After 20 hours, the reaction was complete and the acetyl chloride was removed *in vacuo* to provide a

dark brown oil. Column chromatography (silica gel, 0-40% linear gradient of ethyl acetate/hexanes) yielded the title compound as a light yellow solid (533 mg, 23%). **^{1}H NMR** (500 MHz, Chloroform-*d*) δ 2.58 (s, 3H), 2.44 (s, 3H), 2.14 (s, 3H), 2.09 (s, 3H), 2.06 (s, 3H). **^{13}C NMR** (126 MHz, DMSO-d_6) δ 164.33, 162.98, 161.35, 156.89, 156.20, 146.87, 144.65, 122.84, 119.67, 119.47, 113.22, 26.74, 25.90, 22.01, 13.64, 11.50. **HRMS-ESI** (m/z): -303.1037 (calc'd for $C_{16}H_{15}O_6$ $[M-H]^-$ = 303.0874).

CAUTION! (Diazomethyl)trimethylsilane should be regarded as extremely toxic and should only be handled by individuals trained in its proper and safe use. All operations must be carried out in a well-ventilated fume hood and all skin contact should be avoided.

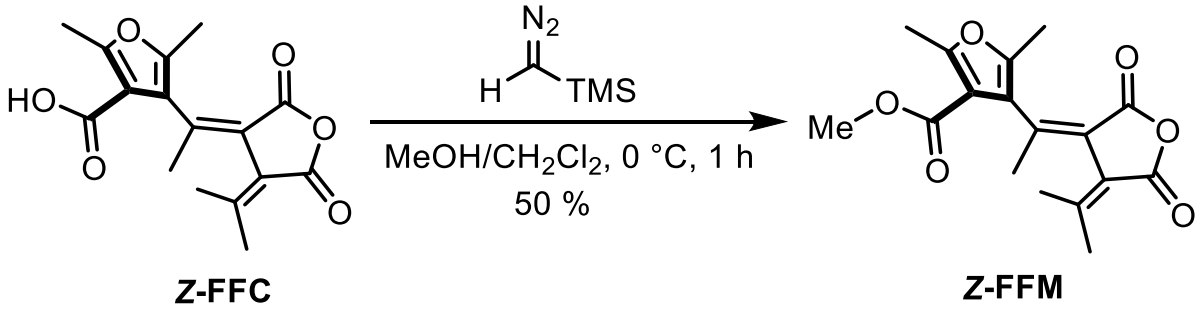

Scheme 3.2. Synthesis of the methyl ester analog, **FFM**.

Methyl (*Z*)-4-(1-(2,5-dioxo-4-(propan-2-ylidene)dihydrofuran-3(2H)-ylidene)ethyl)-2,5-dimethylfuran-3-carboxylate (*Z*-FFM). *Z*-FFC (50 mg, 0.16 mmol) was added to a 10 mL round-bottom flask equipped with a stir bar. The solid starting material was roughly dried with 3 cycles of vacuum/N_2 purging. 2.5 mL of dichloromethane (not degassed) and 0.5 mL of methanol were added to the flask to form a yellow solution which was stirred and cooled to 0 °C in an ice bath. A 2 M solution of (diazomethyl)trimethylsilane in diethyl ether (100 µL, 0.20 mmol of TMS-diazomethane) was added dropwise over one minute to the reaction flask, causing some mild

bubbling. The reaction was taken out of the ice bath and allowed to warm to room temperature with stirring over 1 hour. Then the reaction was cooled to 0 °C in an ice bath and quenched with 200 µL of acetic acid. Liquids were removed *in vacuo* to provide a yellow oil that solidifies to a glassy yellow solid upon standing in high vacuum. Column chromatography (silica gel, 13-28-50% step gradient of ethyl acetate/hexanes) yielded the title compound as a white solid (26 mg, 50%). **^{1}H NMR** (500 MHz, Chloroform-*d*) δ 3.74 (s, 3H), 2.54 (s, 3H), 2.44 (s, 3H), 2.13 (s, 3H), 2.08 (s, 3H), 2.07 (s, 3H). **^{13}C NMR** (126 MHz, $CDCl_3$) δ 164.11, 163.33, 161.65, 158.41, 154.60, 147.46, 144.63, 123.72, 121.17, 119.48, 112.83, 51.42, 27.18, 26.19, 22.55, 14.37, 12.03. **HRMS-ESI** (m/z): 319.1182 (calc'd for $C_{17}H_{19}O_6$ $[M+H]^+$ = 319.1176).

4-acetyl-2,5-dimethylfuran-3-carboxylic acid (CF). Compound **1** (1.00 g, 4.20 mmol) was

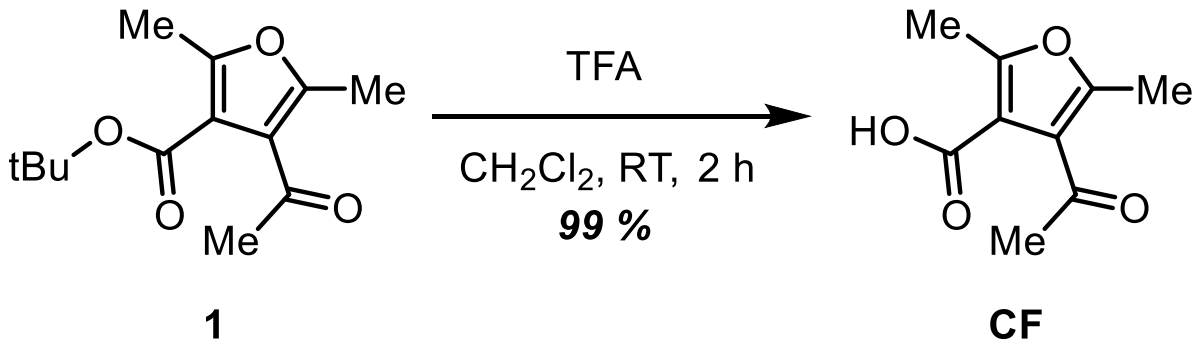

dissolved in 20 mL of a 1:1 (by volume) mixture of dichloromethane and trifuoroacetic acid. The resulting solution was stirred at room temperature under air. The solvents were removed *in vacuo*. The resulting reside was dissolved in ethyl acetate and the resulting solution was passed through a silica plug. Ethyl acetate was removed *in vacuo* to yield a white, hygroscopic solid which was dried under high vacuum and stored in a vacuum desiccator (760 mg, 99%). **^{1}H NMR** (500 MHz, DMSO) δ 2.44 (s, 3H), 2.37 (s, 3H), 2.31 (s, 3H). **^{13}C NMR** (126 MHz, DMSO) δ 196.47, 164.33,

156.08, 153.09, 122.57, 113.34, 30.69, 13.12, 12.75. **HRMS-ESI** (m/z): -181.0504 (calc'd for $C_9H_9O_4$ $[M-H]^-$ = 181.0506).

3.4.2 QD Synthesis

CdSe QDs were synthesized by using adapting previously reported synthesis.[144] Briefly, 1.6 g of Se powder (Sigma) was stirred in 10 mL 1-octadecene (Sigma). 1.28 g of CdO (Sigma) was added to a 100 mL three-necked round-bottom flask with 8.5 mL oleic acid (Sigma) and 4.5 mL ODE, and this mixture was heated to 270°C under a N_2 atmosphere. 1 mL of the Se-ODE solution was injected at 270°C and the reaction was allowed to proceed at 260°C for 10 minutes. The reaction was quenched quickly with a cooling air gun and ice bath and 10 mL of hexanes were added at 70°C. When the reaction reached room temperature, 15 more mL of hexanes were added along with 15 mL of ethanol. The solution was centrifuged at 3500 rpm for 10 minutes. After disposing the supernatant, 10 mL of hexanes were added to resuspend the pellet before adding 10 mL of ethanol and centrifuging at 3500 rpm for 10 more minutes. This centrifugation step was repeated three more times before dissolving the pellet in 10 mL of hexanes for further experiments.

3.4.3 Cyclic Voltammetry

All cyclic voltammetry experiments were conducted in a nitrogen-filled glovebox using acetonitrile with 0.1 M tetrabutylamonnium hexafluorophosphate electrolyte. Ferrocene was added as an internal standard following every run. Due to irreversibility of most of the measured redox events, potentials are reported as half-peak potentials determined by finding the potential at which the measured current reaches the average of the maximum and pre-onset currents of a peak. Because the pre-onset current was somewhat loosely determined based on peak shape, the uncertainties in the reported values were determined by varying the pre-onset current within a

reasonable range. These values were referenced to the half-wave potential of ferrocene. Redox potentials versus ferrocene were converted to the energy levels versus vacuum reported in the text based on the standard potential of the ferrocene-ferrocenium couple vs. SCE, +0.34 V, and the energy of the standard SCE potential relative to vacuum, 4.7 V.[153]

Closed isomers of fulgides were prepared *in situ* by irradiation of acetonitrile solutions with ten 350 nm Rayonet lamps for 10 minutes. Open isomers were prepared by further irradiation of the closed isomers with green LEDs from superbrightLEDs.com for fifteen minutes. The results of the CV measurements are in Table S1-1.

Table 3.3. Electrochemical Potentials for **FFC** and **FFM** Isomers, measured with CV.

	Oxidation potential vs. Fc (V)	Reduction potential vs. Fc (V)	HOMO vs. vac (eV)	LUMO vs. vac. (eV)
Open FFC	+1.23 ± 0.03	-2.3 ± 0.1	-6.27 ± 0.03	-2.7 ± 0.1
Closed FFC	+0.81 ± 0.02	-1.48 ± 0.03	-5.85 ± 0.03	-3.56 ± 0.03
Open FFM	+1.27 ± 0.02	-2.11 ± 0.02	-6.31 ± 0.02	-2.94 ± 0.02
Closed FFM	+0.74 ± 0.02	-1.50 ± 0.02	-5.78 ± 0.02	-3.54 ± 0.003

3.4.4 Transient Absorption

The setup for transient absorption (TA) measurements are described elsewhere.[154] For these experiments, the pump was tuned to 585 nm with an OPA and focused onto the sample. The probe beam was generated using an 800 nm (100 fs) pulse routed through a delay stage and a 3-mm sapphire window to monitor the visible spectral region. For TA of **FFC**, a peristaltic pump and flow cell setup was necessary to use with a reservoir that was illuminated because the pump pulse which caused the ring-opening (or ring-closing) reaction would change the isomer before it could be measured.

3.4.5 Time-resolved Photoluminescence

TRPL experiments were carried out in a custom-built microscope equipped with a piezo scanner (NanoPI, Physik Instrumente), an APD detector (MicroPhoton Devices), and a photon counting board (PicoHarp300, PicoQuant) where correlation times between the excitation pulses and detected photons were recorded. The excitation pulses were synchronized from a 450 nm, 70 ps pulsed diode laser at a repetition rate of 8 MHz (Picoquant) and focused with a long working distance objective (0.7 NA, 100x, Mitutoyo), and the detected PL was filtered with a 475 nm long-pass dichroic (Chroma) and a 495 nm long-pass filter (Thorlabs). The IRF of the instrument was measured by reflecting an attenuated excitation pulse with a silver mirror placed in the sample plane.

3.4.6 Ligand Exchange Sample Preparation

QD samples for NMR were prepared using either $CDCl_3$ or d_8-toluene. Samples were prepared in 1mL of deuterated solvent by drying 20 μM of QDs, the desired equivalents of **FFC** (or other molecule for control experiments), and 1.1 μM of hexamethylcyclotrisiloxane as the internal standard. We initially used $CDCl_3$ for the ligand exchange in air, enclosed in a foil-covered box on a stirring plate to avoid light, followed by drying the mixture after NMR experiments and subsequently dissolving the mixture in toluene in the glovebox. However, upon repeated illumination cycles, we noticed degradation of the QD PL, which we attributed to possible formation of HCl from any residual $CDCl_3$ or other stabilizing agents in $CDCl_3$. As a result of noticing this trend, we switched to using d_8-toluene in the glovebox for the ligand exchange in a foil-covered box on a stirring plate to avoid light. Most figures used this procedure, but some

supplementary figures are based on using $CDCl_3$ prior to air-free toluene. We note whenever this is the case and also note that this discrepancy does not affect any of our conclusions.

3.4.7 Optical Spectroscopy Sample Preparation

All samples were prepared in 2-mm cuvettes (Starna) and sealed with PTFE tape and Parafilm in a nitrogen glovebox before any optical spectroscopy or illumination experiments to avoid the presence of oxygen or water, which are known to react with QDs upon illumination. Non-deuterated toluene was distilled and freeze-pump-thawed prior to use in the glovebox.

3.4.8 Illumination Experiments

Illumination experiments were done using a UV lamp (Cambridge UVGL-15 Compact UV Lamp with a peak at 365 nm and measured power of 0.6 mW) and a strip of LEDs (superbrightleds.com with a peak at 532 nm and measured power of 1.6 mW) taped to a glass dish, **Figure 3.13**. Powers were measured with a Thorlabs PM100 power meter. Samples were stirred during illumination.

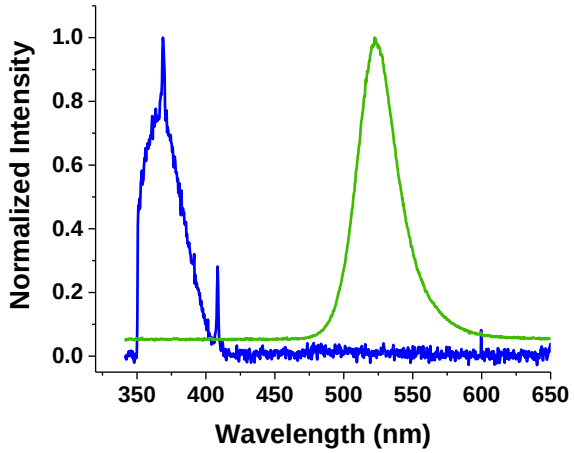

Figure 3.13. Spectra of the UV lamp (blue) and green LEDs (green) used for illumination experiments. Spectra were measured with a Ocean Optics Jaz spectrometer.

3.4.9 Determination of PSS

In a glovebox, ***Z*-FFC** (0.660 mg, 2.17 μmol) was dissolved in 520 μL of toluene-d_8 that had been degassed via freeze-pump-thaw cycling and dried over molecular sieves. The solution was transferred to and sealed in a quartz J. Young NMR tube before being removed from the glovebox. The sample was irradiated with a 365 nm lamp for 75 minutes. The distribution of photoisomers was then measured using ^{1}H NMR and the peak assignments above (Section III). Irradiation for an additional 15 minutes did not change the distribution, indicating that the sample had reached the PSS. The measured PSS at 365 nm in toluene is 52% C, 26% *E* (open), and 22% *Z* (open), as reported in the main text. Irradiation with green LEDs for 30 minutes led to complete consumption of the closed isomer, and the distribution of the open isomers was measured by ^{1}H NMR to be 75% *E* and 25% *Z*, as reported in the main text. Uncertainties of ± 5% were estimated by varying the range of integrated regions in the NMR spectra.

3.4.10 Spectral Deconvolution of Photoisomers

In a glovebox, ***Z*-FFC** (1.120 mg, 3.68 μmol) was dissolved 7.0 mL of toluene. The resultant sample was divided into three portions and diluted to concentrations of 0.526 mM, 0.262 mM, and 0.105 mM in septum-capped quartz cuvettes. The samples were removed from the glovebox and their UV-Vis absorption spectra were recorded. The samples were then subjected to the same course of irradiation and measurement as the NMR sample used to determine the PSS above.

In MATLAB, we constructed a calibration curve at each wavelength using the three different concentrations and the Beer-Lambert Law. The extinction coefficients that we extracted are linear combinations of the extinction coefficients of the three photoisomers with weights determined by the relative distribution of the isomers, *i.e.* the PSS distributions measured above (Section IV). By

assigning the initially measured spectra to exclusively the *Z* isomer, the *E* isomer signal could be derived by subtraction of the appropriately weighted *Z* spectrum from the post-green irradiation data. Similarly, we determined the C spectrum by subtraction of the weighted *E* and *Z* spectra from the post-365 nm data. The uncertainties in Figure 1 are dominated the uncertainties in the PSS measurement above.

3.4.11 Quantum Yield of FFC Isomerization

The quantum yield of photochemical closing and opening isomerizations of **FFC** were measured using potassium ferrioxalate actinometry.[155] We used the potassium ferrioxalate chemical actinometer to determine the total photon flux upon a 1 cm quartz cuvette irradiated with a 370 nm Kessil lamp passed through a UV bandpass filter and with a strip of blue LEDs from superbrightleds.com (470 nm). The total photon fluxes were (2.1 ± 0.1) X 10^{16} s^{-1} and (4.72 ±0.38) X 10^{16-} s^{-1}, respectively. 556 mg of ***Z*-FFC** were dissolved in 3.5 mL of toluene in a 1 cm quartz cuvette equipped with a magnetic stirrer. We then used the measured light sources to induce closing and opening photoisomerization of ***E*-FFC** and **C-FFC**, respectively. The kinetics of the reactions were tracked by measuring the absorbance of **C-FFC** at 463 nm with UV-Vis. Using the extinction coefficient of closed isomer at 493 nm determined above, changes in 463 nm absorbance upon irradiation were converted into absolute rates of **C-FFC** formation or consumption: 1.53 x 10^{15} s^{-1} and 5.91 x 10^{15} s^{-1}, respectively. These values were compared to the total photon flux and the extinction coefficients at 370 nm and 470 nm determined above to determine overall closing and opening quantum yields. These values are 20 ± 3% and 14.4 ± 0.8%, respectively.

3.5 Chapter Conclusion

In summary, we have demonstrated stable, reversible switching of the PL of colloidal QDs between "on" and "off" states, where the intensity of the PL in the "off" state is 20% of that in the "on" state. This switching is mediated by surface-bound photochromic fulgide molecules, which accept electrons from the photoexcited QD in their closed conformation at a rate that is a factor of four faster than in their open conformation. Unlike analogous FRET-based systems, in which the output of the system (the PL of the QD) degrades the response of the system by incidentally inducing the photoisomerization of the bound photoswitch molecule (an unavoidable complication given the spectral overlap of donor and acceptor required for FRET), our PET-based system does not require this overlap and is therefore non-destructive. We anticipate that this or analogous systems will be useful in optical memory applications, particularly nondestructive fluorescent readout, where the read, write, and erase steps need to occur at different incident wavelengths.[125,126] The fast reversible electrocylization of the fulgide and fast PET in this system may further enable experimental investigations of non-equilibrium systems, such as those in which the PET and photoisomerization processes are on commensurate timescales and therefore influence each other's yields; we have theoretically explored such systems.[156] Our results demonstrate that the on/off ratio of this type of remote photoswitch is highly sensitive to the rate of PET, which is, in turn, tunable through the frontier orbital energies of the QD and photoswitch. These features provide handles with which to further optimize this system, and/or tailor it for applications in memory, electronics, or imaging.

Chapter 4: Mechanism of Long-Range Energy Transfer from Quantum Dots to Black Phosphorus

Adapted from:

Padgaonkar, S.*; Brown, P. T.*; Jeong, Y.; Cherqui, C.; Avanaki, K. N.; López-Arteaga, R.; Irgen-Gioro, S.; Wu, Y.; Sangwan, V. K.; Schatz, G. C.; Hersam, M. C.; Weiss, E. A., *submitted.*

(* indicates equal contribution)

4.1 Chapter Summary

This chapter explores the mechanisms of long-range energy transfer (EnT) from a self-assembled film of CdSe/ZnS core-shell quantum dots (QDs) to black phosphorus (BP) nanoflakes through an AlO_x encapsulation layer of variable thickness. The dependence of the EnT on donor-acceptor distance, d, scales as $\sim d^{-2.3}$, which is shallower than the theoretical scaling of $\sim d^{-3}$ for Förster-type EnT from a zero-dimensional (0D) donor to a three-dimensional (3D) acceptor. Electrodynamic simulations reveal that the efficient long-range EnT is attributable to the high areal concentration of the QD film, which results in scattering of a donor QD's dipole field by neighboring QDs, thereby effectively increasing the area over which the donor and acceptor couple. The demonstration of efficient photosensitization of BP through a passivating dielectric layer is important for the development of high-performance optoelectronic devices based on ambient-reactive layered semiconductors.

4.2 Introduction

Black phosphorous (BP) is a promising layered two-dimensional (2D) semiconductor for optoelectronic applications due to high carrier mobility (>10^2 cm/Vs at room temperature) and direct bandgap at all thicknesses ranging from near-infrared to mid-infrared wavelengths.[157,158] However, BP shows dramatic chemical reactivity upon exposure to ambient conditions, such as air, light, and water,[159] and therefore, facile and scalable encapsulation schemes, such as atomic layer deposition of alumina (AlO_x), are required for long-term stability necessary for practical applications.[160,161] In general, these encapsulation layers are considered extraneous and do not participate in the operating mechanism of the devices. Given notable electron and hole mobilities, one promising application of BP enabled by its encapsulation is as a charge transport layer in

photodetectors.[162] While BP is not a strong absorber itself (absorption cross-sections of 10^{-16} cm^2 at 515 nm),[163] which limits its responsivity in photodetector applications,[164,165] performance of these devices can be improved by photosensitizing BP by another light-absorbing material. In this scenario, energy must be subsequently transferred from the photosensitizer to the BP, through the encapsulation layer.[105,166] Such energy transfer (EnT) must be accomplished in high yield over several nanometers, since, for instance, a minimum of 3 nm of AlO_x is required for indefinite chemical stability of BP.[160] For this purpose, Förster-type EnT is a viable sensitization strategy because it occurs through near-field electromagnetic coupling and has been observed to occur at yields of >50% even when donor-acceptor distances are 35 nm, is the most viable sensitization strategy.[167,168] This long-range mechanism stands in contrast with charge transfer, which has proved effective in using semiconductor quantum dots (QDs) to photosensitize ambient-stable 2D materials such as graphene.[169]

In the point-dipole implementation of Förster theory, which is only appropriate for describing systems with zero-dimensional (0D) donors and acceptors, the rate and yield of EnT scales with the donor-acceptor distance, d, as $\sim d^{-6}$.[105,170] Modifications to this simple model must be made in studies of systems with higher dimensionality, where, experimentally, scalings of $\sim d^{-4}$ in 0D-2D systems[171,172] and $\sim d^{-2}$in 2D-2D systems[168] have been observed. Other studies have found that parameters such as the thickness of a 3D acceptor thickness can perturb the distance dependence of EnT.[173,174] Clearly, the magnitude of the electromagnetic coupling that mediates EnT is sensitive to many structural and electronic parameters of the donor-acceptor system; so, to maximize the yield of photosensitization, we must characterize the distance-dependence of

Förster-type EnT for each system of interest, and develop models to link that distance dependence to as many parameters as possible.

Here, we photosensitize multilayer BP with 0D semiconductor QDs, which have large absorbance cross-sections and high photoluminescence quantum yields. QDs are common choices for photosensitizing 2D materials, but these studies have been so far been limited to materials that are stable in ambient conditions and therefore unencapsulated.[168,172–183] Our mixed-dimensional system comprises a monolayer film of close-packed CdSe/ZnS QDs deposited on AlO_x-encapsulated BP nanoflakes. By varying the thickness of the AlO_x layer between 3 and 20 nm, we determine that the rate of EnT scales as $\sim d^{-2.3}$, and the Förster radius, where the probability of EnT from QD to the BP equals the probability of QD exciton decay, is 11 nm. Finite difference time domain (FDTD) simulations of the electrodynamic interactions within our system allow us to attribute this shallow distance dependence and large Förster radius to i) the 3D nature of the BP acceptor (at a thickness of 20-30 nm, the flakes are electronically bulk-like),[162] and ii) the pseudo-2D nature of the close-packed monolayer of QDs, which enables dipole-dipole interactions within the donor sheet,[184] in contrast with prior studies that used isolated single particles or more dilute films of QD donors.[171–174,176,177,179,185] Thus, our study provides a general strategy for long-range photosensitization of ambient-reactive materials through their encapsulation layers that is translatable to a wide variety of photosensitizers and 2D charge transport layers.

4.3 Results and Discussion

4.3.1 Synthesis and Characterization of QD/AlO_x/BP System

Figure 4.1a shows a schematic diagram of our system. We synthesized CdSe/ZnS QDs with average diameter of 4.7 ± 0.7 nm and average emission energies of 530 nm using reported

procedures.[144,186] We obtained isolated BP flakes through micromechanical exfoliation from commercial crystals onto 300-nm SiO_2/Si substrates, and encapsulated the BP flakes with atomic layer deposition (ALD) of AlO_x with thicknesses between 3 nm and 20 nm.[160,187] Unencapsulated BP degrades within minutes of exposure to air due to reactions with ambient oxygen and water,[188]

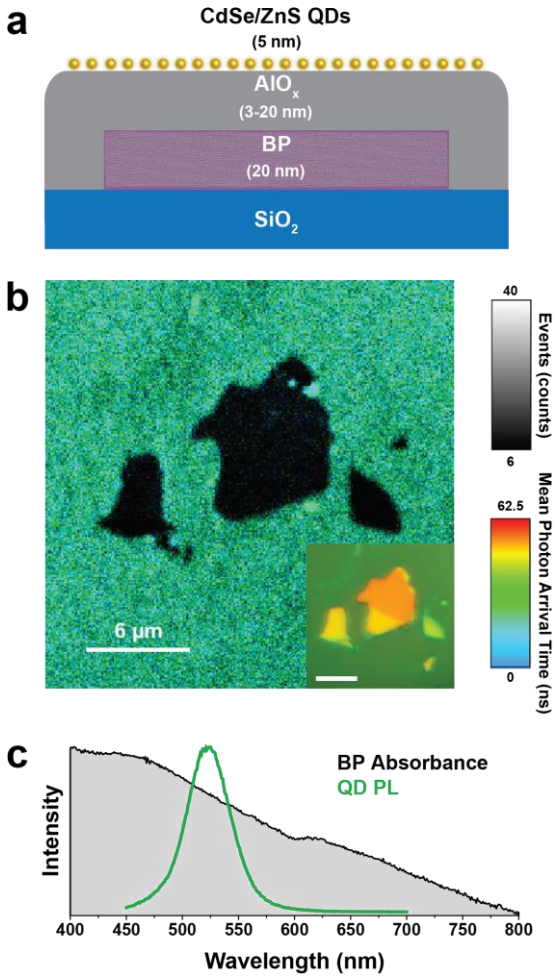

Figure 4.1. (a) Schematic of QD/AlO_x/BP system, not to scale. **(b)** FLIM map of a QD monolayer film deposited on 3 nm of ALD-grown AlO_x on exfoliated BP, on an Si/SiO_2 substrate. The top grayscale bar (black to white) indicates the intensity of the PL in the FLIM map. The bottom color bar (blue to red) indicates the average lifetime of the PL in the FLIM map. Inset: Optical image of the same area, with the same scale bar. **(c)** Ground-state absorbance spectrum of exfoliated BP on glass (black) and emission spectrum of CdSe/ZnS QDs (green). The y-axis has arbitrary units as the graph is intended to show overlap of the two spectra. The discontinuity in the absorbance at ~625 nm is due to a grating change in the spectrometer.

but we observe no signs of degradation in air after four weeks of encapsulation, consistent with previous reports.[160] We deposited a close-packed monolayer film of the QDs self-assembled at the liquid-air interface onto the surfaces of the AlO_x-coated BP flakes using a method described elsewhere.[189] This method produces a densely covered substrate, as seen in the by fluorescence lifetime imaging microscope (FLIM) image, **Figure 4.1b**, and equal coverage on and off the BP flakes, as measured by atomic force microscopy (AFM, **Figure 4.2**).

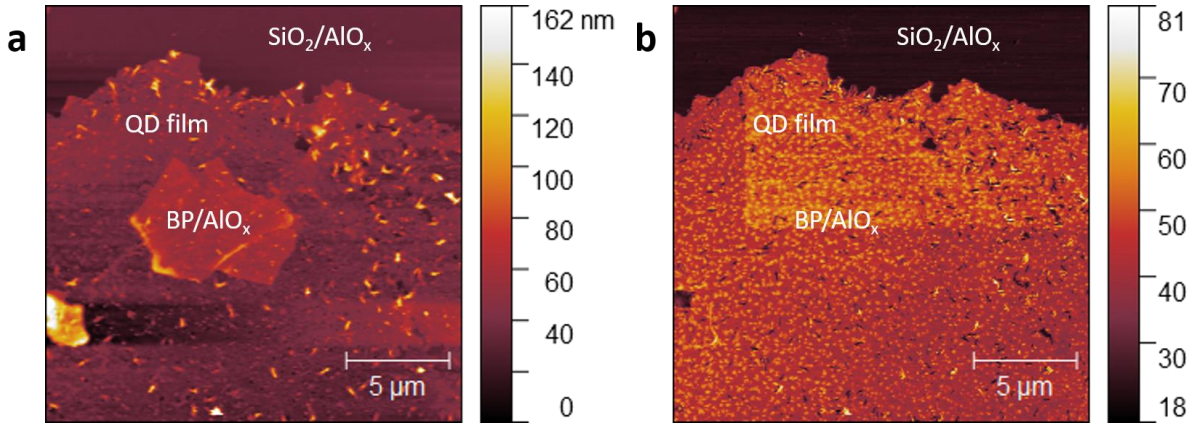

Figure 4.2. (a) Representative AFM topography micrograph of the QD film on the BP/AlO_x sample. The top of the micrograph shows the edge of the self-assembled QD film. The film is mostly close-packed and uniform, other than some pinholes and residue from deposition. The film shows no visible difference on the BP flakes compared to off. **(b)** Phase image from the same scan, showing clearly where the breaks in the QD film are (the darker, lower-phase regions). The phase shift of the QD film on the BP flake is indistinguishable from off the BP.

The FLIM map, **Figure 4.1b**, also confirms that deposition of the QDs on the BP flake quenches their photoluminescence (PL). This result indicates that BP introduces a competitive nonradiative decay process for excitons in the QDs. Although we cannot monitor the PL of the acceptor (BP) because its emission is in the mid-infrared spectral region and outside the range of our detector, we provide experimental evidence supporting Forster-type EnT such as (i) the spectral overlap of the emission of the QDs and the broad absorbance of BP, **Figure 4.1c**, and (ii) the ≥6-nm insulating barrier (comprised of a ~1-nm ZnS shell, ~2-nm oleate/octadecylamine

ligand shell, and >3-nm AlO_x layer), which prohibits electron transfer from the conduction band of photoexcited CdSe QDs to the conduction band (CB) of BP, even though it is energetically allowed.[190] Dexter-type EnT, a semi-concerted transfer of both electron and hole, is eliminated for the same reason.

4.3.2 Distance Dependence of EnT

Time-resolved PL (TRPL) traces, **Figure 4.3a**, extracted from FLIM maps like that shown in **Figure 4.1b** show that the lifetime of the QD exciton increases monotonically as the distance between QD and BP increases, as controlled by the thickness of AlO_x encapsulation. **Figure 4.3b** is a plot of the amplitude-averaged lifetime of the QD exciton, calculated from multi-exponential fits of the traces in **Figure 4.3a**, as a function of the donor-acceptor (QD-BP) distance, which includes the 2.5-nm radius of the QD, the estimated 2.4-nm length of the oleate/octadecylamine ligands on the QD surfaces, and the ≥3-nm AlO_x encapsulation layer on BP. Without underlying BP, the amplitude-averaged PL lifetime, $\tau_{ex,0}$, of the QDs deposited on AlO_x is 10.4 ns. In presence of BP encapsulated by 3-nm AlO_x, the average PL lifetime of the QDs, τ_{ex}, decreases to 3.7 ns. With increasing thickness of AlO_x, the PL lifetime increases, eventually reaching 9.7 ns for a 20-nm-thick AlO_x layer (the thickest layer in this study), which is within 8% of the lifetime measured in the absence of BP, **Figures 4.3a,b**.

We calculate the EnT rate as in eq 4.1, assuming

$$k_{EnT} = \frac{1}{\tau_{ex}} - \frac{1}{\tau_{ex,0}} \qquad (4.1)$$

that EnT is the sole non-radiative process that accelerates exciton decay in the presence of BP,[191] and define the EnT efficiency, *E*, by eq 4.2. **Figure 4.3c** (black) is a plot of the EnT efficiency versus

$$E = 1 - \frac{\tau_{ex}}{\tau_{ex,0}} \quad (4.2)$$

the donor-acceptor distance, fit with eq 4.3, where d is the variable donor-acceptor distance (from

$$E = \frac{{R_o}^n}{{R_o}^n + d^n} \quad (4.3)$$

the center of the donor QD to the surface of the acceptor BP), R_o, the effective Förster radius, at which the probability of EnT is equal to the probability of native radiative or nonradiative processes within the QD, and n is the total dimensionality of the system.[192,193] This fit yields n =

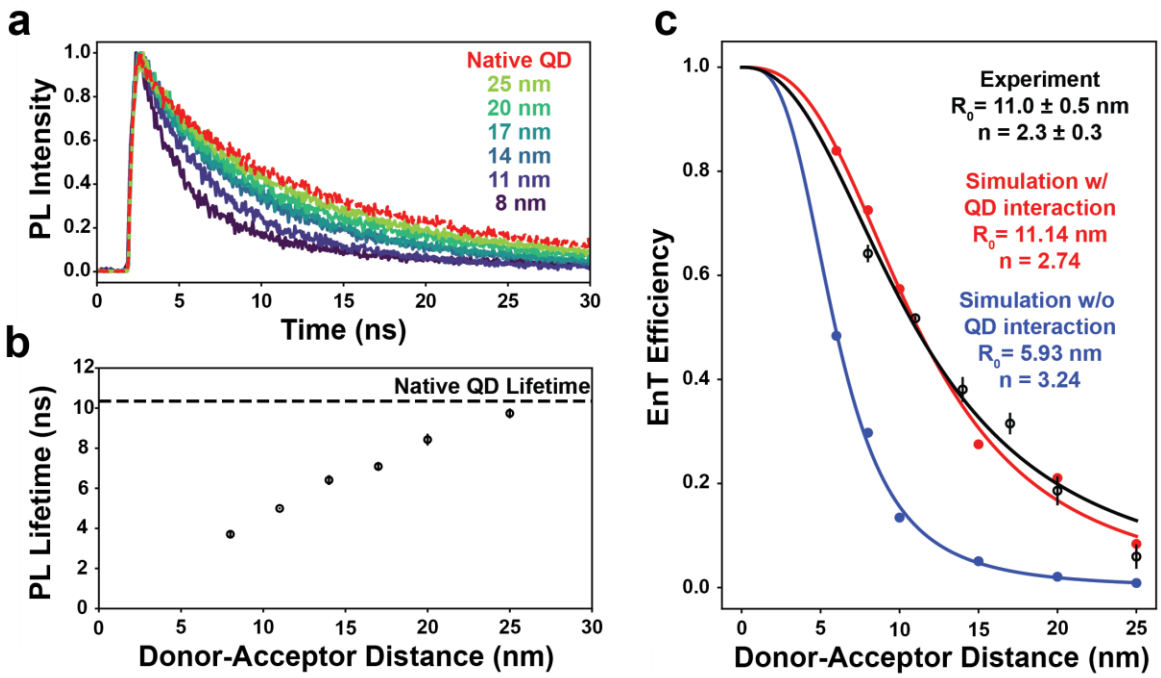

Figure 4.3. (a) Decay of the PL of the QDs deposited on BP with time after excitation, for AlO_x spacer layers of varying thickness; the legend shows the corresponding total donor-acceptor distances. "Native QD" corresponds to QDs deposited on AlO_x without underlying BP. These kinetic traces are averaged across three to five measurements at separate locations on the BP flakes for each AlO_x thickness. **(b)** Amplitude-averaged excitonic lifetime determined from bi-exponential fits of the traces in (a) as a function of donor-acceptor distance. The dashed line is the native QD lifetime. **(c)** Experimental EnT efficiency, defined by eq 4.2, as a function of donor-acceptor distance, fit with nonlinear regression (black). Simulations of this quantity with (red) and without (blue) QD interactions (scattering and absorption of the electric field from photoexcited QDs by the surrounding QDs).

2.3 ± 0.3 and R_o = 11.0 ± 0.5 nm, which is 3 nm longer than the donor-acceptor distance (8 nm) corresponding to the minimum thickness of AlO_x required to stabilize BP (3 nm).

4.3.3 Role of QD Interactions on Distance Dependence of EnT

When the donor-acceptor distance is small compared to the wavelength of the photons being transmitted, quasistatic image dipole theory predicts that the rate of EnT from an isolated 0D donor to a 3D acceptor has a distance dependence of d^{-3} and that this trend should still hold even in the presence of an encapsulation layer.[194,195] The longest donor-acceptor distance in this experiment is ~25 nm, so the quasistatic approximation is valid. To explain the value of n (2.3 ± 0.3) we obtain by fitting the experimental data in **Figure 4.3c** to eq 4.3, we propose that the distance dependence of EnT in our system is influenced by scattering of the dipole fields of photoexcited QD donors by nearby QDs, which changes the spatial profile of the emitted electric field. From the quantum mechanical point of view, this scattering amounts to EnT to other QDs before absorption by BP.

Because it is difficult to model the system with many QDs and the acceptor analytically, we used finite-difference time-domain (FDTD) simulations to calculate the distance dependence of EnT from many photoexcited QDs to BP in two cases: (i) where the QDs interact with the electric field emitted by the other QDs, and (ii) where they do not. In these simulations, QDs that can scatter or absorb the electric field of other QDs are modeled as electric dipole sources enclosed by a dielectric sphere using a Lorentz model that includes the resonance response of the QD, and hypothetical non-interacting QDs are simply described as dipole sources without dielectric spheres (**Figure 4.4**). In both cases, we placed 100 QD dipole sources of the same magnitude and phase and random orientations and positions within a 200 nm × 200 nm region on the alumina layer

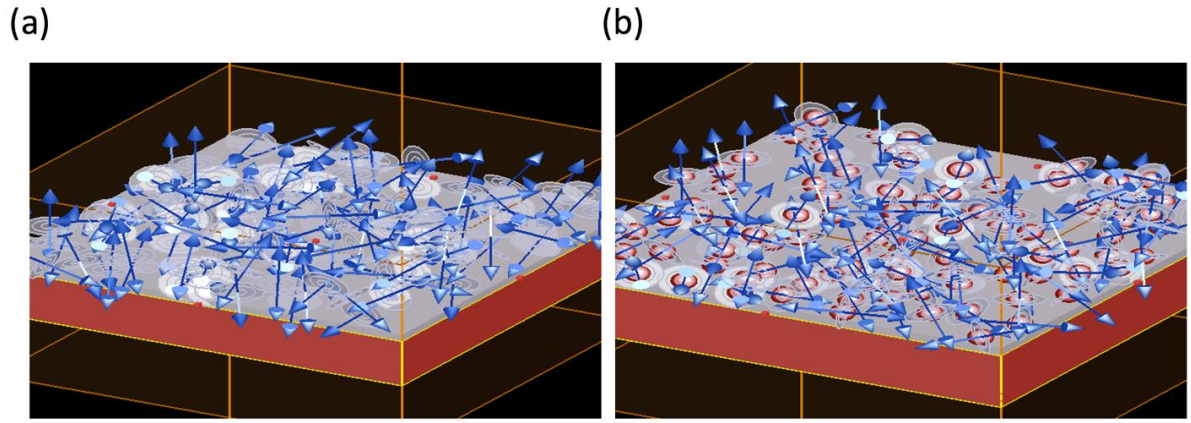

Figure 4.4. Schematic of FDTD simulations for the calculation of EnT efficiency with the BP layer (red) and alumina (grey). **(a)** Hypothetical noninteracting QDs are simply described as electric dipoles (blue arrows) of the same magnitude. **(b)** QDs interacting with each other (i.e., QDs can scatter and absorb the electric field emitted by other QDs) are described as dipole sources enclosed by a dielectric sphere (pink) of which the dielectric function is a Lorentz model.

(refractive index 1.7682) of varying thickness, which is comparable to the concentration of QDs in the experiment. A 35 nm-thick BP layer was placed below the alumina layer. We applied a periodic boundary condition in the *x* and *y* directions to repeat this 200 nm × 200 nm unit cell. To describe the broadband absorption of BP, the dielectric function was modeled as a superposition of five Lorentz models. We note that we have not considered that the ALD-grown AlO_x used in the experiment is not perfectly crystalline, which may result in mild absorption scattering by the alumina layer and therefore affect the distance dependence and Förster radius.

The absorption power of the BP layer was obtained and converted to the EnT rate using eq 4.4,

$$\frac{k_{EnT}}{k_0^{QD}} = \frac{P_{abs}^{BP}}{P_0^{QD}} \qquad (4.4)$$

where k_{EnT} is the EnT rate, k_0^{QD} is the emission rate of a native QD (the inverse of the lifetime multiplied by the measured quantum yield, QY of 52%), P_{abs}^{BP} is the simulated BP absorption power

in one unit cell, and P_0^{QD} is the emission or power of the QDs in one unit cell. To consider the finite emission lineshape of the QDs, we calculated P_{abs}^{BP} as a weighted average of the frequency-dependent absorption power $P_{abs}(\omega)$, where the weight was the emission spectrum of a native QD (modeled as a Gaussian function with a mean at 550 nm and a standard deviation of 15 nm). In the case where the dipole sources were enclosed by dielectric spheres, we applied a frequency-dependent correction factor that accounts for the change of the emitted power from the dipole–sphere composite structure due to the response of the dielectric sphere to $P_{abs}(\omega)$. Once we obtained k_{EnT}, the EnT efficiency is calculated with eq 4.5 (using τ^{QD}=10.5 ns).

$$E = \frac{k_{EnT}}{k_{EnT}+k_0^{QD}+k_{nr}^{QD}} = \frac{k_{EnT}}{k_{EnT}+1/\tau^{QD}} \qquad (4.5)$$

Figure 4.3c (red, blue) shows the calculated EnT efficiency E as a function of the donor-acceptor distance. When the QDs in the simulation include dielectric spheres that allow interaction with the electric field emitted by the other QDs, the R_0 increases from 5.93 nm to 11.1 nm, which agrees well with the experimental value of 11.0 nm. The distance dependence of the EnT rate is $d^{-3.2}$ for non-interacting QDs (as expected from the quasistatic image dipole theory for an isolated QD described above) and $d^{-2.7}$ for interacting QDs, which is closer to the experimental scaling of $d^{-2.3\pm0.3}$.

The simulations suggest that we attribute the unexpectedly long Förster radius and shallow distance dependence of the EnT rate in the mixed dimensional BP-QD system to QD–QD electrodynamic interactions. When QDs interact with one another, an excited QD can transfer its excitonic energy in the lateral direction to the nearby QDs before the energy is absorbed by the BP, as illustrated by the FDTD-calculated electric field profiles in **Figure 4.5.**[196] This interaction widens the area of BP that interacts with the initially excited QD, opening non-vertical channels

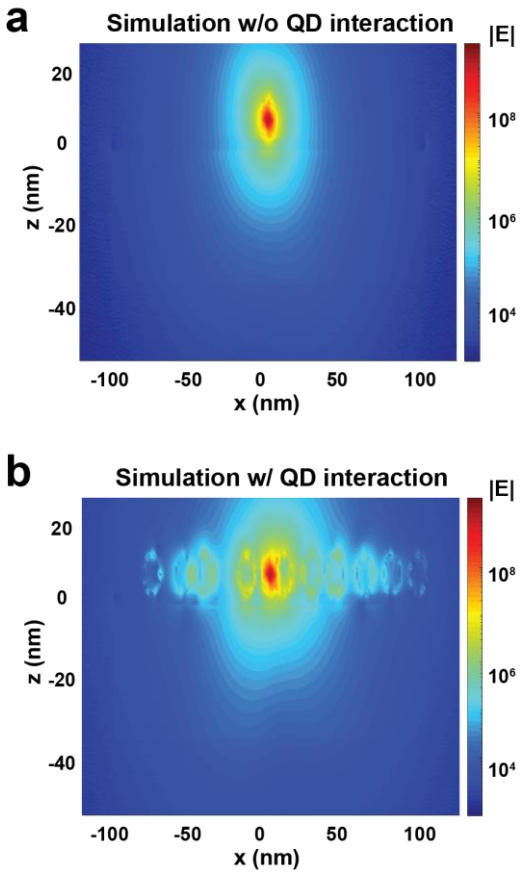

Figure 4.5. FDTD simulations of the spatial profile of the magnitude of the electric field |E| generated by a single excited QD modeled as a dipole source enclosed by a dielectric sphere **(a)** isolated and **(b)** surrounded by 10 ground-state QDs (dielectric spheres). The BP and the alumina layer spanned the region defined by $-100\ nm < x < 100\ nm$, $-100\ nm < y < 100\ nm$, and $-35\ nm < z < 0\ nm$ (BP) and $0\ nm < z < 3\ nm$ (alumina). The centers of all QDs were on the xz plane at $z = 8\ nm$. The center of the excited QD was at the origin, and the orientation of its dipole source was defined by spherical coordinates $\theta = 124°$ and $\phi = 0°$. The figures are the slices at $y = 0$ nm. The same dielectric functions for BP, alumina, and the QDs as those used for the calculation of the EnT efficiency were used.

for EnT. The lengths of these channels increase sub-linearly with increasing d, thus reducing the overall distance dependence of the EnT rate. We note that in these simulations we did not consider (i) the in-plane anisotropy of BP because the dipole moments of the QDs are isotropic and (ii) the thickness dependence of BP because for the range of thicknesses we measured, the EnT was similar.

4.4 Experimental Methods

4.4.1 Sample Preparation

CdSe quantum dots (QDs) were synthesized *via* a typical hot injection route,[144] and two layers of ZnS shell were added via the SILAR method.[186] The size of the QDs was determined from TEM micrographs that were analyzed in ImageJ, which produces a histogram of quantum dot diameters (**Figure 4.6**). The average quantum dot diameter was 4.7 nm, with a standard deviation of 0.6 nm. The black phosphorus (BP) flakes were mechanically exfoliated from purchased bulk crystals (American Elements) using scotch tape exfoliation in an inert nitrogen atmosphere. The exfoliated flakes were then mechanically deposited onto Si/SiO_2 substrates. After AlO_x deposition, the QD monolayer film was deposited using a self-assembling pseudo-Langmuir-Blodgett method.[197] Briefly, the sample chips are placed at the bottom of a 25 mL PTFE crucible and 2 mL of acetonitrile are added to submerge the sample. 60 µL of a dilute solution of CdSe/ZnS QDs in hexanes were carefully pipetted on the inner edge of the crucible until a self-assembled monolayer (and no bilayers) forms upon the surface. The crucible is then covered to allow the assembly

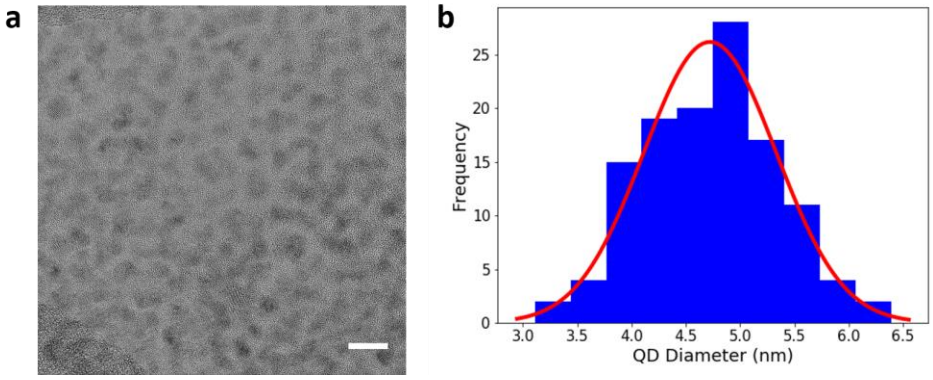

Figure 4.6. (a) Representative TEM micrograph of the QD film. The scale bar is 10 nm. **(b)** Frequency histogram of the quantum dot diameter, with 122 total QDs measured. The histogram was fitted to a normal distribution, shown in red, to give an average QD diameter of 4.7 nm with a standard deviation of 0.6 nm.

process to finish as the hexanes evaporate for 5 minutes and then the acetonitrile antisolvent is carefully pipetted out so that the QD monolayer film remains and deposits on the whole surface of the substrate including encapsulated BP flake.

4.4.2 Atomic Layer Deposition

Atomic layer deposition (ALD) encapsulation was done using a Cambridge Nanotech Savannah ALD system. The AlO_x precursors were trimethylaluminum (TMA) and H_2O. The growth per cycle of this AlO_x process is approximately 0.1 nm per cycle. For the encapsulation, the first 30 cycles, corresponding to ~3 nm, were performed at 55 °C, as that is the minimum required procedure to suppress visible degradation.[198] Because H_2O plays a major role in BP degradation mechanisms, these first 30 cycles were preceded by 10 pulses of just TMA to neutralize any surface contaminants and further protect the BP from the first pulse of H_2O. Following the first ~3 nm at 55 °C, the rest of the ALD was performed at 100 °C to reach the varying thicknesses that determined the donor-acceptor distances. This ALD encapsulation successfully passivated the BP samples used in this study, showing no visible degradation after several weeks (**Figure 4.7**).

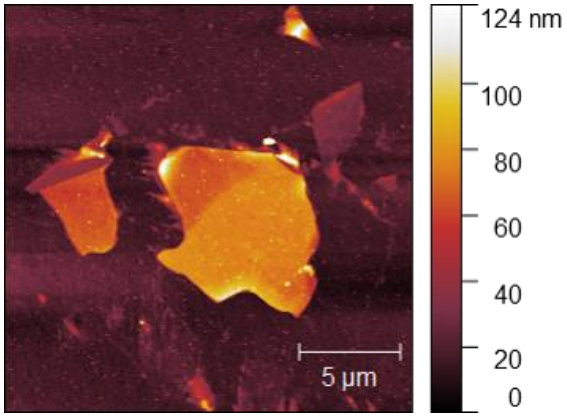

Figure 4.7. Atomic force microscopy (AFM) micrograph of an ALD AlO_x-encapsulated QD/BP heterostructure after at least a week in ambient exposure, showing no visible surface degradation. This micrograph was taken after the TCSPC experiment, so the QD film as well as some residue from QD deposition is visible.

4.4.3 Fluorescence Lifetime Measurements

Spectroscopic measurements of fluorescence lifetimes were conducted using a lab-built time-resolved photoluminescence (TRPL) confocal microscope.[199] Our microscope consists of a piezo scanner (NanoPI, Physik Instrumente), an APD detector (MicroPhoton Devices), and a photon counting board (PicoHarp300, PicoQuant) where correlation times between the excitation pulses and detected photons were recorded. The excitation pulses were generated from a 450-nm, 70-ps pulsed laser at a repetition rate of 8 MHz (Picoquant) and focused with a long working distance objective (0.7 NA, 100x, Mitutovo), and the detected PL was filtered with a 475-nm long-pass dichroic (Chroma) and a 495-nm long-pass filter (Thorlabs). Image reconstruction were carried out using commercial software (SymphoTime 64, PicoQuant). Lifetimes were analyzed using a custom-written Python script. Although the acceptor thickness has been shown to have an effect on fluorescence lifetime for a given donor-acceptor distance near the monolayer thickness limit,[200–

[203] there was no significant observed thickness dependence for the range of thicknesses used in this study (**Figure 4.8**).

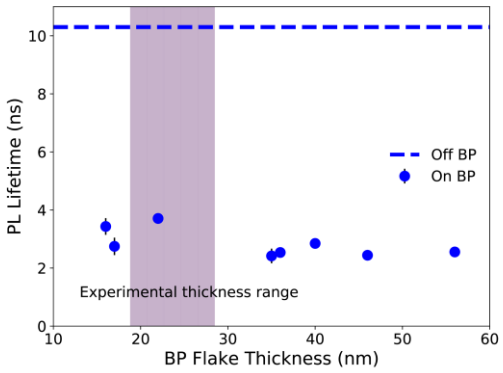

Figure 4.8. QD fluorescence lifetime dependence on BP flake thickness, showing the native QD fluorescence lifetime of ~10.4 ns for reference. Lifetimes were measured at an AlO_x thickness of 3nm, corresponding to a donor-acceptor distance of ~8 nm, and then amplitude-averaged. The range of thicknesses of the BP flakes used in this study is shaded in light purple.

Excited state lifetimes were calculated both as amplitude average lifetimes and intensity average lifetimes from the biexponential fits of TRPL decays. Amplitude average lifetimes are calculated using the formula

$$\tau_{avg,amp} = \frac{\sum A_i \tau_i}{\sum A_i}$$

while intensity average lifetimes are calculated using the formula

$$\tau_{avg,int} = \frac{\sum A_i \tau_i^2}{\sum A_i \tau_i}$$

Both averages are shown as functions of donor-acceptor distance in **Figure 4.9**, and the EnT efficiencies calculated using both averages are shown as functions of donor-acceptor distance in **Figure 4.10**. For the amplitude-averaged EnT efficiency, the fitted data gave R_0 = 11.0 ± 0.5 nm

and n = 2.3 ± 0.3 (R^2 = 0.95). For the intensity average EnT efficiency, the fitted data gave R_0 = 10.8 ± 0.7 nm and n = 2.0 ± 0.3 (R^2 = 0.91).

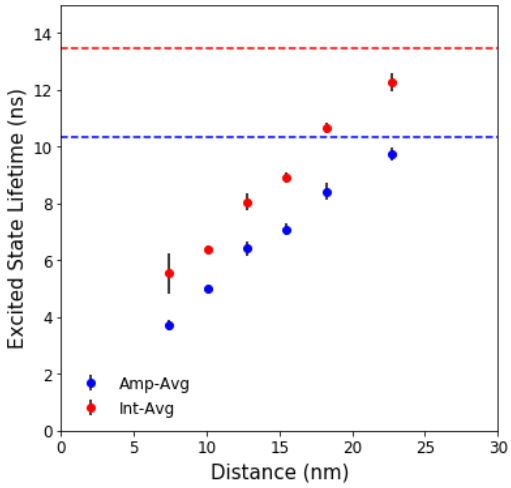

Figure 4.9. The excited state PL lifetimes, calculated as amplitude average and intensity average lifetimes from the biexponential fits of the TRPL decays, as a function of donor-acceptor distance. The blue dashed line corresponds to the amplitude average native QD lifetime, while the red dashed line corresponds to the intensity average native QD lifetime.

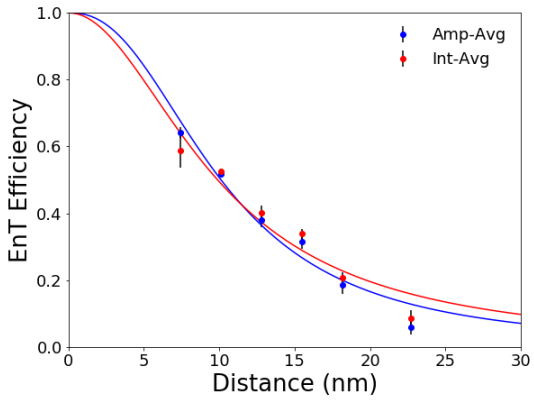

Figure 4.10. The EnT efficiencies calculated from the amplitude average lifetimes (blue) and intensity average lifetimes (red) as a function of donor-acceptor distance.

4.4.4 FDTD Simulations

We used finite difference time domain (FDTD) simulations using Lumerical FDTD Solutions to calculate the EnT efficiency where the dipole field from photoexcited QDs can be scattered or

absorbed by the other QDs and in the other case where the QDs do not interact with each other.[204] A schematic of the simulations is described in **Figure 4.4**. The hypothetical non-interacting QDs were simply described as electric dipoles (blue arrows). In the case interacting QDs, each dipole was enclosed with a dielectric sphere (pink sphere) to model the QDs that emit, scatter, and absorb radiation. The dielectric functions for the QDs amd alumina are described in the main text. To describe the broadband absorption of BP, the dielectric function was modeled as a superposition of five Lorentz models with the resonance frequency, linewidth, and oscillator strength sets $(\omega_0, \gamma, f_{osc}) = (0.3\ eV, 0.5\ eV, 0.5\ eV^2)$, $(0.5\ eV, 1.0\ eV, 0.5\ eV^2)$, $(1.0\ eV, 1.0\ eV, 0.5\ eV^2)$, $(2.0\ eV, 1.0\ eV, 0.5 eV^2)$, and $(2.25\ eV, 1.0\ eV, 0.5\ eV^2)$. Mesh accuracy of 4 was chosen, and a finer mesh of interval 1 nm in the x and y direction and 0.5 nm in the z direction extended through 50 nm above the QD layer and 50 nm below the BP. The simulation region spanned 1000 nm in the z direction, and 8 perfectly matched layers (PMLs) were placed at the top and bottom of the simulation region. The background medium was vacuum. In the simulations of the spatial profile of the magnitude of the electric field generated by a single photoexcited QD, where ground-state QDs were optionally present nearby, boundary conditions are not applied and the simulation region spanned 800 nm in the x, y, and z directions.

4.5 Chapter Conclusion

In summary, we demonstrate long-range Förster-type energy transfer from a self-assembled monolayer of CdS/ZnS QDs to 3D BP through an AlO_x encapsulation layer, with a shallow distance dependence of $\sim d^{-2.3}$ and a Forster radius of 11.0 nm. We attribute the robust EnT over relatively long distances to electrodynamic interactions among QDs within the monolayer, which effectively increase the interfacial area over which the donor and acceptor couple. Correspondence

between experimental and simulated results suggest that specific parameters of the solid state donor-acceptor system – the dimensionality of both the donor and acceptor – can be tuned in order to lengthen the distance over which high-yield EnT occurs. Therefore, this work provides design principles for the sensitization of ambient-reactive materials through the encapsulation layer. More broadly, it provides a general theoretical framework for evaluating Förster parameters for various mixed dimensional systems consisting of bulk, thin-film, and self-assembled nanomaterials.

.

Chapter 5: *Science with Seniors*: A Model Program for STEM Outreach Focused on Senior Citizens

Adapted from:

Padgaonkar, S.; Schafer, E., *Journal of Higher Education Outreach and Engagement*, in press.

5.1 Chapter Summary

While many science, technology, engineering, and math (STEM) outreach programs focus on children, relatively few efforts are dedicated to voting-age populations. These groups are important to reach because misinformation about science is widespread and difficult to detect, often preventing informed voting on science-related issues. *Science with Seniors (SwS)* addresses this critical gap by bringing science research topics and news to the most dedicated voting demographic, senior citizens, through informal science presentations at local senior centers in the greater Chicago area. Over the last three years, graduate students and postdoctoral associates involved in *SwS* have presented on a variety of current and relevant science topics. Participants in the program indicate on surveys that *SwS* has been successful because it has increased their understanding of the presented topics and they would attend similar programs in the future. Given this positive feedback, *SwS* demonstrates a way to bring STEM outreach and accessible science knowledge to older voting populations, and a general program development methodology is outlined so that this graduate student-led model can be implemented elsewhere. Future directions include program expansion, increased accessibility with online compatibility, and evaluation of long-term effects of this program on participants' voting habits and appreciation of science.

5.2 Introduction

The relationship between Americans and their views on science is, in general, complicated. On one hand, the vast majority of Americans trust scientists and believe that investment in science pays off in the long term.[205] As a whole, Americans' public understanding of science has generally increased over time.[206] In contrast, Americans have become increasingly more susceptible to misinformation about science, a trend fueled by the increasingly important roles played by media

and political polarization in recent years.[205] The majority of Americans share views with scientists on most topics, but certain issues, such as climate change or genetically modified organisms, tend to have large disparities between scientists and the public.[207,208] Alongside this troubling trend, stark differences exist between different age groups on surveys measuring public understanding of science. More often than not, older adult Americans (aged 65+) tend to score lower than their younger counterparts.[209] Independent of their performance on these science literacy tests, senior citizens tend to vote at much higher rates than other demographic age groups. In 2016, over 90% of senior citizens were registered to vote, and over 70% turned out to vote, in contrast with just over 45% for Americans ages 18-29.[210] Scientific information is important in informing policy, but misinformation can just as easily be used to create policies by influencing voters and public opinion. As a result, it is crucial that this highly dedicated voting group should be properly informed about scientific issues, particularly those that have policy implications.

There are two primary ways that scientists engage the public: direct outreach (through public talks, conversations, or interactive activities) or citizen science (by creating projects where the public can contribute with data collection or analysis). While there are a number of successful examples in which older adults engaged in citizen science projects, this paper's primary focus is to understand effective program development for science outreach with senior citizens and will therefore not discuss these citizen science efforts in depth.[211–214]

Currently, nearly all science, technology, engineering, and math (STEM) outreach efforts focus on increasing early interest in science among younger populations (children ages < 18).[215–217] STEM graduate students are often eager to volunteer in such programs, motivated by intrinsic emotional benefits, a desire to enhance their teaching skills for career advancement, and the

perceived ease and fun of teaching children.[218] These programs are often short-term and low-commitment endeavors for volunteers, involving brief lesson plans with interactive demonstrations, crafts, or other physical activities.[217] These outreach efforts aim to instill a love and appreciation of science early in childhood, reinforce broad skills for their education, and inspire large percentages of students to pursue science-based careers.[218] While this form of outreach is certainly important to build the next generation of scientists and emphasize informed science knowledge in all stages of life, it overlooks the general population of adults that are current eligible voters.

The most reliable voters in elections are senior citizens, yet to our knowledge, only two STEM outreach efforts have reported targeting this critical demographic. At the University of Missouri, the *Science and Me* program consisted of a novel 15-week graduate course that was designed to train graduate students to build effective science communication skills. Over the course of two years, students who participated in this program gave 62 presentations and reached over 1,000 adults in independent living facilities, public libraries, and college reunions.[219] Feedback of these efforts was largely positive – audience members thoroughly enjoyed the chance to learn about current research topics and students appreciated the chance to reach new audiences, as well as the ability to improve their science communication skills. Another STEM outreach program that targeted senior citizens consisted of a series of monthly astronomy-related lectures to a of audience members in senior living communities in Rochester, New York.[220] This endeavor not only enriched the lives of seniors who grew up during a time when space science was a growing and popular field but also reminded participants of the importance of funding scientific research and related technologies. One key takeaway from this program is that it built upon existing lifelong learning

initiatives (LLIs) at its community partners, in which senior living communities or senior centers hold educational programs on various topics, such as yoga, cooking, travel, or literature. The overall goal of LLIs is to improve cognition (and prevent cognitive decline) by continuing to engage mental faculties of participants through intellectually challenging material.[221] Additionally, LLIs promote intergenerational social interactions, prevent depression, and increase self-esteem and self-efficacy in decision-making processes.[221–224] What is also clear from well-established LLIs like the Osher LLI is that the most effective instrument of lifelong learning is to promote reflective judgement on previously held beliefs so that these can be critically analyzed and independently revised if necessary.[225] For reflective judgement to occur, such a format of learning should occur in an interactive way where a dialogue is encouraged between the student and teacher.

Learning from the successes and challenges of these programs, an optimal science outreach program for older adults would both teach a wide range of scientific topics in depth to community members in a long-term sustainable manner and promote reflective judgement through interactive and engaging formats. Such a program should seek to build a framework that can ensure the most civically-engaged demographic is scientifically informed by answering the following questions:

1. What are effective ways to engage senior citizens with science outreach?
2. How can senior citizens benefit from science outreach?
3. How does science outreach affect the attitudes towards science and voting habits of senior citizens?

In order to fill this gap in current outreach efforts and begin to answer these questions, we started an initiative through a graduate student and postdoctoral associate led organization known as the Science Policy Outreach Taskforce (SPOT) at Northwestern University (NU) that is

committed to advocating for science to policymakers and the general public. We (graduate student members of SPOT) have developed a model program called *Science with Seniors (SwS)*, in which graduate students and postdoctoral associates from NU bring their expertise to local senior centers and present brief, digestible science presentations on a variety of topics. While we encourage NU presenters to relate their talk to current science news or policies to strengthen the connection between a basic understanding of science and governmental decisions, as a nonpartisan organization, we avoid telling participants opinions or how to vote in upcoming elections. Overall, *SwS* seeks to inform participants about specific relevant science topics that impact our everyday lives, improve science literacy, and share an appreciation for scientific research and its outcomes, all of which can lead to more informed voting.

5.3 Results and Discussion

5.3.1 Program Development

In order to best reach this demographic, we chose face-to-face interactions so that we can readily combat misinformation, which rampantly spreads online, with personal conversations.[226,227] We developed SwS with a two-pronged approach to establish relationships with both community partners and presenters, as shown in **Figure 5.1**. To establish community partners, we contact local senior homes to gauge interest in partnering with SwS. We then visit the partner sites to understand how our values align. After giving a trial presentation, we establish a set of dates for presentations to take place and advertise these events at the partner site.

Alongside these efforts, we recruit presenters (STEM graduate students and postdoctoral associates) at NU through information sessions. Many prospective presenters have experience with science outreach already (primarily to children) and are especially interested in reaching new audiences in the greater Chicago community and a desire to grow their science communication skills. We train presenters by providing volunteer primers, which describe strategies for successful presentations, and past successful presentations. After presentations at the senior centers, we distribute surveys to solicit feedback from the participants to evaluate the program and continue

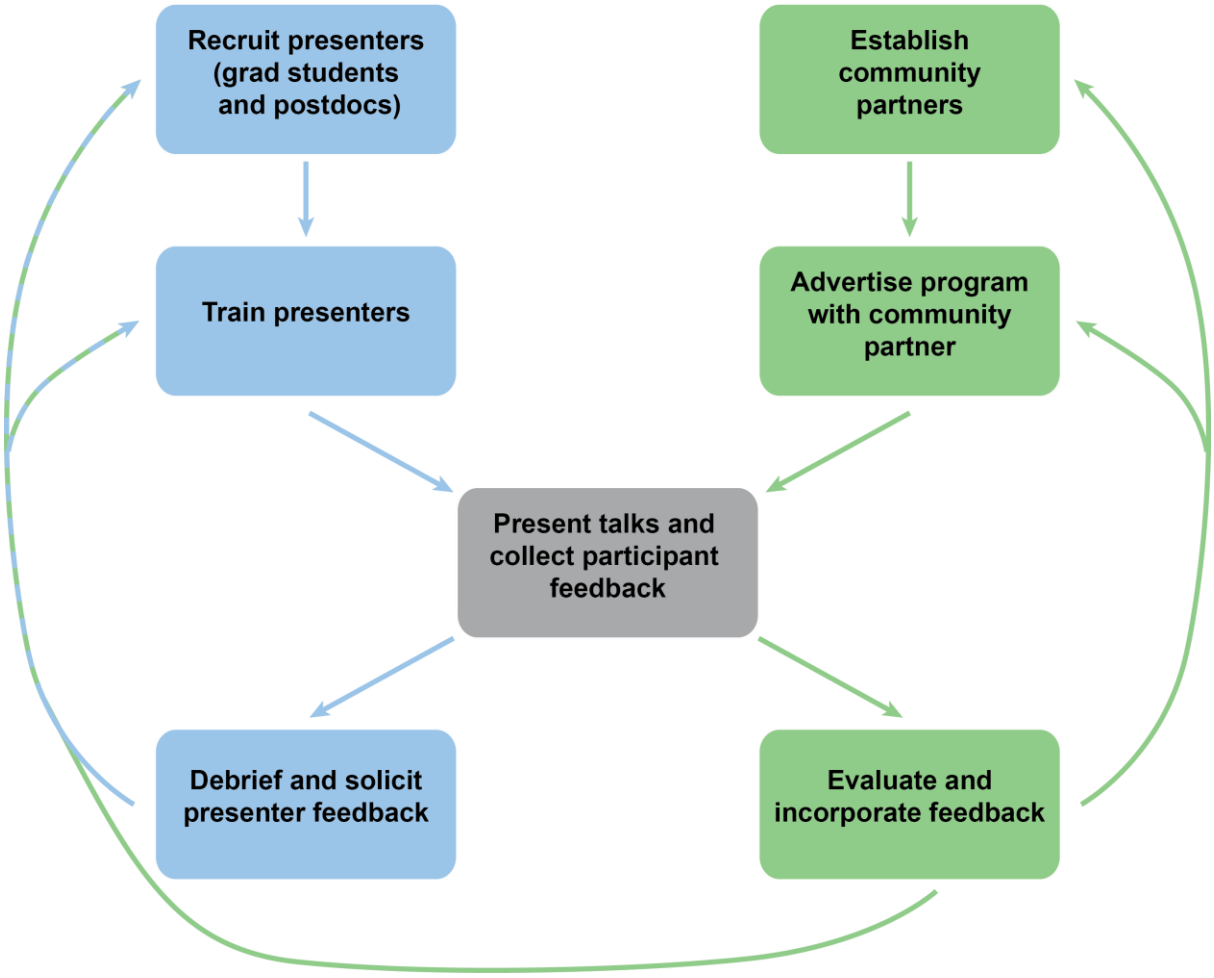

Figure 5.1. Program development steps to build relationships with community partners and presenters for a senior citizen-focused science outreach program.

advertising future presentations. Much of the feedback suggests future topics of interest and we recruit presenters with expertise in these topics. Other feedback about how the program can be improved, such as presentation style, is incorporated in the training step. Expansion to new senior centers is possible after having established a successful track record with the initial community partners. After the presentations, we also debrief with the presenters and solicit feedback on how to improve the program from a presenter perspective. This feedback is incorporated in the training and recruiting steps as well.

5.3.2 Community Partners

We established community partnerships with two local senior centers. In June 2017, we partnered with the Covenant Home in Andersonville, a northern neighborhood of Chicago. In December 2018, we partnered with the Levy Center in Evanston. The population of the Levy Center is comprised of independent community members since it is a daytime center, while the Covenant Home is a live-in senior residential home. While there are certainly differences in the demographic makeup and cognition capacity of seniors in each of these locations, we did not collect this information during the course of this program evaluation period because we used anonymized surveys to gather feedback. To build on this progress in the future as a science education research project, we would be interested in studying the differences in science literacy and overall understanding as a consequence of these presentations between the senior center populations and evaluating if personal characteristics (age, education, gender, cognitive health) play a role in individual attendance and behavior.

5.3.3 Format

Figure 5.2. A graduate student presenting on lab-on-chip technologies to seniors at the Levy Center in January 2019.

Our presenters consist of graduate students and postdoctoral associates who have demonstrated interest in our program by attending a recruiting information session. One or two volunteers sign up for a date to present, which occur monthly at each center, as seen in **Figure 5.2**. Our volunteers originate from a diverse range of STEM departments throughout the university, including chemistry, biology, physics, astronomy, earth science, materials science and engineering, medicine, biomedical engineering, sociology, psychology, and other departments. Volunteers choose a topic of their choice, which can be related to their scientific research or simply of interest to them. Presentation materials focused on a variety of types of science, including brain-machine interfaces, lab-grown meat, antibiotic resistance, animal skin patterns, QLED TVs, climate change, MRIs, and more, again reflecting the broad subject matter studied by the NU volunteers that presented. Since the program's inception in 2017, we have had 54 unique presenters, with 31% of those returning to present more than once.

Our volunteers prepare 15-20 minute talks (typically in, but not limited to, a traditional slide format) with ample time for questions. We train the volunteers to refine the talks to be accessible for senior citizens. To help presenters prepare, we provide a volunteer primer with population-specific considerations along with sample slides from well-received presentations. The primer

consists of several tips that we feel are vital for effective science communication to non-science audiences, described in **Table 5.1**.

Table 5.1. Advice for NU Volunteers.	
Frame the talk around interesting, engaging questions.	Keep in mind that these participants do not regularly attend science talks and may need to be persuaded that your content interests or relates to them. For example, "Why should you care about solar cells?" is more effective than "What are solar cells?"
Keep the presentation relatively broad and non-technical.	Give an overview of the topic and introduce the relevancy of this topic into the participants' lives.
Don't assume prior knowledge.	It is encouraged to define what scientists may perceive as simple concepts, even things like what the periodic table is and how electricity works. Some of the participants may not have formally studied anything science-related since high school 50+ years ago. Never use field-specific jargon.
Give historical context for your field.	Additional historical context and landmark events can help the participants connect more to the topic and your research. It also helps them appreciate the growth of your topic over time, and how far the field may have progressed.
Consider why they should know or care about the topic.	Think about these questions: Can they use it in their lives? Does it help people? Will their kids, grandkids, or future generations be impacted by it? As scientists, we may not test the relevance of your research in our daily lab work-life, but this potential impact is likely why the research is funded and how a lay audience can understand it.
Tie your topic to current news stories.	Many residents follow the news closely and will both understand more complex topics easier and remember the content of a presentation better if they can connect it to current events.
Connect your talk to policy.	Find recent policies, proposed budgets, recently introduced bills, or forth-coming policy changes that are relevant to the presentation. Explain the impact of policy on the field and how the participants can affect a change without endorsing any particular decisions, candidates, or political parties.
Make the presentation interactive.	Are there any props that may help increase understanding? Is there an interactive demonstration that could bring clarity to the narrative? Alternatively, consider creating a presentation that is primarily an interactive demonstration with an underlying message.

Be prepared to answer questions.	Don't expect to have all the answers, especially when they are unrelated to the field, but we as scientists are an advocate for science in general. We need to learn how to step out of our comfort zones and be willing to talk about science outside of our area of expertise. This program should be used as a time to practice and develop these skills.
Be sure to enjoy yourself!	The participants love talking to visitors. Being friendly and honest about your scientific knowledge also will show them that scientists are human, too.

5.3.4 Methods of Program Evaluation

To understand the impact and effectiveness of *SwS* in its aims, we designed and distributed anonymized surveys to participants after every presentation, as shown in **Table 5.2**. First, the surveys were designed to assess the degree of accessibility and communication of the content shared by the presenters. We asked if the presentations were helpful or engaging and increased participants' understanding of science topics. We not only received direct feedback on volunteers' efforts to communicate and engage participants effectively but also learned if presentations increased overall interest in science and willingness to participate in similar programs in the future. Another purpose was to understand the attitudes of participants to scientific research and levels of civic engagement. Although anonymized feedback may lead to more honest feedback,[228] one limitation is that we could not track individual behavioral changes over time. Future studies would benefit from collecting personal information to evaluate specific changes in participants' attitudes towards science and if participation in the program leads to perceived changes in voting behavior.

Table 5.2. Sample survey given to participants at senior centers after presentations.

Questions 1-5 were asked on a 5-point Strongly Disagree-Strongly Agree scale. Questions 6-7 were asked with a Yes-No scale. Question 7a was open-ended.	
1	This program increased my understanding of the presented topic.

2	The presentation on the presented topic was helpful and engaging.
3	The presenters were knowledgeable about the topic(s).
4	Basic science is important and needs to be funded.
5	I am a consistent voter in local, state, and federal elections.
6	Would you be interested in further information on these topics?
7	Would you attend a similar program in the future?
7a	If yes, what scientific topics would you like to see covered?

5.3.5 Outcomes and Feedback

Figure 5.3 shows our program has been largely successful in its aims. Over the course of a year of presentations at the Levy Center (December 2018 – December 2019), the survey feedback (n=202) indicates that 90% of survey respondents agreed that presentations increase their understanding of the topic and 92% indicated that they will return to the program. During the course of the 13 months of the presentations when these data were collected, we enjoyed steady attendance of 7-20 participants per session. Feedback collected from the Covenant Home (n=132) was largely similar to that of the Levy Center indicating the overall generalizability of the program: 78% agreed that the presentations increased their understanding of the topic and 83% reported that they would attend similar programs in the future. While the disparity between levels of agreement

in the two centers may stem from the demographic makeup and cognitive abilities, additional research would directly investigate this relationship.

To further examine the program's reach and its potential impact on voting and science appreciation as specified in the aims, we asked participants about their voting habits and belief in the importance of science funding. While this measure did not explicitly probe the change in these behaviors as a function of the program, it did allow us to understand the opinions of the audience. We found that our participants consistently vote in elections (91% agree), which agrees with the expected voting rate for this age group nationwide. Finally, we found that our participants believe in the importance of science funding (95% agree), which suggests that participants who already

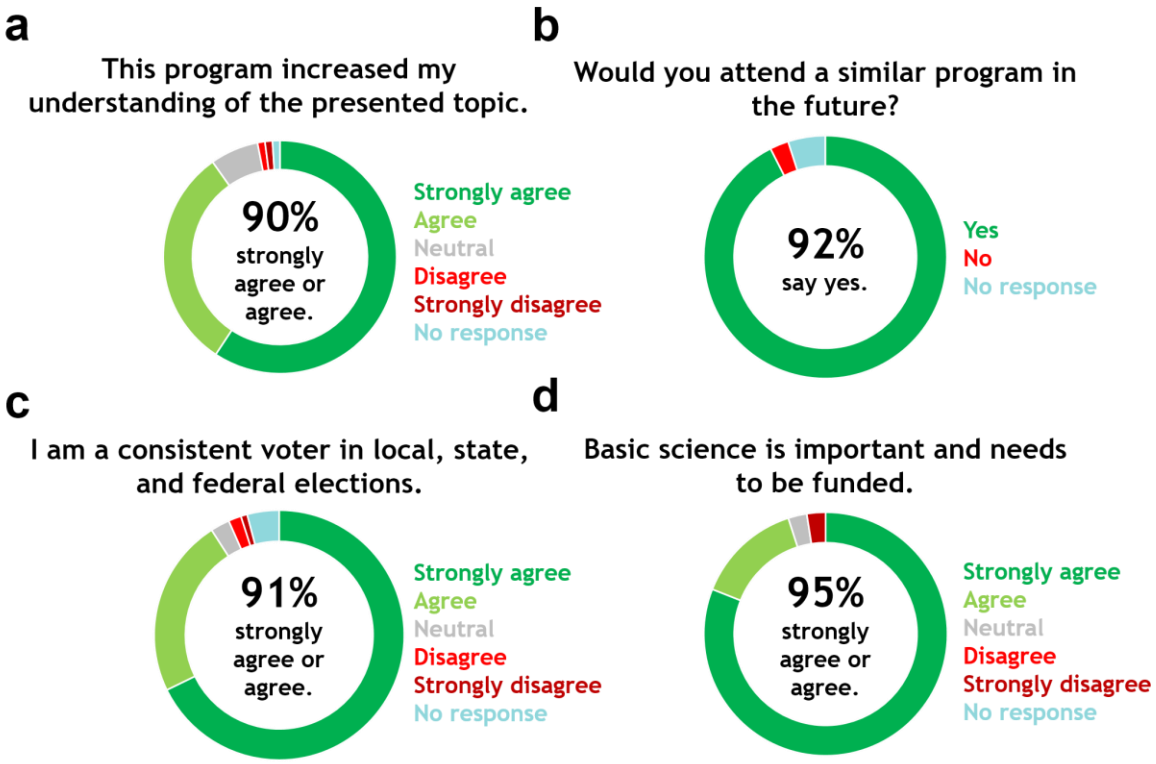

Figure 5.3. Survey feedback from 202 responses collected from December 2018 to December 2019 at the Levy Center.

have interest in science (and therefore positive attitudes about science) may be more likely to attend our sessions. This predisposition is an expected limitation, as our program is an optional event at each center. Future iterations of this program might be interested in evaluating how these results may change in settings where pre-existing attitudes towards science may not be as friendly.

5.3.6 Lessons Learned

In creating *SwS*, we set out to answer the following questions:

1. What are effective ways to engage senior citizens with science outreach?
2. How can senior citizens benefit from science outreach?
3. How will science outreach affect the attitudes towards science and voting habits of senior citizens?

In the early years of *SwS*, we have been most successful at answering Question 1. Along the way, we learned several important lessons about this type of senior citizen-centered STEM outreach throughout its early years of development. Understanding the best way to tailor a talk to a given audience is crucial and framing an argument is key in winning over an audience.[229] In early sessions of our program, we experimented with several formats to understand which method works best. Some early talks tended to be too pedagogical and attempted to cover excessive detailed information. The result was a communication barrier between the presenter and the participants which prevented a productive conversation. Other early presentations tried to borrow aspects from STEM outreach and education designed for children, such as a number of interactive activities that involved mobility and dexterity.[217] We did not initially anticipate these population-specific considerations for an older audience to include in our training and developed an optimal format after several months of trial and error.

We learned that the most useful format for everyone involved was informal talks with a large number of visual aids to reinforce complex concepts. As a result of this change, the participants have been consistently and highly engaged during sessions and have asked many questions throughout presentations. We encourage this type of interaction since it has marked a shift from a pedagogical to conversational program. This type of interaction has led to successful outcomes in established LLIs because it promotes reflective thinking and more engaged learning.[223,225] We are optimistic that this conversational approach of *SwS* will be similarly successful, although further research, as described below, will be needed to evaluate if this format can lead to increased science literacy.

Additionally, we are starting new dialogues and forging new relationships that would not have been formed without *SwS*. Although our content has been primarily tailored to a lay audience level, we found that even participants who may have had expertise in a certain area have been receptive to the content being presented. For example, a participant who was a retired biology professor was eager to contribute his own understanding on talks regarding CRISPR, GMOs, and antibiotics, leading to a productive and useful conversation where both parties learned something new. These talks are learning experiences for the presenters as well, and they often remark that they too have learned how to think about their research from a new angle and answer questions in a clear manner from the comments and unexpected questions that arise during the discussion portion of the session. Frequently, participants asked questions that connected the presentation content to unconventionally-related topics, such as news stories, personal accounts, and other types of science, leading to exciting new discussions. As a result, *SwS* sessions have evolved to become mutually beneficial dialogues for both presenters and participants. One presenter summarized this

sentiment adequately (also seen in **Table 5.3**), explaining, “The prevailing mindset about seniors is that they can only understand so much. But my audience surprised me with so many technical questions and threw around terminology and technology that I had not heard of before. It was a learning experience that went both ways.”

One shortcoming of our program evaluation is that we did not holistically answer Question 2. It is clear that senior citizens have benefited from a self-reported improvement in understanding of scientific topics, but there may be more benefits. As reported in prior LLIs, these types of lectures have the potential to improve cognitive ability, self-esteem, and overall wellbeing.[222,223] It would be interesting to understand if there are other benefits to *SwS* beyond increased appreciation for science. For example, could these lectures be incorporated in a more holistic curriculum or integrated in other LLIs for maximum overall benefit?

Finally, further work will have to be done to rigorously probe Question 3. In this article, we have described the development of a sustainable STEM outreach program in *SwS*. A logical next step would be to use it as a platform to investigate its role on science literacy and voting habits as a science education research project. We might study this by mandating surveys prior to and after presentations to measure a change in scientific understanding. This step could be further supplemented by asking specific questions covered in the topic to obtain a more accurate and non-self-reported way to probe scientific literacy. Although we have currently only collected anonymized feedback, collecting personal information could be used to track the progress of individuals to measure long-term improvements in science literacy. To measure changes in voting behavior, which could be difficult to directly probe, we might ask supplemental questions after an

election to understand if the presentations had any perceived impact on their decision-making process, especially about science-related issues.

With the results and lessons gained from *SwS*, we can put forth several recommendations to guide future STEM outreach programs that seek to focus on older adult populations:

1. Seek community partners with goals that align with program goals, such as established LLIs.
2. Spend the necessary amount of time on training presenters prior to sessions to maximize the potential impact of the content.
3. Make time to chat informally with residents before and after presentations to humanize scientists and build relationships.
4. Foster a dialogue between the presenter and participants by creating a comfortable space for questions and discussion.
5. Seek suggestions for program improvement from both presenters and participants.

5.3.7 Future Outlook

In addition to the ways outlined above to probe the original questions more rigorously, we have other plans to further improve the program moving forward. We plan on partnering with more senior centers and incorporating more medically related talks (which have been heavily requested) by recruiting more presenters from the NU Feinberg School of Medicine. Based on our success establishing this program to multiple locations, we are optimistic that this model can be expanded to other locations, such as public libraries or community centers, to reach a broader audience of voting-age adults. We are also in the process of making presented talks available online so that participants can access this information after the sessions and can continue the conversation about

science elsewhere. These online resources would be accompanied by an optional online version of the survey to further evaluate any learning that occurs beyond our direct presence. A long-term vision for this program is that these conversations expand and proliferate outside of presentation sessions so that participants talk and think critically about science as they encounter it elsewhere in their lives, such as on the news or in the voting booth. We are exploring other ideas to build more actively engaging environments. These formats include disseminating reading guides or case studies to participants beforehand and having participants lead small group-based discussions after presentations.

An additional benefit was that the *SwS* program improved science communication skills of the presenters. Although we did not explicitly measure this improvement during the early development of *SwS*, we have received unsolicited anecdotal feedback from presenters, along with the tendency for presenters to talk and take part in *SwS* multiple times: 31% of our presenters return to the program and give more than one presentation. As a result, we have recently begun to monitor this trend by distributing open-ended surveys to collect self-evaluations from presenters. **Table 5.3** shows some early feedback from presenters from personal experiences with *SwS*.

Table 5.3. Presenter Feedback.
"The prevailing mindset about seniors is that they can only understand so much. But my audience surprised me with so many technical questions and threw around terminology and technology that I had not heard of before. It was a learning experience that went both ways"
"I've been working on outreach for a while now and this definitely reinforced my belief in the importance of disseminating scientific findings to a broader audience."
"SwS has made me realize how important (and difficult!) it is to explain your research in accessible terms and to make the topic exciting/relevant to others. I also feel more confident in my speaking skills!"
"It really showed that sci comm is much more versatile than I generally think--you truly do have to cater it to audiences."
"I realized that outside of classrooms and scientific conferences, it's important to take a step back from detailed explanations and focus more on what research has accomplished and why it is important."

Academic education of graduate and postdoctoral researchers does not always emphasize science presentation skills to a lay audience because research communication to peer scientists in their field is a greater priority. By presenting with *SwS*, volunteers gain valuable science communication skills and experience in how to tailor science talks to people with a wide range of science backgrounds. These tools are urgently important to early-career scientists and engineers so that the network of scientifically-literate, voting-age people continues to grow in the future. The communication skills developed by presenters during *SwS* sessions are likely to help them in future outreach events and in a professional context beyond science outreach.[218]

Finally, we plan to encourage more general feedback about the program to further improve *SwS*. By engaging all participants, including presenters, in shaping the program, we can meet mutual needs and increase its impact on the community. We are hopeful that *SwS* continues on its path of sustainable long-term growth and is viewed by the NU community as a useful learning experience valuable to all STEM researchers and by the broader community as a trustworthy, accessible, and engaging program.

5.4 Chapter Conclusion

In summary, this chapter describes the development, methodology, and analysis of a graduate student-led program to bring STEM outreach to senior citizens, a demographic that is historically overlooked for STEM outreach and the most dedicated voting bloc. Survey results indicate that program participants in *SwS* gain a better understanding of the presented subjects and enjoy coming back to future programs. *SwS* has been successful in its early aims of establishing relationships with senior centers and developing the right format of presentations for this audience,

and it builds a framework for future studies to investigate the long-term effects of this type of programming on attitudes towards science and eventually voting habits.

Chapter 6: Conclusions

Adapted from:

Padgaonkar, S.; Olding, J. N.; Lauhon, L. J.; Hersam, M. C.; Weiss, E. A., *Accounts of Chemical Research*, **2020**, *53* (4), 763-772.

6.1 Dissertation Summary

This dissertation describes the control of the photophysical properties of MDHJs through three different strategies: i) interfacial morphology, ii) responsivity to external stimuli, and iii) use of chemically reactive 2D materials. In Chapter 1, the current state of MDHJ research is assessed, namely primary studies of the interfacial photophysics at the MDHJ interface and early optoelectronic applications of MDHJs in detection, photovoltaics, and catalysis. In Chapter 2, the rate of charge recombination between 0D phthalocyanine (Pc) molecules and 2D MoS_2 is controlled by the orientation of the molecules on the 2D surface. The lifetime of the charge-separated state lasts as long as 70 ns in CuPc/MoS_2 heterojunctions, which is a factor of 17 longer than in H_2Pc/MoS_2 heterojunctions. This long-lived charge separation is attributed to the different orientations of the molecules on the surface of MoS_2; CuPc lies face-on, which facilitates stacking of the CuPc molecules and allows holes to migrate away from the interface, but H_2Pc lies both edge-on and face-on. In Chapter 3, the photoluminescence intensity of CdSe QDs is controlled by using different wavelengths of light to switch the isomer of bound photochromic FFC ligands. UV and visible light switch the FFC between "closed" and "open" isomers, and photo-excited QDs transfer electrons to these different isomers at different rates. The photoluminescence of QDs is reversibly switched by over 80% through at least six illumination cycles. In Chapter 4, a scheme is demonstrated to enable the photosensitization of chemically-reactive BP using a long-range EnT from a self-assembled film of CdSe/ZnS QDs through a protective alumina encapsulation layer. The rate of EnT is dependent on the variable thickness of the alumina encapsulation layer. The EnT dependence on energy donor-acceptor distance scales as $\sim d^{-2.3}$, which is shallower than a predicted scaling of $\sim d^{-3}$ from Förster theory for a 0D donor to 3D acceptor. Electrodynamics simulations posit that this EnT is enables by the interactions of QDs among one another in the self-

assembled film through dipole field scattering, which increases the interaction area of coupling between donor and acceptor.

6.2 Future Directions

MDHJs present a means to obtain superlative performance in optoelectronic applications, such as detectors, photovoltaics, and catalysis. Beyond this short-term opportunity, MDHJs also have the potential to exhibit new and exotic behavior through the combination of different aspects of their nature as nanoscale materials, including quantum confinement and electronic hybridization. Because of their hypersensitivity to surface chemistry due to large surface-to-volume ratios, MDHJs are extremely responsive to small physical changes in themselves and their environment. By leveraging this hypersensitivity, control of the physical parameters in MDHJs can lead to emergent properties that can lead to new optoelectronic applications. This thesis describes projects that control three different physical parameters in MDHJs: interfacial morphology, response to external stimuli, and chemically reactive materials. This section suggests more ways to develop control of these parameters to tune rates of charge and energy transfer and also posits other means to tune physical parameters in order to achieve emergent phenomena in MDHJs: exciton delocalization, spin selectivity, and quantum emission.

6.2.1 Interfacial Morphology

Molecular orientation at mixed-dimensional interfaces affects interfacial exciton dissociation and recombination rates through electronic coupling,[21] and the orientation of components affects interfacial energy transfer rates through relative orientations of the dipole moments of the donor and acceptor, **Figure 6.1a**.[44] While the interactions in these examples are governed by van der Waals forces, covalent linkages to tether 0D materials to 2D materials through molecular bridges

will likely allow for greater control of the molecular orientation, interfacial distance, and excitonic behavior at the heterointerface. Furthermore, certain organic molecules orient in epitaxially specific ways on the surface of 2D materials.[230] This behavior could be further probed by ultrafast scanning tunneling microscopy studies to understand if interfacial excitons emerge at crystallographically pristine interfaces and if rates and yields of charge transfer depend on this epitaxy. For nanocrystals, one major challenge toward achieving pristine interfaces is the polydispersity of as-synthesized low-dimensional materials, which limit carrier transport, but improvements in synthetic schemes to improve monodispersity may provide a solution.[231]

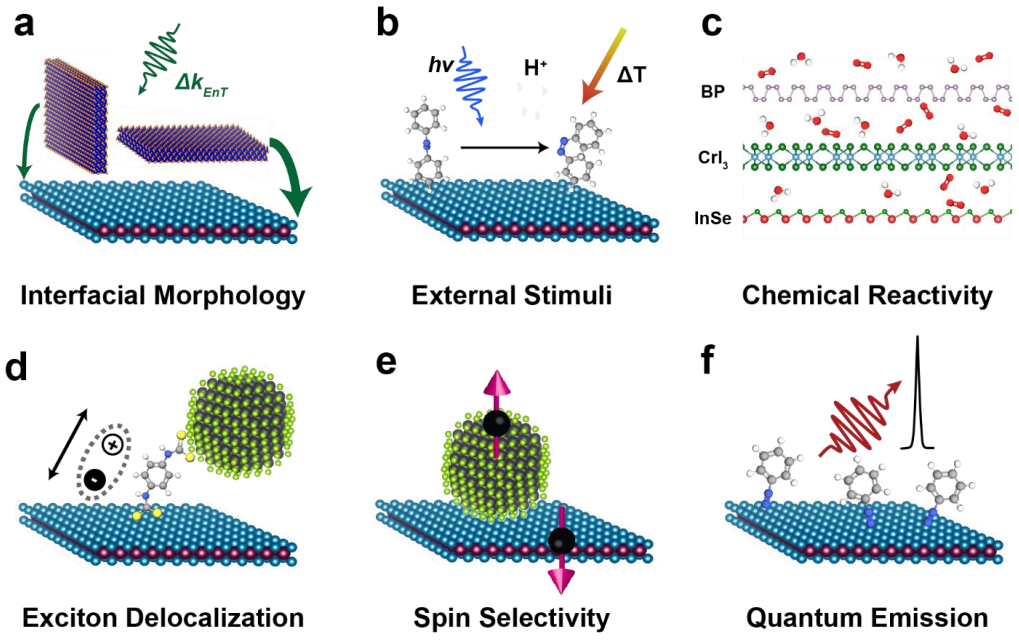

Figure 6.1. Outlook for MDHJs. **(a)** Interfacial morphological effects on exciton dynamics by controlling orientation and interlayers. **(b)** Synthetic tunability of the 0D component to be responsive to external stimuli. **(c)** Exploitation and suppression of ambient reactivity in 2D materials. **(d)** Mechanistic studies of exciton delocalization as a function of chemically modified interlayers. **(e)** Spin selectivity of carrier transfer across heterointerfaces. **(f)** Single photon emission through chemical control of defect states.

6.2.2 Response to External Stimuli

The components of MDHJs are particularly sensitive to external stimuli because the thin 2D substrate incompletely absorbs light and can be readily modulated by gate-induced electric fields, thus presenting opportunities for dynamically controlling the behavior of MDHJs. This control could occur slowly relative to the electronic processes in the junction, in which case the application is likely to be optical or electrical switching. On the other hand, if the switching occurs on the same timescale as the electronic processes in the heterojunction, the resulting non-equilibrium system could display emergent behaviors. The most obvious "knob" to turn within the heterojunction is the set of organic molecules that serve as either 0D materials or interfacial layers, as the conformations and degrees of conjugation of these molecules can be designed to be responsive to external stimuli such as light, temperature, and pH, **Figure 6.1b**. For instance, pH-responsive polymers have been used to encapsulate MoS_2 nanoparticles for sensing applications based on pH changes enabled by energy transfer since MoS_2 acts as an efficient exciton sink.[232] In another example, photoswitchable molecules such as diarylethenes that change their optical absorbance and orbital energy levels upon photoexcitation could drive changes in the charge transport behavior of 2D materials, thereby presenting opportunities for optical memory systems.[233] Use of molecules that switch on faster timescales through, for example, electrocyclization, could allow the properties of 2D materials to be tuned both reversibly and dynamically, allowing light to be used in an analogous manner to the electric fields that are commonly used to gate 2D materials.

6.2.3 Chemically Reactive 2D Materials

While TMDCs, namely MoS_2, have been the main focus of early studies, the potential of many other 2D semiconductors remains untapped, particularly those that are ambient-reactive such as black phosphorus (BP), chromium iodide (CrI_3), and indium selenide (InSe), **Figure 6.1c**. Towards this end, the long-term ambient stabilization of chemically reactive 2D materials has been demonstrated using alumina encapsulation through atomic layer deposition and chemical passivation with covalent adsorbates such as aryl diazonium radicals.[34–36] Because conventional approaches to form heterostructures with solution-processed materials such as spin-coating or layer-by-layer techniques are not likely to be compatible with ambient-reactive materials, one unfulfilled opportunity lies in the development of methods to deposit 0D or 1D materials to form MDHJ architectures. Importantly, long-range energy transfer (on the scale of tens of nm, which is an order of magnitude longer than energy transfer in 0D-0D systems) has been observed with several ambient-stable 2D materials as acceptors,[39,40] so sensitization by a 0D or 1D nanostructure or molecule can still occur through an encapsulation layer. By expanding the range of low-dimensional materials within MDHJs, new possibilities for both fundamental studies and technological applications can be anticipated in this fast-growing research area.

6.2.4 Exciton Delocalization

Organic molecules can be used to tune the quantum confinement of low-dimensional semiconductors. One striking example is phenyldithiocarbamate (PTC) and its derivatives. Post-synthetic treatment of QDs with PTC reduces the optical bandgap of metal-chalcogenide QDs by up to 1 eV without changing the physical size of the QDs[234] through mixing of the frontier orbitals of PTC with the delocalized states of the QD valence band. This delocalization results in sub-

picosecond hole extraction by hole acceptors linked to QDs with PTC, [235] and enhanced exciton transport in QD films.[236] Ligands of this type could be used to increase the electronic coupling at 0D/2D interfaces and, depending on the relative energy levels of the linker and the bands of the semiconductor materials, selectively enhance either hole or electron transport in-plane or across the heterointerface, **Figure 6.1d**. Similarly, 2D materials can be functionalized with exciton delocalizing ligands during colloidal synthesis, delocalizing molecules as surfactants during liquid phase exfoliation, or chemical treatment after fabrication of ultrathin films. Another option for selectively controlling confinement of either the electron or hole within a 0D material is the use of a core-shell architecture where the core and shell have a type-II heterojunction configuration, a technique that has been used extensively to stabilize QDs.[237]

6.2.5 Spin Selectivity

MDHJs also provide opportunities for manipulating the electron spin degree of freedom. A magnetically active overlayer/adlayer/encapsulant would interact with the entirety of an atomically thin monolayer 2D material, potentially mixing spin states and inducing a strong optomagnetic response that could be reconfigured with external magnetic fields. In this context, chiral molecules could serve as spin-selective interlayers for charge transfer, **Figure 6.1e**,[238] as has been demonstrated in QD-QD assemblies.[239] Spin-selective carrier transfer within a MDHJ would enable the creation of spin polarization in the acceptor material following unpolarized electrical or optical injection into the donor material. Chiral effects could also be incorporated beyond molecular systems, such as the case of chiral TMDC quantum dots, which have high potential as spin filters in spintronic applications.[240] Other 2D materials that have layer-dependent magnetic ordering, such as CrI_3, could also be used in this context.[37] These electrically tunable ferromagnets

could potentially be utilized to control spin-sensitive photophysical behavior within adsorbed chromophores, such as intersystem crossing rates.

6.2.6 Quantum Emission

Finally, controlling excitonic confinement to produce single-photon (or quantum) emission from localized states is also of interest for quantum information sciences.[241] Wide-bandgap 2D materials, such as hexagonal boron nitride, have been physically altered to engineer strain in controlled locations for single-photon defect emission.[242] In addition, covalent functionalization of MoS_2 with organohalides leads to lower-energy defect emission,[243] and similar treatments may alter the surfaces of 2D materials to create chemically tailored quantum emitters, **Figure 6.1f**, that are analogous to the tunable emission that has been achieved with carbon nanotubes.[244] Low-dimensional materials are particularly well suited for this application because the proximity of defects to the surface makes them chemically addressable and increases the yield of photon extraction.

References

(1) Scholes, G. D.; Rumbles, G. Excitons in Nanoscale Systems. *Nat. Mater.* **2006**, *5*, 683–696. https://doi.org/10.1038/nmat1710.

(2) Brennan, K. F. *The Physics of Semiconductors*; Cambridge University Press, 1999. https://doi.org/10.1017/CBO9781139164214.

(3) Harris, R. D.; Bettis Homan, S.; Kodaimati, M.; He, C.; Nepomnyashchii, A. B.; Swenson, N. K.; Lian, S.; Calzada, R.; Weiss, E. A. Electronic Processes within Quantum Dot-Molecule Complexes. *Chem. Rev.* **2016**, *116* (21), 12865–12919. https://doi.org/10.1021/acs.chemrev.6b00102.

(4) Ostroverkhova, O. Organic Optoelectronic Materials: Mechanisms and Applications. *Chem. Rev.* **2016**, *116* (22), 13279–13412. https://doi.org/10.1021/acs.chemrev.6b00127.

(5) Dresselhaus, M. S.; Dresselhaus, G.; Saito, R.; Jorio, A. Exciton Photophysics of Carbon Nanotubes. *Annu. Rev. Phys. Chem.* **2007**, *58* (1), 719–747. https://doi.org/10.1146/annurev.physchem.58.032806.104628.

(6) Tamai, Y.; Ohkita, H.; Benten, H.; Ito, S. Exciton Diffusion in Conjugated Polymers: From Fundamental Understanding to Improvement in Photovoltaic Conversion Efficiency. *J. Phys. Chem. Lett.* **2015**, *6* (17), 3417–3428. https://doi.org/10.1021/acs.jpclett.5b01147.

(7) Yuan, L.; Wang, T.; Zhu, T.; Zhou, M.; Huang, L. Exciton Dynamics, Transport, and Annihilation in Atomically Thin Two-Dimensional Semiconductors. *J. Phys. Chem. Lett.* **2017**, *8* (14), 3371–3379. https://doi.org/10.1021/acs.jpclett.7b00885.

(8) Ceballos, F.; Zhao, H. Ultrafast Laser Spectroscopy of Two-Dimensional Materials Beyond Graphene. *Adv. Funct. Mater.* **2017**, *27* (19), 1604509. https://doi.org/10.1002/adfm.201604509.

(9) Jariwala, D.; Marks, T. J.; Hersam, M. C. Mixed-Dimensional van Der Waals Heterostructures. *Nat. Mater.* **2017**, *16* (2), 170–181. https://doi.org/10.1038/nmat4703.

(10) Kufer, D.; Nikitskiy, I.; Lasanta, T.; Navickaite, G.; Koppens, F. H. L.; Konstantatos, G. Hybrid 2D-0D MoS_2-PbS Quantum Dot Photodetectors. *Adv. Mater.* **2015**, *27* (1), 176–180. https://doi.org/10.1002/adma.201402471.

(11) Kufer, D.; Lasanta, T.; Bernechea, M.; Koppens, F. H. L.; Konstantatos, G. Interface Engineering in Hybrid Quantum Dot-2D Phototransistors. *ACS Photonics* **2016**, *3* (7), 1324–1330. https://doi.org/10.1021/acsphotonics.6b00299.

(12) Adinolfi, V.; Kramer, I. J.; Labelle, A. J.; Sutherland, B. R.; Hoogland, S.; Sargent, E. H. Photojunction Field-Effect Transistor Based on a Colloidal Quantum Dot Absorber Channel Layer. *ACS Nano* **2015**, *9* (1), 356–362. https://doi.org/10.1021/nn5053537.

(13) Zhu, X.; Monahan, N. R.; Gong, Z.; Zhu, H.; Williams, K. W.; Nelson, C. A. Charge Transfer Excitons at van Der Waals Interfaces. *J. Am. Chem. Soc.* **2015**, *137* (26), 8313–8320. https://doi.org/10.1021/jacs.5b03141.

(14) Shastry, T. A.; Balla, I.; Bergeron, H.; Amsterdam, S. H.; Marks, T. J.; Hersam, M. C. Mutual Photoluminescence Quenching and Photovoltaic Effect in Large-Area Single-Layer MoS_2-Polymer Heterojunctions. *ACS Nano* **2016**, *10* (11), 10573–10579. https://doi.org/10.1021/acsnano.6b06592.

(15) Zhu, T.; Yuan, L.; Zhao, Y.; Zhou, M.; Wan, Y.; Mei, J.; Huang, L. Highly Mobile Charge-Transfer Excitons in Two-Dimensional WS_2/Tetracene Heterostructures. *Sci. Adv.* **2018**, *4* (1), eaao3104. https://doi.org/10.1126/sciadv.aao3104.

(16) Amsterdam, S. H.; Stanev, T. K.; Zhou, Q.; Lou, A. J. T.; Bergeron, H.; Darancet, P.; Hersam, M. C.; Stern, N. P.; Marks, T. J. Electronic Coupling in Metallophthalocyanine-Transition Metal Dichalcogenide Mixed-Dimensional Heterojunctions. *ACS Nano* **2019**, *13* (4), 4183–4190. https://doi.org/10.1021/acsnano.8b09166.

(17) Homan, S. B.; Sangwan, V. K.; Balla, I.; Bergeron, H.; Weiss, E. A.; Hersam, M. C. Ultrafast Exciton Dissociation and Long-Lived Charge Separation in a Photovoltaic Pentacene-MoS_2 van Der Waals Heterojunction. *Nano Lett.* **2017**, *17* (1), 164–169. https://doi.org/10.1021/acs.nanolett.6b03704.

(18) Petoukhoff, C. E.; Krishna, M. B. M.; Voiry, D.; Bozkurt, I.; Deckoff-Jones, S.; Chhowalla, M.; O'Carroll, D. M.; Dani, K. M. Ultrafast Charge Transfer and Enhanced Absorption in MoS_2-Organic van Der Waals Heterojunctions Using Plasmonic Metasurfaces. *ACS Nano* **2016**, *10* (11), 9899–9908. https://doi.org/10.1021/acsnano.6b03414.

(19) Boulesbaa, A.; Wang, K.; Mahjouri-Samani, M.; Tian, M.; Puretzky, A. A.; Ivanov, I.; Rouleau, C. M.; Xiao, K.; Sumpter, B. G.; Geohegan, D. B. Ultrafast Charge Transfer and Hybrid Exciton Formation in 2D/0D Heterostructures. *J. Am. Chem. Soc.* **2016**, *138* (44), 14713–14719. https://doi.org/10.1021/jacs.6b08883.

(20) Zhong, C.; Sangwan, V. K.; Wang, C.; Bergeron, H.; Hersam, M. C.; Weiss, E. A. Mechanisms of Ultrafast Charge Separation in a PTB7/Monolayer MoS_2 van Der Waals Heterojunction. *J. Phys. Chem. Lett.* **2018**, *9* (10), 2484–2491. https://doi.org/10.1021/acs.jpclett.8b00628.

(21) Padgaonkar, S.; Amsterdam, S. H.; Bergeron, H.; Su, K.; Marks, T. J.; Hersam, M. C.; Weiss, E. A. Molecular-Orientation-Dependent Interfacial Charge Transfer in Phthalocyanine/MoS_2 Mixed-Dimensional Heterojunctions. *J. Phys. Chem. C* **2019**, *123* (21), 13337–13343. https://doi.org/10.1021/acs.jpcc.9b04063.

(22) Sulas-Kern, D. B.; Zhang, H.; Li, Z.; Blackburn, J. L. Microsecond Charge Separation at Heterojunctions between Transition Metal Dichalcogenide Monolayers and Single-Walled Carbon Nanotubes. *Mater. Horiz.* **2019**, *6* (10), 2103–2111. https://doi.org/10.1039/c9mh00954j.

(23) Kafle, T. R.; Kattel, B.; Yao, P.; Zereshki, P.; Zhao, H.; Chan, W. L. Effect of the Interfacial Energy Landscape on Photoinduced Charge Generation at the ZnPc/MoS_2 Interface. *J. Am. Chem. Soc.* **2019**, *141* (28), 11328–11336. https://doi.org/10.1021/jacs.9b05893.

(24) Kafle, T. R.; Kattel, B.; Lane, S. D.; Wang, T.; Zhao, H.; Chan, W. L. Charge Transfer Exciton and Spin Flipping at Organic-Transition-Metal Dichalcogenide Interfaces. *ACS Nano* **2017**, *11* (10), 10184–10192. https://doi.org/10.1021/acsnano.7b04751.

(25) Henning, A.; Sangwan, V. K.; Bergeron, H.; Balla, I.; Sun, Z.; Hersam, M. C.; Lauhon, L. J. Charge Separation at Mixed-Dimensional Single and Multilayer MoS_2/Silicon Nanowire Heterojunctions. *ACS Appl. Mater. Interfaces* **2018**, *10* (19), 16760–16767. https://doi.org/10.1021/acsami.8b03133.

(26) Li, M.; Chen, J. S.; Routh, P. K.; Zahl, P.; Nam, C. Y.; Cotlet, M. Distinct Optoelectronic Signatures for Charge Transfer and Energy Transfer in Quantum Dot–MoS_2 Hybrid Photodetectors Revealed by Photocurrent Imaging Microscopy. *Adv. Funct. Mater.* **2018**, *28* (29), 1707558. https://doi.org/10.1002/adfm.201707558.

(27) Jin, C.; Ma, E. Y.; Karni, O.; Regan, E. C.; Wang, F.; Heinz, T. F. Ultrafast Dynamics in van Der Waals Heterostructures. *Nat. Nanotechnol.* **2018**, *13* (11), 994–1003. https://doi.org/10.1038/s41565-018-0298-5.

(28) Howard, I. A.; Mauer, R.; Meister, M.; Laquai, F. Effect of Morphology on Ultrafast Free Carrier Generation in Polythiophene:Fullerene Organic Solar Cells. *J. Am. Chem. Soc.* **2010**, *132* (42), 14866–14876. https://doi.org/10.1021/ja105260d.

(29) Liu, X. Y.; Chen, W. K.; Fang, W. H.; Cui, G. Nonadiabatic Dynamics Simulations Reveal Distinct Effects of the Thickness of PTB7 on Interfacial Electron and Hole Transfer Dynamics in PTB7@MoS_2 Heterostructures. *J. Phys. Chem. Lett.* **2019**, *10* (11), 2949–2956. https://doi.org/10.1021/acs.jpclett.9b01066.

(30) Liu, X. Y.; Xie, X. Y.; Fang, W. H.; Cui, G. Theoretical Insights into Interfacial Electron Transfer between Zinc Phthalocyanine and Molybdenum Disulfide. *J. Phys. Chem. A* **2018**, *122* (50), 9587–9596. https://doi.org/10.1021/acs.jpca.8b07816.

(31) Olding, J. N.; Henning, A.; Dong, J. T.; Zhou, Q.; Moody, M. J.; Smeets, P. J. M.; Darancet, P.; Weiss, E. A.; Lauhon, L. J. Charge Separation in Epitaxial SnS/MoS2 Vertical Heterojunctions Grown by Lowerature Pulsed MOCVD. *ACS Appl. Mater. Interfaces* **2019**, *11* (43), 40543–40550. https://doi.org/10.1021/acsami.9b14412.

(32) Brumberg, A.; Diroll, B. T.; Nedelcu, G.; Sykes, M. E.; Liu, Y.; Harvey, S. M.; Wasielewski, M. R.; Kovalenko, M. V.; Schaller, R. D. Material Dimensionality Effects on Electron Transfer Rates between $CsPbBr_3$ and CdSe Nanoparticles. *Nano Lett.* **2018**, *18* (8), 4771–4776. https://doi.org/10.1021/acs.nanolett.8b01238.

(33) Ryder, C. R.; Wood, J. D.; Wells, S. A.; Hersam, M. C. Chemically Tailoring Semiconducting Two-Dimensional Transition Metal Dichalcogenides and Black Phosphorus. *ACS Nano* **2016**, *10* (4), 3900–3917. https://doi.org/10.1021/acsnano.6b01091.

(34) Ryder, C. R.; Wood, J. D.; Wells, S. A.; Yang, Y.; Jariwala, D.; Marks, T. J.; Schatz, G. C.; Hersam, M. C. Covalent Functionalization and Passivation of Exfoliated Black Phosphorus via Aryl Diazonium Chemistry. *Nat. Chem.* **2016**, *8* (6), 597–602. https://doi.org/10.1038/nchem.2505.

(35) Wood, J. D.; Wells, S. A.; Jariwala, D.; Chen, K. S.; Cho, E.; Sangwan, V. K.; Liu, X.; Lauhon, L. J.; Marks, T. J.; Hersam, M. C. Effective Passivation of Exfoliated Black Phosphorus Transistors against Ambient Degradation. *Nano Lett.* **2014**, *14* (12), 6964–6970. https://doi.org/10.1021/nl5032293.

(36) Wells, S. A.; Henning, A.; Gish, J. T.; Sangwan, V. K.; Lauhon, L. J.; Hersam, M. C. Suppressing Ambient Degradation of Exfoliated InSe Nanosheet Devices via Seeded Atomic Layer Deposition Encapsulation. *Nano Lett.* **2018**, *18* (12), 7876–7882. https://doi.org/10.1021/acs.nanolett.8b03689.

(37) Jiang, S.; Li, L.; Wang, Z.; Mak, K. F.; Shan, J. Controlling Magnetism in 2D CrI3 by Electrostatic Doping. *Nat. Nanotechnol.* **2018**, *13* (7), 549–553. https://doi.org/10.1038/s41565-018-0135-x.

(38) Swathi, R. S.; Sebastian, K. L. Long Range Resonance Energy Transfer from a Dye Molecule to Graphene Has (Distance)$^{-4}$ Dependence. *J. Chem. Phys.* **2009**, *130* (8), 086101. https://doi.org/10.1063/1.3077292.

(39) Taghipour, N.; Martinez, P. L. H.; Ozden, A.; Olutas, M.; Dede, D.; Gungor, K.; Erdem, O.; Perkgoz, N. K.; Demir, H. V. Near-Unity Efficiency Energy Transfer from Colloidal Semiconductor Quantum Wells of CdSe/CdS Nanoplatelets to a Monolayer of MoS_2. *ACS Nano* **2018**, *12* (8), 8547–8554. https://doi.org/10.1021/acsnano.8b04119.

(40) Raja, A.; Montoya-Castillo, A.; Zultak, J.; Zhang, X. X.; Ye, Z.; Roquelet, C.; Chenet, D. A.; Van Der Zande, A. M.; Huang, P.; Jockusch, S.; Hone, J.; Reichman, D. R.; Brus, L. E.; Heinz, T. F. Energy Transfer from Quantum Dots to Graphene and MoS_2: The Role of Absorption and Screening in Two-Dimensional Materials. *Nano Lett.* **2016**, *16* (4), 2328–2333. https://doi.org/10.1021/acs.nanolett.5b05012.

(41) Prins, F.; Goodman, A. J.; Tisdale, W. A. Reduced Dielectric Screening and Enhanced Energy Transfer in Single- and Few-Layer MoS_2. *Nano Lett.* **2014**, *14* (11), 6087–6091. https://doi.org/10.1021/nl5019386.

(42) Prasai, D.; Klots, A. R.; Newaz, A. K. M.; Niezgoda, J. S.; Orfield, N. J.; Escobar, C. A.; Wynn, A.; Efimov, A.; Jennings, G. K.; Rosenthal, S. J.; Bolotin, K. I. Electrical Control of Near-Field Energy Transfer between Quantum Dots and Two-Dimensional Semiconductors. *Nano Lett.* **2015**, *15* (7), 4374–4380. https://doi.org/10.1021/acs.nanolett.5b00514.

(43) Lee, J.; Bao, W.; Ju, L.; Schuck, P. J.; Wang, F.; Weber-Bargioni, A. Switching Individual Quantum Dot Emission through Electrically Controlling Resonant Energy Transfer to Graphene. *Nano Lett.* **2014**, *14* (12), 7115–7119. https://doi.org/10.1021/nl503587z.

(44) Erdem, O.; Gungor, K.; Guzelturk, B.; Tanriover, I.; Sak, M.; Olutas, M.; Dede, D.; Kelestemur, Y.; Demir, H. V. Orientation-Controlled Nonradiative Energy Transfer to Colloidal Nanoplatelets: Engineering Dipole Orientation Factor. *Nano Lett.* **2019**, *19* (7), 4297–4305. https://doi.org/10.1021/acs.nanolett.9b00681.

(45) Konstantatos, G. Current Status and Technological Prospect of Photodetectors Based on Two-Dimensional Materials. *Nat. Commun.* **2018**, *9* (1), 5266. https://doi.org/10.1038/s41467-018-07643-7.

(46) Schuler, S.; Schall, D.; Neumaier, D.; Dobusch, L.; Bethge, O.; Schwarz, B.; Krall, M.; Mueller, T. Controlled Generation of a P-n Junction in a Waveguide Integrated Graphene Photodetector. *Nano Lett.* **2016**, *16* (11), 7107–7112. https://doi.org/10.1021/acs.nanolett.6b03374.

(47) Konstantatos, G.; Badioli, M.; Gaudreau, L.; Osmond, J.; Bernechea, M.; De Arquer, F. P. G.; Gatti, F.; Koppens, F. H. L. Hybrid Graphene-Quantum Dot Phototransistors with Ultrahigh Gain. *Nat. Nanotechnol.* **2012**, *7* (6), 363–368. https://doi.org/10.1038/nnano.2012.60.

(48) Adinolfi, V.; Sargent, E. H. Photovoltage Field-Effect Transistors. *Nature* **2017**, *542* (7641), 324–327. https://doi.org/10.1038/nature21050.

(49) Jariwala, D.; Davoyan, A. R.; Wong, J.; Atwater, H. A. Van Der Waals Materials for Atomically-Thin Photovoltaics: Promise and Outlook. *ACS Photonics* **2017**, *4* (12), 2962–2970. https://doi.org/10.1021/acsphotonics.7b01103.

(50) Liu, X.; Balla, I.; Sangwan, V. K.; Usta, H.; Facchetti, A.; Marks, T. J.; Hersam, M. C. Ultrahigh Vacuum Self-Assembly of Rotationally Commensurate C_8-BTBT/MoS_2/Graphene Mixed-Dimensional Heterostructures. *Chem. Mater.* **2019**, *31* (5), 1761–1766. https://doi.org/10.1021/acs.chemmater.8b05348.

(51) Zong, X.; Yan, H.; Wu, G.; Ma, G.; Wen, F.; Wang, L.; Li, C. Enhancement of Photocatalytic H_2 Evolution on CdS by Loading MoS_2 as Cocatalyst under Visible Light Irradiation. *J. Am. Chem. Soc.* **2008**, *130* (23), 7176–7177. https://doi.org/10.1021/ja8007825.

(52) Li, Q.; Zhao, F.; Qu, C.; Shang, Q.; Xu, Z.; Yu, L.; McBride, J. R.; Lian, T. Two-Dimensional Morphology Enhances Light-Driven H_2 Generation Efficiency in CdS Nanoplatelet-Pt Heterostructures. *J. Am. Chem. Soc.* **2018**, *140* (37), 11726–11734. https://doi.org/10.1021/jacs.8b06100.

(53) Jiang, Y.; Wang, C.; Rogers, C. R.; Kodaimati, M. S.; Weiss, E. A. Regio- and Diastereoselective Intermolecular [2+2] Cycloadditions Photocatalysed by Quantum Dots. *Nat. Chem.* **2019**, *11*, 1034–1040. https://doi.org/10.1038/s41557-019-0344-4.

(54) Kodaimati, M. S.; Lian, S.; Schatz, G. C.; Weiss, E. A. Energy Transfer-Enhanced Photocatalytic Reduction of Protons within Quantum Dot Light-Harvesting–Catalyst Assemblies. *Proc. Natl. Acad. Sci. U. S. A.* **2018**, *115* (33), 8290–8295. https://doi.org/10.1073/pnas.1805625115.

(55) Zhou, Q.; Cho, Y.; Yang, S.; Weiss, E. A.; Berkelbach, T. C.; Darancet, P. Large Band Edge Tunability in Colloidal Nanoplatelets. *Nano Lett.* **2019**. https://doi.org/10.1021/acs.nanolett.9b02645.

(56) Wang, Q. H.; Kalantar-Zadeh, K.; Kis, A.; Coleman, J. N.; Strano, M. S. Electronics and Optoelectronics of Two-Dimensional Transition Metal Dichalcogenides. *Nat. Nanotechnol.* **2012**, *7* (11), 699–712. https://doi.org/10.1038/nnano.2012.193.

(57) Bhimanapati, G. R.; Lin, Z.; Meunier, V.; Jung, Y.; Cha, J.; Das, S.; Xiao, D.; Son, Y.; Strano, M. S.; Cooper, V. R.; Liang, L.; Louie, S. G.; Ringe, E.; Zhou, W.; Kim, S. S.; Naik, R. R.; Sumpter, B. G.; Terrones, H.; Xia, F.; Wang, Y.; Zhu, J.; Akinwande, D.; Alem, N.; Schuller, J. A.; Schaak, R. E.; Terrones, M.; Robinson, J. A. Recent Advances in Two-Dimensional Materials beyond Graphene. *ACS Nano* **2015**, *9* (12), 11509–11539. https://doi.org/10.1021/acsnano.5b05556.

(58) Jariwala, D.; Howell, S. L.; Chen, K. S.; Kang, J.; Sangwan, V. K.; Filippone, S. A.; Turrisi, R.; Marks, T. J.; Lauhon, L. J.; Hersam, M. C. Hybrid, Gate-Tunable, van Der Waals p-n Heterojunctions from Pentacene and MoS2. *Nano Lett.* **2016**, *16* (1), 497–503. https://doi.org/10.1021/acs.nanolett.5b04141.

(59) Shastry, T. A.; Balla, I.; Bergeron, H.; Amsterdam, S. H.; Marks, T. J.; Hersam, M. C. Mutual Photoluminescence Quenching and Photovoltaic Effect in Large-Area Single-Layer MoS2-Polymer Heterojunctions. *ACS Nano* **2016**, *10* (11), 10573–10579. https://doi.org/10.1021/acsnano.6b06592.

(60) Homan, S. B.; Sangwan, V. K.; Balla, I.; Bergeron, H.; Weiss, E. A.; Hersam, M. C. Ultrafast Exciton Dissociation and Long-Lived Charge Separation in a Photovoltaic Pentacene-MoS2 van Der Waals Heterojunction. *Nano Lett.* **2017**, *17* (1), 164–169. https://doi.org/10.1021/acs.nanolett.6b03704.

(61) Zhong, C.; Sangwan, V. K.; Wang, C.; Bergeron, H.; Hersam, M. C.; Weiss, E. A. [ASAP] Mechanisms of Ultrafast Charge Separation in a PTB7/Monolayer MoS2 van Der Waals Heterojunction. *J. Phys. Chem. Lett.* **2018**, *9*, 2484–2491. https://doi.org/10.1021/acs.jpclett.8b00628.

(62) Jariwala, D.; Sangwan, V. K.; Wu, C.-C.; Prabhumirashi, P. L.; Geier, M. L.; Marks, T. J.; Lauhon, L. J.; Hersam, M. C. Gate-Tunable Carbon Nanotube-MoS2 Heterojunction p-n Diode. *Proc. Natl. Acad. Sci.* **2013**, *110* (45), 18076–18080. https://doi.org/10.1073/pnas.1317226110.

(63) Huang, Y.; Zhuge, F.; Hou, J.; Lv, L.; Luo, P.; Zhou, N.; Gan, L.; Zhai, T. Van Der Waals Coupled Organic Molecules with Monolayer MoS 2 for Fast Response Photodetectors with Gate-Tunable Responsivity. *ACS Nano* **2018**, *12* (4), 4062–4073. https://doi.org/10.1021/acsnano.8b02380.

(64) Konstantatos, G.; Badioli, M.; Gaudreau, L.; Osmond, J.; Bernechea, M.; de Arquer, F. P. G.; Gatti, F.; Koppens, F. H. L. Hybrid Graphene–Quantum Dot Phototransistors with Ultrahigh Gain. *Nat. Nanotechnol.* **2012**, *7* (6), 363–368. https://doi.org/10.1038/nnano.2012.60.

(65) Kufer, D.; Nikitskiy, I.; Lasanta, T.; Navickaite, G.; Koppens, F. H. L.; Konstantatos, G. Hybrid 2D-0D MoS2 -PbS Quantum Dot Photodetectors. *Adv. Mater. Deerfield Beach Fla* **2015**, *27* (1), 176–180. https://doi.org/10.1002/adma.201402471.

(66) Jariwala, D.; Marks, T. J.; Hersam, M. C. Mixed-Dimensional van Der Waals Heterostructures. *Nat. Mater.* **2016**, *16* (2), 170–181. https://doi.org/10.1038/nmat4703.

(67) Kafle, T. R.; Kattel, B.; Lane, S. D.; Wang, T.; Zhao, H.; Chan, W. L. Charge Transfer Exciton and Spin Flipping at Organic-Transition-Metal Dichalcogenide Interfaces. *ACS Nano* **2017**, *11* (10), 10184–10192. https://doi.org/10.1021/acsnano.7b04751.

(68) Petoukhoff, C. E.; Krishna, M. B. M.; Voiry, D.; Bozkurt, I.; Deckoff-Jones, S.; Chhowalla, M.; O'Carroll, D. M.; Dani, K. M. Ultrafast Charge Transfer and Enhanced Absorption in MoS2-Organic van Der Waals Heterojunctions Using Plasmonic Metasurfaces. *ACS Nano* **2016**, *10* (11), 9899–9908. https://doi.org/10.1021/acsnano.6b03414.

(69) Zhu, T.; Yuan, L.; Zhao, Y.; Zhou, M.; Wan, Y.; Mei, J.; Huang, L. Highly Mobile Charge-Transfer Excitons in Two-Dimensional WS2/Tetracene Heterostructures. *Sci. Adv.* **2018**, *4* (1), eaao3104. https://doi.org/10.1126/sciadv.aao3104.

(70) Amsterdam, S. H.; Stanev, T. K.; Zhou, Q.; Lou, A. J.-T.; Bergeron, H.; Darancet, P.; Hersam, M. C.; Stern, N. P.; Marks, T. J. Electronic Coupling in Metallophthalocyanine–Transition Metal Dichalcogenide Mixed-Dimensional Heterojunctions. *ACS Nano* **2019**, *In press*, acsnano.8b09166. https://doi.org/10.1021/acsnano.8b09166.

(71) Clark, G.; Aivazian, G.; Rivera, P.; Mandrus, D. G.; Yao, W.; Schaibley, J. R.; Ross, J. S.; Yan, J.; Seyler, K.; Ghimire, N. J.; Wu, S.; Klement, P.; Jones, A. M.; Xu, X. Observation of Long-Lived Interlayer Excitons in Monolayer MoSe2–WSe2 Heterostructures. *Nat. Commun.* **2015**, *6* (1). https://doi.org/10.1038/ncomms7242.

(72) Ceballos, F.; Bellus, M. Z.; Chiu, H. Y.; Zhao, H. Ultrafast Charge Separation and Indirect Exciton Formation in a MoS2-MoSe2van Der Waals Heterostructure. *ACS Nano* **2014**, *8* (12), 12717–12724. https://doi.org/10.1021/nn505736z.

(73) Park, J. H.; Sanne, A.; Guo, Y.; Amani, M.; Zhang, K.; Movva, H. C. P.; Robinson, J. A.; Javey, A.; Robertson, J.; Banerjee, S. K.; Kummel, A. C. Defect Passivation of Transition Metal Dichalcogenides via a Charge Transfer van Der Waals Interface. *Sci. Adv.* **2017**, *3* (10). https://doi.org/10.1126/sciadv.1701661.

(74) Benjamin, C. J.; Zhang, S.; Chen, Z. Controlled Doping of Transition Metal Dichalcogenides by Metal Work Function Tuning in Phthalocyanine Compounds. *Nanoscale* **2018**, *10* (11), 5148–5153. https://doi.org/10.1039/c7nr08497h.

(75) Pak, J.; Jang, J.; Cho, K.; Kim, T.-Y.; Kim, J.-K.; Song, Y.; Hong, W.-K.; Min, M.; Lee, H.; Lee, T. Enhancement of Photodetection Characteristics of MoS_2 Field Effect Transistors Using Surface Treatment with Copper Phthalocyanine. *Nanoscale* **2015**, *7* (44), 18780–18788. https://doi.org/10.1039/C5NR04836B.

(76) Vincett, P. S.; Voigt, E. M.; Rieckhoff, K. E. Phosphorescence and Fluorescence of Phthalocyanines. *J. Chem. Phys.* **1971**, *55* (8), 4131–4140. https://doi.org/10.1063/1.1676714.

(77) Terao, Y.; Sasabe, H.; Adachi, C. Correlation of Hole Mobility, Exciton Diffusion Length, and Solar Cell Characteristics in Phthalocyanine/Fullerene Organic Solar Cells. *Appl. Phys. Lett.* **2007**, *90* (10), 103515. https://doi.org/10.1063/1.2711525.

(78) Sangwan, V. K.; Lee, H.-S.; Bergeron, H.; Balla, I.; Beck, M. E.; Chen, K.-S.; Hersam, M. C. Multi-Terminal Memtransistors from Polycrystalline Monolayer Molybdenum Disulfide. *Nature* **2018**, *554* (7693), 500–504. https://doi.org/10.1038/nature25747.

(79) Carvalho, A.; Ribeiro, R. M.; Castro Neto, A. H. Band Nesting and the Optical Response of Two-Dimensional Semiconducting Transition Metal Dichalcogenides. *Phys. Rev. B - Condens. Matter Mater. Phys.* **2013**, *88* (11), 115205. https://doi.org/10.1103/PhysRevB.88.115205.

(80) Hill, I. G.; Kahn, A. Energy Level Alignment at Interfaces of Organic Semiconductor Heterostructures. *J. Appl. Phys.* **1998**, *84* (10), 5583–5586. https://doi.org/10.1063/1.368864.

(81) Farag, A. A. M. Optical Absorption Studies of Copper Phthalocyanine Thin Films. *Opt. Laser Technol.* **2007**, *39* (4), 728–732. https://doi.org/10.1016/j.optlastec.2006.03.011.

(82) McVie, J.; Sinclair, R. S.; Truscott, T. G. Triplet States of Copper and Metal-Free Phthalocyanines. *J. Chem. Soc. Faraday Trans. 2 Mol. Chem. Phys.* **1978**, *74*, 1870–1879. https://doi.org/10.1039/F29787401870.

(83) Millard, R. R.; Greene, B. I. Direct Determination of Nonradiative Relaxation Rates in Nonfluorescent Metallophthalocyanines. *J. Phys. Chem.* **1985**, *89* (14), 2976–2978. https://doi.org/10.1021/j100260a004.

(84) Ma, G.; Guo, L.; Mi, J.; Liu, Y.; Qian, S.; Pan, D.; Huang, Y. Femtosecond Nonlinear Optical Response of Metallophthalocyanine Films. *Solid State Commun.* **2001**, *118* (12), 633–638. https://doi.org/10.1016/S0038-1098(01)00183-1.

(85) Dutton, G. J.; Robey, S. W. Exciton Dynamics at CuPc/C60 Interfaces: Energy Dependence of Exciton Dissociation. *J. Phys. Chem. C* **2012**, *116* (36), 19173–19181. https://doi.org/10.1021/jp305637r.

(86) Caplins, B. W.; Mullenbach, T. K.; Holmes, R. J.; Blank, D. A. Femtosecond to Nanosecond Excited State Dynamics of Vapor Deposited Copper Phthalocyanine Thin

Films. *Phys. Chem. Chem. Phys.* **2016**, *18* (16), 11454–11459. https://doi.org/10.1039/c6cp00958a.

(87) Pak, J.; Min, M.; Cho, K.; Lien, D. H.; Ahn, G. H.; Jang, J.; Yoo, D.; Chung, S.; Javey, A.; Lee, T. Improved Photoswitching Response Times of MoS 2 Field-Effect Transistors by Stacking p -Type Copper Phthalocyanine Layer. *Appl. Phys. Lett.* **2016**, *109* (18), 183502. https://doi.org/10.1063/1.4966668.

(88) Cunningham, P. D.; McCreary, K. M.; Hanbicki, A. T.; Currie, M.; Jonker, B. T.; Hayden, L. M. Charge Trapping and Exciton Dynamics in Large-Area CVD Grown MoS2. *J. Phys. Chem. C* **2016**, *120* (10), 5819–5826. https://doi.org/10.1021/acs.jpcc.6b00647.

(89) Wang, H.; Zhang, C.; Rana, F. Ultrafast Dynamics of Defect-Assisted Electron-Hole Recombination in Monolayer MoS2. *Nano Lett.* **2015**, *15* (1), 339–345. https://doi.org/10.1021/nl503636c.

(90) Liu, X. Y.; Xie, X. Y.; Fang, W. H.; Cui, G. Theoretical Insights into Interfacial Electron Transfer between Zinc Phthalocyanine and Molybdenum Disulfide. *J. Phys. Chem. A* **2018**, *122* (50), 9587–9596. https://doi.org/10.1021/acs.jpca.8b07816.

(91) Jeong, J.; Park, S.; Kang, S. J.; Lee, H.; Yi, Y. Impacts of Molecular Orientation on the Hole Injection Barrier Reduction: CuPc/HAT-CN/Graphene. *J. Phys. Chem. C* **2016**, *120* (4), 2292–2298. https://doi.org/10.1021/acs.jpcc.5b11535.

(92) Murray, C.; Dozova, N.; McCaffrey, J. G.; FitzGerald, S.; Shafizadeh, N.; Crépin, C. Infra-Red and Raman Spectroscopy of Free-Base and Zinc Phthalocyanines Isolated in Matrices. *Phys. Chem. Chem. Phys.* **2010**, *12* (35), 10406–10422. https://doi.org/10.1039/c0cp00055h.

(93) Alkhamisi, M.; Korolkov, V. V.; Nizovtsev, A. S.; Kerfoot, J.; Taniguchi, T.; Watanabe, K.; Besley, N. A.; Besley, E.; Beton, P. H. The Growth and Fluorescence of Phthalocyanine Monolayers, Thin Films and Multilayers on Hexagonal Boron Nitride. *Chem. Commun.* **2018**, *54* (85), 12021–12024. https://doi.org/10.1039/c8cc06304d.

(94) Zhang, L.; Yang, Y.; Huang, H.; Lyu, L.; Zhang, H.; Cao, N.; Xie, H.; Gao, X.; Niu, D.; Gao, Y. Thickness-Dependent Air-Exposure-Induced Phase Transition of CuPc Ultrathin Films to Well-Ordered One-Dimensional Nanocrystals on Layered Substrates. *J. Phys. Chem. C* **2015**, *119* (8), 4217–4223. https://doi.org/10.1021/jp512613z.

(95) Mativetsky, J. M.; Wang, H.; Lee, S. S.; Whittaker-Brooks, L.; Loo, Y. L. Face-on Stacking and Enhanced out-of-Plane Hole Mobility in Graphene-Templated Copper Phthalocyanine. *Chem. Commun.* **2014**, *50* (40), 5319–5321. https://doi.org/10.1039/c3cc47516f.

(96) Knowles, K. E.; Malicki, M.; Weiss, E. A. Dual-Time Scale Photoinduced Electron Transfer from PbS Quantum Dots to a Molecular Acceptor. *J. Am. Chem. Soc.* **2012**, *134* (30), 12470–12473. https://doi.org/10.1021/ja3060222.

(97) Lin, C. L.; Lee, C. C.; Ho, K. C. Spectroelectrochemical Studies of Manganese Phthalocyanine Thin Films for Applications in Electrochromic Devices. *J. Electroanal. Chem.* **2002**, *524–525*, 81–89. https://doi.org/10.1016/S0022-0728(02)00757-X.

(98) Ade, H.; Wang, M.; Tumbleston, J. R.; Huang, F.; Gann, E.; Ma, W. Domain Purity, Miscibility, and Molecular Orientation at Donor/Acceptor Interfaces in High Performance Organic Solar Cells: Paths to Further Improvement. *Adv. Energy Mater.* **2013**, *3* (7), 864–872. https://doi.org/10.1002/aenm.201200912.

(99) Tumbleston, J. R.; Ma, W.; You, W.; Gann, E.; Collins, B. A.; Ade, H.; Stuart, A. C.; Yang, L. The Influence of Molecular Orientation on Organic Bulk Heterojunction Solar Cells. *Nat. Photonics* **2014**, *8* (5), 385–391. https://doi.org/10.1038/nphoton.2014.55.

(100) Hörmann, U.; Lorch, C.; Hinderhofer, A.; Gerlach, A.; Gruber, M.; Kraus, J.; Sykora, B.; Grob, S.; Linderl, T.; Wilke, A.; Opitz, A.; Hansson, R.; Anselmo, A. S.; Ozawa, Y.; Nakayama, Y.; Ishii, H.; Koch, N.; Moons, E.; Schreiber, F.; Brütting, W. Voc from a Morphology Point of View: The Influence of Molecular Orientation on the Open Circuit Voltage of Organic Planar Heterojunction Solar Cells. *J. Phys. Chem. C* **2014**, *118* (46), 26462–26470. https://doi.org/10.1021/jp506180k.

(101) Szarko, J. M.; Guo, J.; Liang, Y.; Lee, B.; Rolczynski, B. S.; Strzalka, J.; Xu, T.; Loser, S.; Marks, T. J.; Yu, L.; Chen, L. X. When Function Follows Form: Effects of Donor Copolymer Side Chains on Film Morphology and BHJ Solar Cell Performance. *Adv. Mater.* **2010**, *22* (48), 5468–5472. https://doi.org/10.1002/adma.201002687.

(102) Szarko, J. M.; Rolczynski, B. S.; Lou, S. J.; Xu, T.; Strzalka, J.; Marks, T. J.; Yu, L.; Chen, L. X. Photovoltaic Function and Exciton/Charge Transfer Dynamics in a Highly Efficient Semiconducting Copolymer. *Adv. Funct. Mater.* **2014**, *24* (1), 10–26. https://doi.org/10.1002/adfm.201301820.

(103) Guo, X.; Zhou, N.; Lou, S. J.; Smith, J.; Tice, D. B.; Hennek, J. W.; Ortiz, R. P.; Navarrete, J. T. L.; Li, S.; Strzalka, J.; Chen, L. X.; Chang, R. P. H.; Facchetti, A.; Marks, T. J. Polymer Solar Cells with Enhanced Fill Factors. *Nat. Photonics* **2013**, *7* (10), 825–833. https://doi.org/10.1038/nphoton.2013.207.

(104) Warren, S. C.; Guney-Altay, O.; Grzybowski, B. A. Responsive and Nonequilibrium Nanomaterials. *J. Phys. Chem. Lett.* **2012**, *3* (15), 2103–2111. https://doi.org/10.1021/jz300584c.

(105) Padgaonkar, S.; Olding, J. N.; Lauhon, L. J.; Hersam, M. C.; Weiss, E. A. Emergent Optoelectronic Properties of Mixed-Dimensional Heterojunctions. *Acc. Chem. Res.* **2020**. https://doi.org/10.1021/acs.accounts.9b00581.

(106) Zhao, Y.; Ippolito, S.; Samorì, P. Functionalization of 2D Materials with Photosensitive Molecules: From Light-Responsive Hybrid Systems to Multifunctional Devices. *Adv. Opt. Mater.* **2019**, 1900286–1900286. https://doi.org/10.1002/adom.201900286.

(107) Gonzalez, A.; Kengmana, E. S.; Fonseca, M. V.; Han, G. G. D. Solid-State Photoswitching Molecules: Structural Design for Isomerization in Condensed Phase. *Mater. Today Adv.* **2020**, *6*, 100058. https://doi.org/10.1016/j.mtadv.2020.100058.

(108) Yildiz, I.; Deniz, E.; Raymo, F. M. Fluorescence Modulation with Photochromic Switches in Nanostructured Constructs. *Chem. Soc. Rev.* **2009**, *38* (7), 1859–1867. https://doi.org/10.1039/B804151M.

(109) Wei, Y.; Han, S.; Kim, J.; Soh, S.; Grzybowski, B. A. Photoswitchable Catalysis Mediated by Dynamic Aggregation of Nanoparticles. *J. Am. Chem. Soc.* **2010**, *132* (32), 11018–11020. https://doi.org/10.1021/ja104260n.

(110) Zhao, Y.; Bertolazzi, S.; Samorì, P. A Universal Approach toward Light-Responsive Two-Dimensional Electronics: Chemically Tailored Hybrid van Der Waals Heterostructures. *ACS Nano* **2019**, *13* (4), 4814–4825. https://doi.org/10.1021/acsnano.9b01716.

(111) Paquette, M. M.; Plaul, D.; Kurimoto, A.; Patrick, B. O.; Frank, N. L. Opto-Spintronics: Photoisomerization-Induced Spin State Switching at 300 K in Photochrome Cobalt–

Dioxolene Thin Films. *J. Am. Chem. Soc.* **2018**, *140* (44), 14990–15000. https://doi.org/10.1021/jacs.8b09190.

(112) Park, J.; Yuan, D.; Pham, K. T.; Li, J.-R.; Yakovenko, A.; Zhou, H.-C. Reversible Alteration of CO2 Adsorption upon Photochemical or Thermal Treatment in a Metal–Organic Framework. *J. Am. Chem. Soc.* **2012**, *134* (1), 99–102. https://doi.org/10.1021/ja209197f.

(113) Lilly, G. D.; Whalley, A. C.; Grunder, S.; Valente, C.; Frederick, M. T.; Stoddart, J. F.; Weiss, E. A. Switchable Photoconductivity of Quantum Dot Films Using Cross-Linking Ligands with Light-Sensitive Structures. *J. Mater. Chem.* **2011**, *21* (31), 11492–11497. https://doi.org/10.1039/c0jm04397d.

(114) Impellizzeri, S.; McCaughan, B.; Callan, J. F.; Raymo, F. M. Photoinduced Enhancement in the Luminescence of Hydrophilic Quantum Dots Coated with Photocleavable Ligands. *J. Am. Chem. Soc.* **2012**, *134* (4), 2276–2283. https://doi.org/10.1021/ja209873g.

(115) Credi, A. Quantum Dot-Molecule Hybrids: A Paradigm for Light-Responsive Nanodevices. *New J. Chem.* **2012**, *36* (10), 1925–1930. https://doi.org/10.1039/c2nj40335h.

(116) Erno, Z.; Yildiz, I.; Gorodetsky, B.; Raymo, F. M.; Branda, N. R. Optical Control of Quantum Dot Luminescence via Photoisomerization of a Surface-Coordinated, Cationic Dithienylethene. *Photochem. Photobiol. Sci.* **2010**, *9* (2), 249–253. https://doi.org/10.1039/b9pp00115h.

(117) Díaz, S. A.; Gillanders, F.; Susumu, K.; Oh, E.; Medintz, I. L.; Jovin, T. M. Water-Soluble, Thermostable, Photomodulated Color-Switching Quantum Dots. *Chem. - Eur. J.* **2017**, *23* (2), 263–267. https://doi.org/10.1002/chem.201604688.

(118) Díaz, S. A.; Menéndez, G. O.; Etchehon, M. H.; Giordano, L.; Jovin, T. M.; Jares-Erijman, E. A. Photoswitchable Water-Soluble Quantum Dots: PcFRET Based on Amphiphilic Photochromic Polymer Coating. *ACS Nano* **2011**, *5* (4), 2795–2805. https://doi.org/10.1021/nn103243c.

(119) Díaz, S. A.; Giordano, L.; Jovin, T. M.; Jares-Erijman, E. A. Modulation of a Photoswitchable Dual-Color Quantum Dot Containing a Photochromic FRET Acceptor and an Internal Standard. *Nano Lett.* **2012**, *12* (7), 3537–3544. https://doi.org/10.1021/nl301093s.

(120) Díaz, S. A.; Gillanders, F.; Jares-Erijman, E. A.; Jovin, T. M. Photoswitchable Semiconductor Nanocrystals with Self-Regulating Photochromic Förster Resonance Energy Transfer Acceptors. *Nat. Commun.* **2015**, *6* (1), 6036. https://doi.org/10.1038/ncomms7036.

(121) Zhu, L.; Zhu, M.-Q.; Hurst, J. K.; Li, A. D. Q. Light-Controlled Molecular Switches Modulate Nanocrystal Fluorescence. *J. Am. Chem. Soc.* **2005**, *127* (25), 8968–8970. https://doi.org/10.1021/ja0423421.

(122) Zhang, Y.; Zhang, K.; Wang, J.; Tian, Z.; Li, A. D. Q. Photoswitchable Fluorescent Nanoparticles and Their Emerging Applications. *Nanoscale* **2015**, *7* (46), 19342–19357. https://doi.org/10.1039/c5nr05436b.

(123) Saeed, S.; Yin, J.; Khalid, M. A.; Channar, P. A.; Shabir, G.; Saeed, A.; Arif Nadeem, M.; Soci, C.; Iqbal, A. Photoresponsive Azobenzene Ligand as an Efficient Electron Acceptor

for Luminous CdTe Quantum Dots. *J. Photochem. Photobiol. Chem.* **2019**, *375*, 48–53. https://doi.org/10.1016/j.jphotochem.2019.02.007.

(124) Bang, J.; Park, J.; Velu, R.; Yoon, E.; Lee, K.; Cho, S.; Cha, S.; Chae, G.; Joo, T.; Kim, S. Photoswitchable Quantum Dots by Controlling the Photoinduced Electron Transfers. *Chem. Commun.* **2012**, *48* (73), 9174–9176. https://doi.org/10.1039/C2CC34002J.

(125) Berberich, M.; Krause, A. M.; Orlandi, M.; Scandola, F.; Würthner, F. Toward Fluorescent Memories with Nondestructive Readout: Photoswitching of Fluorescence by Intramolecular Electron Transfer in a Diaryl Ethene-Perylene Bisimide Photochromic System. *Angew. Chem. - Int. Ed.* **2008**, *47* (35), 6616–6619. https://doi.org/10.1002/anie.200802007.

(126) Fukaminato, T.; Doi, T.; Tamaoki, N.; Okuno, K.; Ishibashi, Y.; Miyasaka, H.; Irie, M. Single-Molecule Fluorescence Photoswitching of a Diarylethene- Perylenebisimide Dyad: Non-Destructive Fluorescence Readout. *J. Am. Chem. Soc.* **2011**, *133* (13), 4984–4990. https://doi.org/10.1021/ja110686t.

(127) Berberich, M.; Natali, M.; Spenst, P.; Chiorboli, C.; Scandola, F.; Würthner, F. Nondestructive Photoluminescence Read-Out by Intramolecular Electron Transfer in a Perylene Bisimide-Diarylethene Dyad. *Chem. – Eur. J.* **2012**, *18* (43), 13651–13664. https://doi.org/10.1002/chem.201201484.

(128) Fukaminato, T.; Ishida, S.; Métivier, R. Photochromic Fluorophores at the Molecular and Nanoparticle Levels: Fundamentals and Applications of Diarylethenes. *NPG Asia Mater.* **2018**, *10* (9), 859–881. https://doi.org/10.1038/s41427-018-0075-9.

(129) Yokoyama, Y. Fulgides for Memories and Switches. *Chem. Rev.* **2000**, *100* (5), 1717–1740. https://doi.org/10.1021/cr980070c.

(130) Renth, F.; Siewertsen, R.; Temps, F. Enhanced Photoswitching and Ultrafast Dynamics in Structurally Modified Photochromic Fulgides. *Int. Rev. Phys. Chem.* **2013**, *32* (1), 1–38. https://doi.org/10.1080/0144235X.2012.729331.

(131) Siewertsen, R.; Renth, F.; Temps, F.; Sönnichsen, F. Parallel Ultrafast E-C Ring Closure and E-Z Isomerisation in a Photochromic Furylfulgide Studied by Femtosecond Time-Resolved Spectroscopy. *Phys. Chem. Chem. Phys.* **2009**, *11* (28), 5952–5961. https://doi.org/10.1039/b821344e.

(132) Siewertsen, R.; Strübe, F.; Mattay, J.; Renth, F.; Temps, F. Tuning of Switching Properties and Excited-State Dynamics of Fulgides by Structural Modifications. *Phys. Chem. Chem. Phys.* **2011**, *13* (9), 3800–3808. https://doi.org/10.1039/c0cp01890b.

(133) Port, H.; Gärtner, P.; Hennrich, M.; Ramsteiner, I.; Schöck, T. Ultrafast Photochromic Reactions of Fulgide Photoswitches. *Mol. Cryst. Liq. Cryst.* **2005**, *430* (1), 15–21. https://doi.org/10.1080/15421400590946109.

(134) Slavov, C.; Bellakbil, N.; Wahl, J.; Mayer, K.; Rück-Braun, K.; Burghardt, I.; Wachtveitl, J.; Braun, M. Ultrafast Coherent Oscillations Reveal a Reactive Mode in the Ring-Opening Reaction of Fulgides. *Phys. Chem. Chem. Phys.* **2015**, *17* (21), 14045–14053. https://doi.org/10.1039/c5cp01878a.

(135) Slavov, C.; Boumrifak, C.; Hammer, C. A.; Trojanowski, P.; Chen, X.; Lees, W. J.; Wachtveitl, J.; Braun, M. The Ultrafast Reactions in the Photochromic Cycle of Water-Soluble Fulgimide Photoswitches. *Phys. Chem. Chem. Phys.* **2016**, *18* (15), 10289–10296. https://doi.org/10.1039/c5cp06866e.

(136) Siewertsen, R.; Strübe, F.; Mattay, J.; Renth, F.; Temps, F. Electronic and Steric Effects on the Photo-Induced C → E Ring-Opening of Structurally Modified Furylfulgides. *Phys. Chem. Chem. Phys.* **2011**, *13* (34), 15699–15707. https://doi.org/10.1039/C1CP21320B.
(137) Morris-Cohen, A. J.; Malicki, M.; Peterson, M. D.; Slavin, J. W. J.; Weiss, E. A. Chemical, Structural, and Quantitative Analysis of the Ligand Shells of Colloidal Quantum Dots. *Chem. Mater.* **2013**, *25* (8), 1155–1165. https://doi.org/10.1021/cm302108j.
(138) Knauf, R. R.; Lennox, J. C.; Dempsey, J. L. Quantifying Ligand Exchange Reactions at CdSe Nanocrystal Surfaces. *Chem. Mater.* **2016**, *28* (13), 4762–4770. https://doi.org/10.1021/acs.chemmater.6b01827.
(139) Hens, Z.; Martins, J. C. A Solution NMR Toolbox for Characterizing the Surface Chemistry of Colloidal Nanocrystals. *Chem. Mater.* **2013**, *25* (8), 1211–1221. https://doi.org/10.1021/cm303361s.
(140) Fritzinger, B.; Capek, R. K.; Lambert, K.; Martins, J. C.; Hens, Z. Utilizing Self-Exchange to Address the Binding of Carboxylic Acid Ligands to CdSe Quantum Dots. *J. Am. Chem. Soc.* **2010**, *132* (29), 10195–10201. https://doi.org/10.1021/ja104351q.
(141) Wang, J.; Zhou, R.; He, Z.-R.; He, Z. Phosphane-Mediated Domino Synthesis of Tetrasubstituted Furans from Simple Terminal Activated Olefins. *Eur. J. Org. Chem.* **2012**, *2012* (30), 6033–6041. https://doi.org/10.1002/ejoc.201200945.
(142) Lee, W.-W. W.; Gan, L.-M.; Loh, T.-P. Synthesis and Photochromic Properties of Cycloalkylidene Fulgides. *Synlett* **2005**, *2005* (16), 2473–2477. https://doi.org/10.1055/s-2005-917082.
(143) Tomoda, A.; Kaneko, A.; Tsuboi, H.; Matsushima, R. Photochromism of Heterocyclic Fulgides. IV. Relationship between Chemical Structure and Photochromic Performance. *Bull. Chem. Soc. Jpn.* **1993**, *66* (1), 330–333. https://doi.org/10.1246/bcsj.66.330.
(144) Flamee, S.; Cirillo, M.; Abe, S.; De Nolf, K.; Gomes, R.; Aubert, T.; Hens, Z. Fast, High Yield, and High Solid Loading Synthesis of Metal Selenide Nanocrystals. *Chem. Mater.* **2013**, *25* (12), 2476–2483. https://doi.org/10.1021/cm400799e.
(145) Yu, W. W.; Qu, L.; Guo, W.; Peng, X. Experimental Determination of the Extinction Coefficient of CdTe, CdSe, and CdS Nanocrystals. *Chem. Mater.* **2003**, *15* (14), 2854–2860. https://doi.org/10.1021/cm034081k.
(146) Jasieniak, J.; Smith, L.; van Embden, J.; Mulvaney, P.; Califano, M. Re-Examination of the Size-Dependent Absorption Properties of CdSe Quantum Dots. *J. Phys. Chem. C* **2009**, *113* (45), 19468–19474. https://doi.org/10.1021/jp906827m.
(147) Jasieniak, J.; Califano, M.; Watkins, S. E. Size-Dependent Valence and Conduction Band-Edge Energies of Semiconductor Nanocrystals. *ACS Nano* **2011**, *5* (7), 5888–5902. https://doi.org/10.1021/nn201681s.
(148) Valiev, M.; Bylaska, E. J.; Govind, N.; Kowalski, K.; Straatsma, T. P.; Van Dam, H. J. J.; Wang, D.; Nieplocha, J.; Apra, E.; Windus, T. L.; de Jong, W. A. NWChem: A Comprehensive and Scalable Open-Source Solution for Large Scale Molecular Simulations. *Comput. Phys. Commun.* **2010**, *181* (9), 1477–1489. https://doi.org/10.1016/j.cpc.2010.04.018.
(149) Aprà, E.; Bylaska, E. J.; de Jong, W. A.; Govind, N.; Kowalski, K.; Straatsma, T. P.; Valiev, M.; van Dam, H. J. J.; Alexeev, Y.; Anchell, J.; Anisimov, V.; Aquino, F. W.;

Atta-Fynn, R.; Autschbach, J.; Bauman, N. P.; Becca, J. C.; Bernholdt, D. E.; Bhaskaran-Nair, K.; Bogatko, S.; Borowski, P.; Boschen, J.; Brabec, J.; Bruner, A.; Cauët, E.; Chen, Y.; Chuev, G. N.; Cramer, C. J.; Daily, J.; Deegan, M. J. O.; Dunning, T. H.; Dupuis, M.; Dyall, K. G.; Fann, G. I.; Fischer, S. A.; Fonari, A.; Früchtl, H.; Gagliardi, L.; Garza, J.; Gawande, N.; Ghosh, S.; Glaesemann, K.; Götz, A. W.; Hammond, J.; Helms, V.; Hermes, E. D.; Hirao, K.; Hirata, S.; Jacquelin, M.; Jensen, L.; Johnson, B. G.; Jónsson, H.; Kendall, R. A.; Klemm, M.; Kobayashi, R.; Konkov, V.; Krishnamoorthy, S.; Krishnan, M.; Lin, Z.; Lins, R. D.; Littlefield, R. J.; Logsdail, A. J.; Lopata, K.; Ma, W.; Marenich, A. V.; Martin del Campo, J.; Mejia-Rodriguez, D.; Moore, J. E.; Mullin, J. M.; Nakajima, T.; Nascimento, D. R.; Nichols, J. A.; Nichols, P. J.; Nieplocha, J.; Otero-de-la-Roza, A.; Palmer, B.; Panyala, A.; Pirojsirikul, T.; Peng, B.; Peverati, R.; Pittner, J.; Pollack, L.; Richard, R. M.; Sadayappan, P.; Schatz, G. C.; Shelton, W. A.; Silverstein, D. W.; Smith, D. M. A.; Soares, T. A.; Song, D.; Swart, M.; Taylor, H. L.; Thomas, G. S.; Tipparaju, V.; Truhlar, D. G.; Tsemekhman, K.; Van Voorhis, T.; Vázquez-Mayagoitia, Á.; Verma, P.; Villa, O.; Vishnu, A.; Vogiatzis, K. D.; Wang, D.; Weare, J. H.; Williamson, M. J.; Windus, T. L.; Woliński, K.; Wong, A. T.; Wu, Q.; Yang, C.; Yu, Q.; Zacharias, M.; Zhang, Z.; Zhao, Y.; Harrison, R. J. NWChem: Past, Present, and Future. *J. Chem. Phys.* **2020**, *152* (18), 184102. https://doi.org/10.1063/5.0004997.

(150) Zhu, H.; Yang, Y.; Hyeon-Deuk, K.; Califano, M.; Song, N.; Wang, Y.; Zhang, W.; Prezhdo, O. V.; Lian, T. Auger-Assisted Electron Transfer from Photoexcited Semiconductor Quantum Dots. *Nano Lett.* **2014**, *14* (3), 1263–1269. https://doi.org/10.1021/nl4041687.

(151) Krivenkov, V.; Samokhvalov, P.; Zvaigzne, M.; Martynov, I.; Chistyakov, A.; Nabiev, I. Ligand-Mediated Photobrightening and Photodarkening of CdSe/ZnS Quantum Dot Ensembles. *J. Phys. Chem. C* **2018**, *122* (27), 15761–15771. https://doi.org/10.1021/acs.jpcc.8b04544.

(152) Carrillo-Carrión, C.; Cárdenas, S.; Simonet, B. M.; Valcárcel, M. Quantum Dots Luminescence Enhancement Due to Illumination with UV/Vis Light. *Chem. Commun.* **2009**, No. 35, 5214–5226. https://doi.org/10.1039/B904381K.

(153) Lian, S.; Weinberg, D. J.; Harris, R. D.; Kodaimati, M. S.; Weiss, E. A. Subpicosecond Photoinduced Hole Transfer from a CdS Quantum Dot to a Molecular Acceptor Bound Through an Exciton-Delocalizing Ligand. *ACS Nano* **2016**, *10* (6), 6372–6382. https://doi.org/10.1021/acsnano.6b02814.

(154) Padgaonkar, S.; Amsterdam, S. H.; Bergeron, H.; Su, K.; Marks, T. J.; Hersam, M. C.; Weiss, E. A. Molecular-Orientation-Dependent Interfacial Charge Transfer in Phthalocyanine/MoS2 Mixed-Dimensional Heterojunctions. *J. Phys. Chem. C* **2019**, *123* (21), 13337–13343. https://doi.org/10.1021/acs.jpcc.9b04063.

(155) Hatchard, C. G.; Parker, C. A. A New Sensitive Chemical Actinometer - II. Potassium Ferrioxalate as a Standard Chemical Actinometer. *Proc. R. Soc. Lond. Ser. Math. Phys. Sci.* **1956**, *235* (1203), 518–536. https://doi.org/10.1098/rspa.1956.0102.

(156) Sowa, J. K.; Weiss, E. A.; Seideman, T. Photoisomerization-Coupled Electron Transfer. *J. Chem. Phys.* **2020**, *153* (3), 034301. https://doi.org/10.1063/5.0013468.

(157) Gusmão, R.; Sofer, Z.; Pumera, M. Black Phosphorus Rediscovered: From Bulk Material to Monolayers. *Angew. Chem. Int. Ed.* **2017**, *56* (28), 8052–8072. https://doi.org/10.1002/anie.201610512.
(158) Xia, F.; Wang, H.; Jia, Y. Rediscovering Black Phosphorus as an Anisotropic Layered Material for Optoelectronics and Electronics. *Nat. Commun.* **2014**, *5* (1), 4458. https://doi.org/10.1038/ncomms5458.
(159) Favron, A.; Gaufrès, E.; Fossard, F.; Phaneuf-L'Heureux, A.-L.; Tang, N. Y.-W.; Lévesque, P. L.; Loiseau, A.; Leonelli, R.; Francoeur, S.; Martel, R. Photooxidation and Quantum Confinement Effects in Exfoliated Black Phosphorus. *Nat. Mater.* **2015**, *14* (8), 826–832. https://doi.org/10.1038/nmat4299.
(160) Wood, J. D.; Wells, S. A.; Jariwala, D.; Chen, K.-S.; Cho, E.; Sangwan, V. K.; Liu, X.; Lauhon, L. J.; Marks, T. J.; Hersam, M. C. Effective Passivation of Exfoliated Black Phosphorus Transistors against Ambient Degradation. *Nano Lett.* **2014**, *14* (12), 6964–6970. https://doi.org/10.1021/nl5032293.
(161) Abate, Y.; Akinwande, D.; Gamage, S.; Wang, H.; Snure, M.; Poudel, N.; Cronin, S. B. Recent Progress on Stability and Passivation of Black Phosphorus. *Adv. Mater.* **2018**, *30* (29), 1704749. https://doi.org/10.1002/adma.201704749.
(162) Castellanos-Gomez, A. Black Phosphorus: Narrow Gap, Wide Applications. *J. Phys. Chem. Lett.* **2015**, *6* (21), 4280–4291. https://doi.org/10.1021/acs.jpclett.5b01686.
(163) Zhang, S.; Li, Y.; Zhang, X.; Dong, N.; Wang, K.; Hanlon, D.; N. Coleman, J.; Zhang, L.; Wang, J. Slow and Fast Absorption Saturation of Black Phosphorus: Experiment and Modelling. *Nanoscale* **2016**, *8* (39), 17374–17382. https://doi.org/10.1039/C6NR06076E.
(164) Engel, M.; Steiner, M.; Avouris, P. Black Phosphorus Photodetector for Multispectral, High-Resolution Imaging. *Nano Lett.* **2014**, *14* (11), 6414–6417. https://doi.org/10.1021/nl502928y.
(165) Guo, Q.; Pospischil, A.; Bhuiyan, M.; Jiang, H.; Tian, H.; Farmer, D.; Deng, B.; Li, C.; Han, S.-J.; Wang, H.; Xia, Q.; Ma, T.-P.; Mueller, T.; Xia, F. Black Phosphorus Mid-Infrared Photodetectors with High Gain. *Nano Lett.* **2016**, *16* (7), 4648–4655. https://doi.org/10.1021/acs.nanolett.6b01977.
(166) Sangwan, V. K.; Hersam, M. C. Electronic Transport in Two-Dimensional Materials. *Annu. Rev. Phys. Chem.* **2018**, *69* (1), 299–325. https://doi.org/10.1146/annurev-physchem-050317-021353.
(167) Sauer, K. Photosynthetic Membranes. *Acc. Chem. Res.* **1978**, *11* (7), 257–264. https://doi.org/10.1021/ar50127a001.
(168) Taghipour, N.; Hernandez Martinez, P. L.; Ozden, A.; Olutas, M.; Dede, D.; Gungor, K.; Erdem, O.; Kosku Perkgoz, N.; Demir, H. V. Near-Unity Efficiency Energy Transfer from Colloidal Semiconductor Quantum Wells of CdSe/CdS Nanoplatelets to A Monolayer of MoS2. *ACS Nano* **2018**. https://doi.org/10.1021/acsnano.8b04119.
(169) Konstantatos, G.; Badioli, M.; Gaudreau, L.; Osmond, J.; Bernechea, M.; de Arquer, F. P. G.; Gatti, F.; Koppens, F. H. L. Hybrid Graphene–Quantum Dot Phototransistors with Ultrahigh Gain. *Nat. Nanotechnol.* **2012**, *7* (6), 363–368. https://doi.org/10.1038/nnano.2012.60.
(170) Jariwala, D.; Marks, T. J.; Hersam, M. C. Mixed-Dimensional van Der Waals Heterostructures. *Nat. Mater.* **2017**, *16* (2), 170–181. https://doi.org/10.1038/nmat4703.

(171) Gaudreau, L.; Tielrooij, K. J.; Prawiroatmodjo, G. E. D. K.; Osmond, J.; de Abajo, F. J. G.; Koppens, F. H. L. Universal Distance-Scaling of Nonradiative Energy Transfer to Graphene. *Nano Lett.* **2013**, *13* (5), 2030–2035. https://doi.org/10.1021/nl400176b.
(172) Chen, Z.; Berciaud, S.; Nuckolls, C.; Heinz, T. F.; Brus, L. E. Energy Transfer from Individual Semiconductor Nanocrystals to Graphene. *ACS Nano* **2010**, *4* (5), 2964–2968. https://doi.org/10.1021/nn1005107.
(173) Prins, F.; Goodman, A. J.; Tisdale, W. A. Reduced Dielectric Screening and Enhanced Energy Transfer in Single- and Few-Layer MoS2. *Nano Lett.* **2014**, *14* (11), 6087–6091. https://doi.org/10.1021/nl5019386.
(174) Raja, A.; Montoya-Castillo, A.; Zultak, J.; Zhang, X. X.; Ye, Z.; Roquelet, C.; Chenet, D. A.; Van Der Zande, A. M.; Huang, P.; Jockusch, S.; Hone, J.; Reichman, D. R.; Brus, L. E.; Heinz, T. F. Energy Transfer from Quantum Dots to Graphene and MoS2: The Role of Absorption and Screening in Two-Dimensional Materials. *Nano Lett.* **2016**, *16* (4), 2328–2333. https://doi.org/10.1021/acs.nanolett.5b05012.
(175) Li, M.; Chen, J.-S.; Cotlet, M. Light-Induced Interfacial Phenomena in Atomically Thin 2D van Der Waals Material Hybrids and Heterojunctions. *ACS Energy Lett.* **2019**, *4* (9), 2323–2335. https://doi.org/10.1021/acsenergylett.9b01399.
(176) Zang, H.; Routh, P. K.; Huang, Y.; Chen, J. S.; Sutter, E.; Sutter, P.; Cotlet, M. Nonradiative Energy Transfer from Individual CdSe/ZnS Quantum Dots to Single-Layer and Few-Layer Tin Disulfide. *ACS Nano* **2016**, *10* (4), 4790–4796. https://doi.org/10.1021/acsnano.6b01538.
(177) Federspiel, F.; Froehlicher, G.; Nasilowski, M.; Pedetti, S.; Mahmood, A.; Doudin, B.; Park, S.; Lee, J. O.; Halley, D.; Dubertret, B.; Gilliot, P.; Berciaud, S. Distance Dependence of the Energy Transfer Rate from a Single Semiconductor Nanostructure to Graphene. *Nano Lett.* **2015**, *15* (2), 1252–1258. https://doi.org/10.1021/nl5044192.
(178) Zhou, H.; Qin, C.; Chen, R.; Zhou, W.; Zhang, G.; Gao, Y.; Xiao, L.; Jia, S. Accurate Investigation on the Fluorescence Resonance Energy Transfer between Single Organic Molecules and Monolayer WSe2 by Quantum Coherent Modulation-Enhanced Single-Molecule Imaging Microscopy. *J. Phys. Chem. Lett.* **2019**, *10* (11), 2849–2856. https://doi.org/10.1021/acs.jpclett.9b00854.
(179) Liu, H.; Wang, T.; Wang, C.; Liu, D.; Luo, J. Exciton Radiative Recombination Dynamics and Nonradiative Energy Transfer in Two-Dimensional Transition-Metal Dichalcogenides. *J. Phys. Chem. C* **2019**, *123* (15), 10087–10093. https://doi.org/10.1021/acs.jpcc.8b12179.
(180) Prasai, D.; Klots, A. R.; Newaz, A.; Niezgoda, J. S.; Orfield, N. J.; Escobar, C. A.; Wynn, A.; Efimov, A.; Jennings, G. K.; Rosenthal, S. J.; Bolotin, K. I. Electrical Control of Near-Field Energy Transfer between Quantum Dots and Two-Dimensional Semiconductors. *Nano Lett.* **2015**, *15* (7), 4374–4380. https://doi.org/10.1021/acs.nanolett.5b00514.
(181) Li, M.; Chen, J.-S.; Routh, P. K.; Zahl, P.; Nam, C.-Y.; Cotlet, M. Distinct Optoelectronic Signatures for Charge Transfer and Energy Transfer in Quantum Dot–MoS2 Hybrid Photodetectors Revealed by Photocurrent Imaging Microscopy. *Adv. Funct. Mater.* **2018**, *28* (29), 1707558. https://doi.org/10.1002/adfm.201707558.

(182) Ra, H.-S.; Kwak, D.-H.; Lee, J.-S. A Hybrid MoS2 Nanosheet–CdSe Nanocrystal Phototransistor with a Fast Photoresponse. *Nanoscale* **2016**, *8* (39), 17223–17230. https://doi.org/10.1039/C6NR05393A.
(183) Gough, J. J.; McEvoy, N.; O'Brien, M.; Bell, A. P.; McCloskey, D.; Boland, J. B.; Coleman, J. N.; Duesberg, G. S.; Bradley, A. L. Dependence of Photocurrent Enhancements in Quantum Dot (QD)-Sensitized MoS2Devices on MoS2Film Properties. *Adv. Funct. Mater.* **2018**, *28* (13), 1706149. https://doi.org/10.1002/adfm.201706149.
(184) Lee, T.; Enomoto, K.; Ohshiro, K.; Inoue, D.; Kikitsu, T.; Hyeon-Deuk, K.; Pu, Y.-J.; Kim, D. Controlling the Dimension of the Quantum Resonance in CdTe Quantum Dot Superlattices Fabricated via Layer-by-Layer Assembly. *Nat. Commun.* **2020**, *11* (1), 5471. https://doi.org/10.1038/s41467-020-19337-0.
(185) Goodfellow, K. M.; Chakraborty, C.; Sowers, K.; Waduge, P.; Wanunu, M.; Krauss, T.; Driscoll, K.; Vamivakas, A. N. Distance-Dependent Energy Transfer between CdSe/CdS Quantum Dots and a Two-Dimensional Semiconductor. *Appl. Phys. Lett.* **2016**, *108* (2), 021101. https://doi.org/10.1063/1.4939845.
(186) Talapin, D. V.; Mekis, I.; Götzinger, S.; Kornowski, A.; Benson, O.; Weller, H. CdSe/CdS/ZnS and CdSe/ZnSe/ZnS Core−Shell−Shell Nanocrystals. *J. Phys. Chem. B* **2004**, *108* (49), 18826–18831. https://doi.org/10.1021/jp046481g.
(187) Wells, S. A.; Henning, A.; Gish, J. T.; Sangwan, V. K.; Lauhon, L. J.; Hersam, M. C. Suppressing Ambient Degradation of Exfoliated InSe Nanosheet Devices via Seeded Atomic Layer Deposition Encapsulation. *Nano Lett.* **2018**, *18* (12), 7876–7882. https://doi.org/10.1021/acs.nanolett.8b03689.
(188) Abellán, G.; Wild, S.; Lloret, V.; Scheuschner, N.; Gillen, R.; Mundloch, U.; Maultzsch, J.; Varela, M.; Hauke, F.; Hirsch, A. Fundamental Insights into the Degradation and Stabilization of Thin Layer Black Phosphorus. *J. Am. Chem. Soc.* **2017**, *139* (30), 10432–10440. https://doi.org/10.1021/jacs.7b04971.
(189) McPhail, M. R.; Campbell, G. P.; Bedzyk, M. J.; Weiss, E. A. Structural Features of PbS Nanocube Monolayers upon Treatment with Mono- and Dicarboxylic Acids and Thiols at a Liquid–Air Interface. *Langmuir* **2016**, *32* (26), 6666–6673. https://doi.org/10.1021/acs.langmuir.6b01444.
(190) Lee, A.-Y.; Ra, H.-S.; Kwak, D.-H.; Jeong, M.-H.; Park, J.-H.; Kang, Y.-S.; Chae, W.-S.; Lee, J.-S. Hybrid Black Phosphorus/Zero-Dimensional Quantum Dot Phototransistors: Tunable Photodoping and Enhanced Photoresponsivity. *ACS Appl. Mater. Interfaces* **2018**, *10* (18), 16033–16040. https://doi.org/10.1021/acsami.8b03285.
(191) Energy Transfer. In *Principles of Fluorescence Spectroscopy*; Lakowicz, J. R., Ed.; Springer US: Boston, MA, 2006; pp 443–475. https://doi.org/10.1007/978-0-387-46312-4_13.
(192) Swathi, R. S.; Sebastian, K. L. Distance Dependence of Fluorescence Resonance Energy Transfer. *J. Chem. Sci.* **2009**, *121* (5), 777. https://doi.org/10.1007/s12039-009-0092-x.
(193) Kuhn, H. Classical Aspects of Energy Transfer in Molecular Systems. *J. Chem. Phys.* **1970**, *53* (1), 101–108. https://doi.org/10.1063/1.1673749.
(194) Hua, X. M.; Gersten, J. I.; Nitzan, A. Theory of Energy Transfer between Molecules near Solid State Particles. *J. Chem. Phys.* **1985**, *83* (7), 3650–3659. https://doi.org/10.1063/1.449120.

(195) Govorov, A. O.; Lee, J.; Kotov, N. A. Theory of Plasmon-Enhanced F\"orster Energy Transfer in Optically Excited Semiconductor and Metal Nanoparticles. *Phys. Rev. B* **2007**, *76* (12), 125308. https://doi.org/10.1103/PhysRevB.76.125308.
(196) Zhang, X.; Marocico, C. A.; Lunz, M.; Gerard, V. A.; Gun'ko, Y. K.; Lesnyak, V.; Gaponik, N.; Susha, A. S.; Rogach, A. L.; Bradley, A. L. Experimental and Theoretical Investigation of the Distance Dependence of Localized Surface Plasmon Coupled Förster Resonance Energy Transfer. *ACS Nano* **2014**, *8* (2), 1273–1283. https://doi.org/10.1021/nn406530m.
(197) McPhail, M. R.; Campbell, G. P.; Bedzyk, M. J.; Weiss, E. A. Structural Features of PbS Nanocube Monolayers upon Treatment with Mono- and Dicarboxylic Acids and Thiols at a Liquid–Air Interface. *Langmuir* **2016**, *32* (26), 6666–6673. https://doi.org/10.1021/acs.langmuir.6b01444.
(198) Wood, J. D.; Wells, S. A.; Jariwala, D.; Chen, K.-S.; Cho, E.; Sangwan, V. K.; Liu, X.; Lauhon, L. J.; Marks, T. J.; Hersam, M. C. Effective Passivation of Exfoliated Black Phosphorus Transistors against Ambient Degradation. *Nano Lett.* **2014**, *14* (12), 6964–6970. https://doi.org/10.1021/nl5032293.
(199) Amsterdam, S. H.; LaMountain, T.; Stanev, T. K.; Sangwan, V. K.; López-Arteaga, R.; Padgaonkar, S.; Watanabe, K.; Taniguchi, T.; Weiss, E. A.; Marks, T. J.; Hersam, M. C.; Stern, N. P. Tailoring the Optical Response of Pentacene Thin Films via Templated Growth on Hexagonal Boron Nitride. *J. Phys. Chem. Lett.* **2021**, *12* (1), 26–31. https://doi.org/10.1021/acs.jpclett.0c03132.
(200) Zang, H.; Routh, P. K.; Huang, Y.; Chen, J.-S.; Sutter, E.; Sutter, P.; Cotlet, M. Nonradiative Energy Transfer from Individual CdSe/ZnS Quantum Dots to Single-Layer and Few-Layer Tin Disulfide. *ACS Nano* **2016**, *10* (4), 4790–4796. https://doi.org/10.1021/acsnano.6b01538.
(201) Prins, F.; Goodman, A. J.; Tisdale, W. A. Reduced Dielectric Screening and Enhanced Energy Transfer in Single- and Few-Layer MoS2. *Nano Lett.* **2014**, *14* (11), 6087–6091. https://doi.org/10.1021/nl5019386.
(202) Raja, A.; Montoya−Castillo, A.; Zultak, J.; Zhang, X.-X.; Ye, Z.; Roquelet, C.; Chenet, D. A.; van der Zande, A. M.; Huang, P.; Jockusch, S.; Hone, J.; Reichman, D. R.; Brus, L. E.; Heinz, T. F. Energy Transfer from Quantum Dots to Graphene and MoS2: The Role of Absorption and Screening in Two-Dimensional Materials. *Nano Lett.* **2016**, *16* (4), 2328–2333. https://doi.org/10.1021/acs.nanolett.5b05012.
(203) Chen, Z.; Berciaud, S.; Nuckolls, C.; Heinz, T. F.; Brus, L. E. Energy Transfer from Individual Semiconductor Nanocrystals to Graphene. *ACS Nano* **2010**, *4* (5), 2964–2968. https://doi.org/10.1021/nn1005107.
(204) Lumerical Inc. https://www.lumerical.com/products/.
(205) Kennedy, B.; Hefferon, M. *What Americans Know About Science*; Pew Research Center, 2019; pp 1–27.
(206) NSF. *S&E Indicators 2018, Chapter 7: Science and Technology: Public Attitudes and Understanding*; National Science Foundation, 2018.
(207) Druckman, J. N.; McGrath, M. C. The Evidence for Motivated Reasoning in Climate Change Preference Formation. *Nat. Clim. Change* **2019**, *9* (2), 111–119. https://doi.org/10.1038/s41558-018-0360-1.

(208) Funk, C.; Kennedy, B. *The Politics of Climate Change*; Pew Research Center, 2016; p 114.
(209) Funk, C.; Goo, S. K. *What Americans Know and Don't Know about Science*; Pew Research Center, 2015.
(210) Bunis, D. The Immense Power of the Older Voter in an Election https://www.aarp.org/politics-society/government-elections/info-2018/power-role-older-voters.html (accessed May 18, 2020).
(211) Cronin, D. P.; Messemer, J. E. Elevating Adult Civic Science Literacy Through a Renewed Citizen Science Paradigm. *Adult Learn.* **2013**, *24* (4), 143–150. https://doi.org/10.1177/1045159513499550.
(212) King, A. C.; Winter, S. J.; Sheats, J. L.; Rosas, L. G.; Buman, M. P.; Salvo, D.; Rodriguez, N. M.; Seguin, R. A.; Moran, M.; Garber, R.; Broderick, B.; Zieff, S. G.; Sarmiento, O. L.; Gonzalez, S. A.; Banchoff, A.; Dommarco, J. R. Leveraging Citizen Science and Information Technology for Population Physical Activity Promotion. *Transl. J. Am. Coll. Sports Med.* **2016**, *1* (4), 30–44.
(213) Merenlender, A. M.; Crall, A. W.; Drill, S.; Prysby, M.; Ballard, H. Evaluating environmental education, citizen science, and stewardship through naturalist programs. *Conserv. Biol.* **2016**, *30* (6), 1255–1265. https://doi.org/10.1111/cobi.12737.
(214) Tuckett, A. G.; Freeman, A.; Hetherington, S.; Gardiner, P. A.; King, A. C.; On behalf of Burnie Brae Citizen Scientists. Older Adults Using Our Voice Citizen Science to Create Change in Their Neighborhood Environment. *Int. J. Environ. Res. Public. Health* **2018**, *15* (12), 2685. https://doi.org/10.3390/ijerph15122685.
(215) Andrews, E.; Weaver, A.; Hanley, D.; Shamatha, J.; Melton, G. Scientists and Public Outreach: Participation, Motivations, and Impediments. *J. Geosci. Educ.* **2005**, *53* (3), 281–293. https://doi.org/10.5408/1089-9995-53.3.281.
(216) Kennedy, M.; Daugherty, R.; Garibay, C.; Sanford, C.; Braun, R.; Koerner, J.; Lewin, J. Science Club: Bridging In-School and Out-of-School STEM Learning Through a Collaborative, Community-Based After-School Program. *Sci. Scope Wash.* **2017**, *41* (1), 78–79.
(217) Laursen, S.; Liston, C.; Thiry, H.; Graf, J. What Good Is a Scientist in the Classroom? Participant Outcomes and Program Design Features for a Short-Duration Science Outreach Intervention in K–12 Classrooms. *CBE—Life Sci. Educ.* **2007**, *6* (1), 49–64. https://doi.org/10.1187/cbe.06-05-0165.
(218) Laursen, S. L.; Thiry, H.; Liston, C. S. The Impact of a University-Based School Science Outreach Program on Graduate Student Participants' Career Paths and Professional Socialization. *J. High. Educ. Outreach Engagem.* **2012**, *16* (2), 47–78.
(219) Alexander, H.; Waldron, A. M.; Abell, S. K. Science and Me: A Student-Driven Science Outreach Program for Lay Adult Audiences. *J. Coll. Sci. Teach.* **2011**, *40* (6), 28–34.
(220) Rapson, V. Communicating Astronomy with the Public Journal. *Commun. Astron. Public* **2014**, *15*, 18–19.
(221) Simone, P. M.; Scuilli, M. Cognitive Benefits of Participation in Lifelong Learning Institutes. *LLI Rev.* **2006**, *1*, 44–51.

(222) Brady, E. M.; Cardale, A.; Neidy, J. C. The Quest for Community in Osher Lifelong Learning Institutes. *Educ. Gerontol.* **2013**, *39* (9), 627–639. https://doi.org/10.1080/03601277.2012.734147.
(223) Lamb, R.; Brady, E. M. Participation in Lifelong Learning Institutes: What Turns Members On? *Educ. Gerontol.* **2005**, *31* (3), 207–224. https://doi.org/10.1080/03601270590900936.
(224) Talmage, C. A.; Hansen, R. J.; Knopf, R. C.; Thaxton, S. P.; McTague, R.; Moore, D. B. Unleashing the Value of Lifelong Learning Institutes: Research and Practice Insights From a National Survey of Osher Lifelong Learning Institutes. *Adult Educ. Q.* **2019**, *69* (3), 184–206. https://doi.org/10.1177/0741713619834651.
(225) Lamb, R. Lifelong Learning Institutes: The Next Challenge. *LLI Rev.* **2011**, *6*, 1–10.
(226) D. Jones, M.; Anderson Crow, D. How Can We Use the 'Science of Stories' to Produce Persuasive Scientific Stories? *Palgrave Commun.* **2017**, *3* (1), 1–9. https://doi.org/10.1057/s41599-017-0047-7.
(227) Scheufele, D. A.; Krause, N. M. Science Audiences, Misinformation, and Fake News. *Proc. Natl. Acad. Sci.* **2019**, *116* (16), 7662–7669. https://doi.org/10.1073/pnas.1805871115.
(228) Antonioni, D. The Effects of Feedback Accountability on Upward Appraisal Ratings. *Pers. Psychol.* **1994**, *47* (2), 349–356. https://doi.org/10.1111/j.1744-6570.1994.tb01728.x.
(229) Bubela, T.; Nisbet, M. C.; Borchelt, R.; Brunger, F.; Critchley, C.; Einsiedel, E.; Geller, G.; Gupta, A.; Hampel, J.; Hyde-Lay, R.; Jandciu, E. W.; Jones, S. A.; Kolopack, P.; Lane, S.; Lougheed, T.; Nerlich, B.; Ogbogu, U.; O'Riordan, K.; Ouellette, C.; Spear, M.; Strauss, S.; Thavaratnam, T.; Willemse, L.; Caulfield, T. Science Communication Reconsidered. *Nat. Biotechnol.* **2009**, *27* (6), 514–518. https://doi.org/10.1038/nbt0609-514.
(230) Liu, X.; Hersam, M. C. Interface Characterization and Control of 2D Materials and Heterostructures. *Adv. Mater.* **2018**, *30* (39), 1801586. https://doi.org/10.1002/adma.201801586.
(231) Gilmore, R. H.; Lee, E. M. Y.; Weidman, M. C.; Willard, A. P.; Tisdale, W. A. Charge Carrier Hopping Dynamics in Homogeneously Broadened PbS Quantum Dot Solids. *Nano Lett.* **2017**, *17* (2), 893–901. https://doi.org/10.1021/acs.nanolett.6b04201.
(232) Park, C. H.; Lee, S.; Pornnoppadol, G.; Nam, Y. S.; Kim, S. H.; Kim, B. J. Microcapsules Containing PH-Responsive, Fluorescent Polymer-Integrated MoS_2: An Effective Platform for in Situ PH Sensing and Photothermal Heating. *ACS Appl. Mater. Interfaces* **2018**, *10* (10), 9023–9031. https://doi.org/10.1021/acsami.7b19468.
(233) Zheng, W.; Feng, W.; Zhang, X.; Chen, X.; Liu, G.; Qiu, Y.; Hasan, T.; Tan, P.; Hu, P. A. Anisotropic Growth of Nonlayered CdS on MoS_2 Monolayer for Functional Vertical Heterostructures. *Adv. Funct. Mater.* **2016**, *26* (16), 2648–2654. https://doi.org/10.1002/adfm.201504775.
(234) Frederick, M. T.; Amin, V. A.; Swenson, N. K.; Ho, A. Y.; Weiss, E. A. Control of Exciton Confinement in Quantum Dot-Organic Complexes through Energetic Alignment of Interfacial Orbitals. *Nano Lett.* **2013**, *13* (1), 287–292. https://doi.org/10.1021/nl304098e.

(235) Lian, S.; Weinberg, D. J.; Harris, R. D.; Kodaimati, M. S.; Weiss, E. A. Subpicosecond Photoinduced Hole Transfer from a CdS Quantum Dot to a Molecular Acceptor Bound Through an Exciton-Delocalizing Ligand. *ACS Nano* **2016**, *10* (6), 6372–6382. https://doi.org/10.1021/acsnano.6b02814.

(236) Azzaro, M. S.; Dodin, A.; Zhang, D. Y.; Willard, A. P.; Roberts, S. T. Exciton-Delocalizing Ligands Can Speed Up Energy Migration in Nanocrystal Solids. *Nano Lett.* **2018**, *18* (5), 3259–3270. https://doi.org/10.1021/acs.nanolett.8b01079.

(237) Vasudevan, D.; Gaddam, R. R.; Trinchi, A.; Cole, I. Core-Shell Quantum Dots: Properties and Applications. *J. Alloys Compd.* **2015**, *636*, 395–404. https://doi.org/10.1016/j.jallcom.2015.02.102.

(238) Naaman, R.; Paltiel, Y.; Waldeck, D. H. Chiral Molecules and the Electron Spin. *Nat. Rev. Chem.* **2019**, *3* (4), 250–260. https://doi.org/10.1038/s41570-019-0087-1.

(239) Bloom, B. P.; Graff, B. M.; Ghosh, S.; Beratan, D. N.; Waldeck, D. H. Chirality Control of Electron Transfer in Quantum Dot Assemblies. *J. Am. Chem. Soc.* **2017**, *139* (26), 9038–9043. https://doi.org/10.1021/jacs.7b04639.

(240) Purcell-Milton, F.; McKenna, R.; Brennan, L. J.; Cullen, C. P.; Guillemeney, L.; Tepliakov, N. V.; Baimuratov, A. S.; Rukhlenko, I. D.; Perova, T. S.; Duesberg, G. S.; Baranov, A. V.; Fedorov, A. V.; Gun'Ko, Y. K. Induction of Chirality in Two-Dimensional Nanomaterials: Chiral 2D MoS_2 Nanostructures. *ACS Nano* **2018**, *12* (2), 954–964. https://doi.org/10.1021/acsnano.7b06691.

(241) Liu, X.; Hersam, M. C. 2D Materials for Quantum Information Science. *Nat. Rev. Mater.* **2019**, *4* (10), 669–684. https://doi.org/10.1038/s41578-019-0136-x.

(242) Tran, T. T.; Bray, K.; Ford, M. J.; Toth, M.; Aharonovich, I. Quantum Emission from Hexagonal Boron Nitride Monolayers. *Nat. Nanotechnol.* **2016**, *11* (1), 37–41. https://doi.org/10.1038/nnano.2015.242.

(243) Voiry, D.; Goswami, A.; Kappera, R.; Silva, C. D. C. C. E.; Kaplan, D.; Fujita, T.; Chen, M.; Asefa, T.; Chhowalla, M. Covalent Functionalization of Monolayered Transition Metal Dichalcogenides by Phase Engineering. *Nat. Chem.* **2015**, *7* (1), 45–49. https://doi.org/10.1038/nchem.2108.

(244) Ma, X.; Hartmann, N. F.; Baldwin, J. K. S.; Doorn, S. K.; Htoon, H. Room-Temperature Single-Photon Generation from Solitary Dopants of Carbon Nanotubes. *Nat. Nanotechnol.* **2015**, *10* (8), 671–675. https://doi.org/10.1038/nnano.2015.136.

Vita

Suyog Padgaonkar

1416 W Arthur Ave, Apt 1, Chicago, IL 60626
suyog.pad@gmail.com | 215-900-9047

Google Scholar: http://bit.ly/suyogscholar
LinkedIn: linkedin.com/in/suyogpad

Education

Northwestern University — Evanston, IL
PhD in Chemistry — May 2021
Advisors: Prof. Emily A. Weiss & Prof. Mark C. Hersam

Management Certificate for Scientists & Engineers — August 2020
Kellogg School of Management

University of Miami — Coral Gables, FL
BS in Chemistry | BA in Music — May 2016
Summa cum laude

Research

Graduate Researcher — November 2016 – May 2021
Advisors: Prof. Emily Weiss and Prof. Mark Hersam — *Northwestern University, Evanston, IL*

- Investigated how electrons behave in light-sensitive nanomaterials for applications in energy harvesting, solar fuel generation, and information storage

International Undergraduate Researcher — May 2015 – August 2015
Advisor: Prof. Suresh Valiyavettil — *National University of Singapore, Singapore*

- Engineered toxic metal-removing materials for water purification using modified biowaste
- Selected for a competitive (less than 5% acceptance rate) international research experience sponsored by the American Chemical Society (ACS)

Undergraduate Researcher — January 2014 – May 2016
Advisor: Prof. Amy Scott — *University of Miami, Coral Gables, FL*

- Synthesized and characterized light-sensitive inorganic catalysts for water-splitting reactions

Policy

Southeast Environmental Task Force (SETF)
Graduate Intern — April 2021 – present

- Wrote one-pagers with information on renewable and non-renewable energy resources and their effect on SE Chicago communities

- Compiled cumulative impact assessment of industrial pollution in Calumet River

Materials Research Society Government Affairs Committee
Member, Grassroots Advocacy Subcommittee August 2020 – present

- Drafted letters advocating for diversity and equity training in federal scientific facilities for Materials Research Society members to send to their representatives
- Participated in monthly calls to discuss latest developments in materials science policy

Science Policy Outreach Taskforce (SPOT)
Senior Advisor June 2020 – May 2021
President May 2019 – June 2020
Outreach Coordinator February 2017 – May 2019

- Co-founded a science policy organization at Northwestern for graduate students and postdoctoral associates seeking to advocate for science to policymakers and the general public
- Organized the first annual SPOT SciPol Symposium, an event with over 10 invited local expert speakers and 40 attendees from 7 different universities
- Assisted in the creation of a by-request one-pager program to provide scientific information to Illinois state legislators
- Wrote 5 successful internal and external grant proposals to raise over $15,000 in funds
- Established agendas and delegated tasks for monthly meetings for a 10+ member board
- Co-authored a Green Labs report to provide suggestions to increase sustainability in laboratories

Teaching and Service

Science with Seniors (SwS)
Founder April 2017 – present

- Founded a novel monthly science outreach program to bring science to senior citizens by establishing community partnerships with 3 local senior centers
- Recruited over 40 graduate students and postdoctoral associates with regular information sessions and organized over 40 monthly SwS sessions
- Transitioned monthly programs to Zoom during COVID-19 pandemic
- Designed surveys and analyzed feedback from over 300 responses
- Featured in Chicago Tribune in August 2018 and Chicago Sun Times in September 2020

Northwestern University
Graduate Researcher November 2016 – May 2021

- Mentored and trained 4 graduate and 2 undergraduate students on their research

Obama Foundation Chicago, IL
Community Leadership Corps Member May 2019 – December 2019

- Engaged in multiple trainings on community leadership and grassroots activism
- Developed a curriculum on financial wellness for graduating seniors in partnership with a high school in the South Side of Chicago

Science Club Chicago, IL
Senior Mentor September 2016 – June 2019

- Mentored 6 middle school students during weekly sessions by leading interactive science experiments

Department of Chemistry, Northwestern University Evanston, IL
Teaching Assistant September 2016 – June 2018

- Led 4 quarters of 10-15 students in organic and analytic chemistry laboratory experiments

Institute of Sustainability at Northwestern University Evanston, IL
Teaching Assistant September 2017 – December 2017

- Assisted in teaching and facilitating an introductory sustainability class of 100+ students

Department of Chemistry, University of Miami Coral Gables, FL
Workshop Coordinator August 2014 – May 2016

- Organized weekly workshops taught by over 30 undergraduate teaching assistants for over 500 students enrolled in organic chemistry

USolar Miami, FL
Instructor October 2015 – May 2016

- Taught elementary and middle school students about solar energy through interactive demos

Skills

Programming	Python (proficient), MATLAB (proficient)
Design	Adobe Illustrator & Photoshop (proficient)
Languages	Marathi (native), Hindi (conversational)

Awards

Outstanding Research Mentor Award 2020
International Institute of Nanotechnology, Northwestern University

Institute of Sustainability at Northwestern Cluster Fellowship 2017 – 2018
Northwestern University

Outstanding Senior, Bachelor of Arts in Music 2016
Frost School of Music

Edward T. Foote Fellowship 2012 – 2016
University of Miami

Stamps Family Leadership Scholarship 2012 – 2016
University of Miami

Publications

Research (* indicates equal contribution)

1. Amsterdam, S. H.*; Stanev, T. K.*; Zhou, Q.; Wang, L.; Irgen-Gioro, S.; **Padgaonkar, S.**; Murthy, A. A.; Sangwan, V. K.; Dravid, V. P.; Weiss, E. A.; Chan, M.; Darancet, P.; Hersam, M. C.; Stern, N. P.; Marks, T. J., "Mechanistic Investigation of MoS_2 Defect Photoluminescence Quenching by Adsorbed Metallophthalocyanines," *in preparation*.
2. **Padgaonkar, S.***; Brown, P. T.*; Jeong, Y.; Cherqui, C.; Avanaki, K. N.; López-Arteaga, R.; Irgen-Gioro, S.; Wu, Y.; Sangwan, V. K.; Schatz, G. C.; Hersam, M. C.; Weiss, E. A., "Mechanism of Long-Range Energy Transfer from Quantum Dots to Black Phosphorus," *submitted* (invited paper).
3. Chang, W. J.*; Irgen-Gioro, S.*; **Padgaonkar, S**.; López-Arteaga, R.; Weiss, E. A., "Photo-redox Mediated Sensitization of Lanthanide Dopants by Perovskite Quantum Dots," *submitted*.
4. Irgen-Gioro, S.*; Wu, Y.*; López-Arteaga, R.; **Padgaonkar, S**.; Olding, J. N.; Weiss, E. A., "Evidence for Two Timescale-Specific Blinking Mechanisms in Room-Temperature Single Nanoplatelets," *submitted*.
5. Ricci, F.; Marougail, V.; Varnavski, O.; Wu, Y.; **Padgaonkar, S**.; Irgen-Gioro, S.; Weiss, E. A.; Goodson, T., "Enhanced Exciton Quantum Coherent Properties in Single $CsPbBr_3$ Perovskite Quantum Dots using Femtosecond Two-Photon Near-Field Scanning Optical Microscopy at Room Temperature," *submitted*.
6. Spanopoulos, I.; Hadar, I.; Ke, W.; Guo, P.; Mozur, E.; Morgan, E.; Wang, S.; Zheng, D.; **Padgaonkar, S.**; Manjunatha Reddy, G. N.; Weiss, E. A.; Hersam, M. C.; Seshadri, R.; Schaller, R. D.; Kanatzidis, M., "Tunable Broad Light Emission from 3D 'Hollow' Bromide Perovskites through Defect Engineering," *Journal of the American Chemical Society*, **2021**, *143* (18), 7069-7080.
7. **Padgaonkar, S.***; Eckdahl, C. T.*; Sowa, J. K.; López-Arteaga, R.; Westmoreland, D. E.; Woods, E. F.; Irgen-Gioro, S.; Nagasing, B.; Seideman, T.; Hersam, M. C.; Kalow, J. A.; Weiss, E. A., "Light-Triggered Switching of Quantum Dot Photoluminescence through Excited-State Electron Transfer to Surface-Bound Photochromic Molecules," *Nano Letters*, **2021**, *21* (1), 854-860.
8. Amsterdam, S .H.*; LaMountain, T.*; Stanev, T. K.*; Sangwan, V. K.; López-Arteaga, R.; **Padgaonkar, S.**; Watanabe, K.; Taniguchi, T.; Weiss, E. A.; Marks, T. J.; Hersam, M. C.; Stern, N. P, "Tailoring the Optical Response of Pentacene Thin Films via Templated Growth on Hexagonal Boron Nitride," *Journal of Physical Chemistry Letters*, **2021**, *12* (1), 26-31.

9. Irgen-Gioro, S.; Yang, M.; **Padgaonkar, S.**; Chang, W. J.; Zhang, Z.; Nagasing, B.; Jiang, Y.; Weiss, E. A., "Charge and Energy Transfer in the Context of Colloidal Nanocrystals," *Chemical Physics Reviews*, **2020**, *1*, 011305 (invited paper).

10. **Padgaonkar, S.**; Olding, J. N.; Lauhon, L. J.; Hersam, M. C.; Weiss, E. A., "Emergent Optoelectronic Properties of Mixed-Dimensional Heterojunctions," *Accounts of Chemical Research*, **2020**, *53* (4), 763-772 (invited paper, front cover).

11. Irgen-Gioro, S.; Roy, P.; **Padgaonkar, S.**; Harel, E., "Low Energy Excited State Vibrations Revealed in Conjugated Co-Polymer PCDTBT," *Journal of Chemical Physics*, **2020**, *152*, 044201 (invited paper).

12. **Padgaonkar, S.**; Amsterdam, S. H.; Bergeron H.; Su., K.; Marks, T. J.; Hersam, M. C.; Weiss, E. A., "Molecular Orientation-Dependent Interfacial Charge Separation in Phthalocyanine/MoS_2 Mixed-Dimensional Heterojunctions," *Journal of Physical Chemistry C*, **2019**, *123* (21), 13337-13343.

13. Mazza, M. A.; Hu, Q.; Yamazaki, S.; Mai, D. X.; **Padgaonkar, S.**; Peurifoy, S. R.; Goncalves, A.; Scott, A. M., "Photoinduced Charge Recombination in Dipolar D-A-A Photonic Liquid Crystal Polymorphs," *Physical Chemistry Chemical Physics*, **2017**, *19*, 4588-4596.

14. Qian, L.; Yuan, F.; Rodriguez-Tello, P.; **Padgaonkar, S.**; Zhang, Y., "Human Fanconi Anemia Complementation Group A Protein Stimulates the 5′ Flap Endonuclease Activity of FEN1," *PLoS ONE*, **2013**, *8* (12), e82666.

Outreach/Policy

1. **Padgaonkar, S.**; Schafer, E., "Science with Seniors: A Model Program for Senior Citizen-Centered STEM Outreach," *Journal of Higher Education Outreach and Engagement*, **2021**, *in press*.

2. Chintam, K.*; Barber, O. W.*; **Padgaonkar, S.**, "Overview of Pharmaceutical Disposal Methods: Addressed to the General Assembly of Illinois," *Journal of Science Policy and Governance*, **2020**, *17* (1).

Presentations

Research ([a]oral or [b]poster)

1. **Padgaonkar, S.**; Hersam, M. C.; Weiss, E. A., "Influence of Interfacial Morphology on Ultrafast Charge Separation in 0D/2D Mixed-Dimensional Heterojunctions," **December 2019**, *Materials Research Society Fall Meeting (Boston, MA)*.[a]

2. **Padgaonkar, S.**; Hersam, M. C.; Weiss, E. A. "Molecular Orientation-Dependent Interfacial Charge Separation in Phthalocyanine/MoS_2 Mixed-Dimensional Heterojunctions," **May 2019**, *American Chemical Society Great Lakes Regional Meeting (Lisle, IL)*.[b]

3. **Padgaonkar, S.**; Valiyaveettil, S., "Arsenic Removal from Water by Treated Cellulose Fibers," **March 2016**, *American Chemical Society National Meeting (San Diego, CA).*[b]

4. **Padgaonkar, S.**; Valiyaveettil, S., "Summer in Singapore: Purifying Water and Exploring Southeast Asia," **March 2016**, *American Chemical Society National Meeting (San Diego, CA).*[a]

Outreach/Policy

1. **Padgaonkar, S.**, "Science with Seniors: A Model Program for Senior Citizen-Centered STEM Outreach," **April 2020**, *Advancing Research Impact in Society Broader Impacts Summit (Virtual).*[a]

2. **Padgaonkar, S.**; Axford, Y., "Science with Seniors: A Model Program for STEM Outreach towards Senior Citizens," **February 2020**, *American Association for the Advancement of Science Annual Meeting (Seattle, WA).*[a,b] (Awarded Honorable Mention in Graduate Student Poster Competition).

3. **Padgaonkar, S**; Neely, J.; Mullowney, M.; Savereide, L.; Lescott, C.; DiStefano, J.; McClure, E.; Schlossberg, S.; Mayers, R.; Siegel, K., "Science Policy Outreach Taskforce at Northwestern University," **November 2019**, *National Science Policy Network Science Policy Symposium (Madison, WI).*[b]

4. **Padgaonkar, S.**, "Science with Seniors: A Model Program for STEM Outreach towards Senior Citizens," **October 2019**, *Emerging Engagement Scholars Workshop (Denver, CO).*[a]